2021

Assessing the Effectiveness of CFD to Solve an Inverse Problem of Thermal Profiles for the ProtoDUNE-SP Neutrino Detector

Cecilia Anne Streff
South Dakota State University

ASSESSING THE EFFECTIVENESS OF CFD TO SOLVE AN INVERSE PROBLEM OF THERMAL PROFILES FOR THE PROTODUNE-SP NEUTRINO DETECTOR

BY

CECILIA STREFF

A thesis submitted in partial fulfillment of the requirements for the

Master of Science

Major in Mechanical Engineering

South Dakota State University

2021

THESIS ACCEPTANCE PAGE

Cecilia Streff

This thesis is approved as a creditable and independent investigation by a candidate for the master's degree and is acceptable for meeting the thesis requirements for this degree. Acceptance of this does not imply that the conclusions reached by the candidate are necessarily the conclusions of the major department.

Stephen Gent
Advisor Date

Kurt Bassett
Department Head Date

Nicole Lounsbery, PhD
Director, Graduate School Date

To my biggest supporters:
my parents, Paul and Louann, and my love, Ben,
for their sacrificial love and endless encouragement.

ACKNOWLEDGEMENTS

My deepest thanks go to all who have helped me throughout my time at South Dakota State University. In particular, thank you to my advisor and mentor, Dr. Stephen Gent, who not only sparked my interest in academic research, but also provided an unparalleled level of dedication to helping me become a better researcher and achieve my personal and professional goals. I will never be able to repay the patience, grace, and encouragement he afforded me during my time as his advisee. Thank you also to Dr. Gregory Michna for supporting me and my work during my time on this project; for continually asking the really tough questions; and for being such a phenomenal teacher. Next, thank you to my past and present lab mates, Dillon Pedersen, Weston Christensen, Taylor Seuss, and Jenna Harrison for being great teammates and helping build our lab's body of knowledge. Finally, thank you to our collaborators on the Deep Underground Neutrino Experiment for funding my work and providing our team with the tools and resources needed to perform this study.

CONTENTS

LIST OF FIGURES viii

LIST OF TABLES xi

NOMENCLATURE xii

ABSTRACT xiv

1 INTRODUCTION 1

1.1 Background 1

1.2 Computational Modeling 5

1.3 Case Study: ProtoDUNE-SP Neutrino Detector 6

1.4 Research Rationale and Objectives 10

1.5 Organization of the Work 11

2 LITERATURE REVIEW 12

2.1 Inverse Problems 12

2.1.1 A Brief History 13

2.1.2 Inverse Problem Formulation 14

2.1.3 Intricacies of Inverse Problems 17

2.1.4 Applications in Fluid Mechanics 18

2.2 Computational Fluid Dynamics (CFD) 22

2.3 Case Study – ProtoDUNE-SP Neutrino Detector 25

2.3.1 The DUNE Experiment 25

2.3.2 The ProtoDUNE-SP Detector 29

2.3.3 Previous ProtoDUNE-SP Modeling 32

2.4 Key Findings 34

3 METHODOLOGY 36
3.1 Forward Modeling the LAr Cryostat in CFD 37
3.1.1 Geometry Simplifications 38
3.1.2 Physics 48
3.1.3 Boundary Conditions 53
3.1.4 Numerical Solution 61
3.2 Parameterization 65
3.2.1 LAr-Ullage Interface Height 66
3.2.2 Cold Electronics Heat Source 66
3.2.3 Field Cage Volumetric Heat Source 67
3.2.4 Cable Tray and I-Beam Geometries 67
3.2.5 Combined Effects 69
3.3 Inverse Modeling 69
4 RESULTS AND DISCUSSION 73
4.1 Base CFD Simulation 73
4.2 Initial Model Parameterizations 75
4.2.1 Effect of LAr-Ullage Interface Height 75
4.2.2 Effect of Cold Electronics Heat Source 81
4.2.3 Effect of Field Cage Volumetric Heat Source 87
4.2.4 Effect of Cable Tray and I-Beam Geometries 91
4.3 Combined Effects 96
4.4 Discussion 98
5 CONCLUSIONS AND FUTURE WORK 102
5.1 Conclusions 102

5.2 Future Work 103

6 BIBLIOGRAPHY 105

LIST OF FIGURES

Figure 1. Comparison of direct and inverse problems. Direct problems solve for system outputs or effects “y.” Inverse problems solve for system inputs “x” based on measurements of outputs “y.” 2

Figure 2. Comparison of direct and inverse problems by a simple example. The forward problem of multiplication has a unique solution. The corresponding inverse problem of factorization does not. 2

Figure 3. The fluid in the ProtoDUNE-SP detector (right) is cooled, purified, and circulated by adjacent cryogenic systems (left), (The DUNE Collaboration, 2017) 7

Figure 4. Natural convective air flow in this room is caused by the radiator heating the fluid (upward/ rising motion) and the window cooling the fluid (downward/ sinking motion). (AEL Heating Solutions, 2018) 8

Figure 5. Overview of the components of Deep Underground Experiment (DUNE), (Fermi National Accelerator Laboratory, 2020a). 28

Figure 6. External structure of the ProtoDUNE-SP neutrino detector. 30

Figure 7. The working principle of neutrino detection in the ProtoDUNE-SP detector. Negatively charged particles released by neutrino interaction with argon are repelled from the like-charged CPA (left) towards the oppositely charged APA (right). (The DUNE Collaboration, 2020) 31

Figure 8. Location of Valencia and Hawaii temperature sensor arrays, adapted from Cervera (2019). 32

Figure 9. Cross sectional views of the actual (left) and simplified (right) insulation geometry. Plane on right is the location of the LAr ullage interface. 39

Figure 10. The physical geometries within the cryostat are too complex to model in their entirety. The bottom (gray) component represents the bottom wall (floor) of the inner membrane; its bounds in the x and z directions represent the locations of the inner walls. 41

Figure 11. CFD geometry impermeable components: framing (gray), cold electronics (pink), and CPA (yellow). 42

Figure 12. CFD geometry of porous components (from left to right): field cage (FC), anode plane assemblies (APAs), and ground planes (GP). 43

Figure 13. Model of actual cold electronics geometry (green boxes). 45

Figure 14. Simplified geometries in base CFD model. Temperature profiles Valencia and Hawaii are main basis of comparison with experimental. 47

Figure 15. Inlet pipes manifold system is asymmetric. Blue, horizontal segments (1-4) are modeled explicitly in base CFD model. 54

Figure 16. Inlet pipe boundary condition: heat flux with position. 58

Figure 17. Cross sectional view of base CFD model mesh at x = 0.0m. 62

Figure 18. Motivation for iteration-averaged temperature reporting. Previous CFD modeling methods resulted in slight unsteadiness in the temperature solution at convergence. 64

Figure 19. Iteration-averaged temperature reporting steadies the solution by taking the mean of the final 1,000 temperature calculations (iterations). 64

Figure 20. Photo of cable trays and cold electronics (CE) above APA. 68

Figure 21. Location of modeled cable trays and I-beams (left). Cable tray sizes (a) original and (b) larger modeled separately. 69

Figure 22. CFD Valencia temperature profile correction. 70

Figure 23. CFD base case, temperature profiles Valencia (left) and Hawaii (right) compared to experimental. 74

Figure 24. CFD case LAr height = 7.25m, temperature profiles Valencia (left) and Hawaii (right). 75

Figure 25. CFD case LAr height = 7.16m, temperature profiles Valencia (left) and Hawaii (right). 76

Figure 26. CFD varying LAr-ullage interface height, velocity streamlines with temperature contours, isometric (left) and +x normal (right). 78

Figure 27. Varying LAr-ullage interface height 7.40m (base) case, relative temperature contour with velocity vector (projection) in-plane with Valencia. 80

Figure 28. Varying LAr-ullage interface height 7.25m case, relative temperature contour with velocity vector (projection) in-plane with Valencia. 80

Figure 29. Varying LAr-ullage interface height 7.16m case, relative temperature contour with velocity vector (projection) in-plane with Valencia. 81

Figure 31. CFD case 0.5*CE Heat (168W), temperature profiles Valencia (left) and Hawaii (right). 82

Figure 30. CFD case No CE Heat (0W), temperature profiles Valencia (left) and Hawaii (right). 82

Figure 32. CFD case 1.5*CE Heat (504W), temperature profiles Valencia (left) and Hawaii (right). 82

Figure 33. CFD case 2.0*CE Heat (672W), temperature profiles Valencia (left) and Hawaii (right). 83

Figure 34. CFD Valencia MSE*10^6 with varying CE Heat. 84

Figure 35. Varying CE Heat Source 0W case, relative temperature contour with velocity vector (projection) in-plane with Valencia. 85

Figure 36. Varying CE Heat Source 168W case, relative temperature contour with velocity vector (projection) in-plane with Valencia. 86

Figure 37. Varying CE Heat Source 504W case, relative temperature contour with velocity vector (projection) in-plane with Valencia. 86

Figure 38. Varying CE Heat Source 672W case, relative temperature contour with velocity vector (projection) in-plane with Valencia. 87

Figure 40. CFD case FC Heat 320W/m^3, temperature profiles Valencia (left) and Hawaii (right). 88

Figure 39. CFD case FC Heat 32W/m^3, temperature profiles Valencia (left) and Hawaii (right). 88

Figure 41. CFD case FC Heat 800W/m^3, temperature profiles Valencia (left) and Hawaii (right). 88

Figure 42. Varying FC Heat Source 32W/m^3 case, relative temperature contour with velocity vector (projection) in-plane with Valencia. 90

Figure 43. Varying FC Heat Source 320W/m^3 case, relative temperature contour with velocity vector (projection) in-plane with Valencia. 90

Figure 44. Varying FC Heat Source 800W/m^3 case, relative temperature contour with velocity vector (projection) in-plane with Valencia. 91

Figure 47. CFD case I-Beams and Cable Trays (larger), temperature profiles Valencia (left) and Hawaii (right). 92

Figure 46. CFD case I-Beams and Cable Trays, temperature profiles Valencia (left) and Hawaii (right). 92

Figure 45. CFD case I-Beams, temperature profiles Valencia (left) and Hawaii (right). 92

Figure 48. CFD case I-Beams (+z beam longer) and Cable Trays (larger), temperature profiles Valencia (left) and Hawaii (right). 93

Figure 49. CFD case I-Beams, relative temperature contour with velocity vector (projection) in-plane with Valencia. 94

Figure 50. CFD case I-Beams and Cable Trays, relative temperature contour with velocity vector (projection) in-plane with Valencia. 95

Figure 51. CFD case I-Beams and Cable Trays (larger), relative temperature contour with velocity vector (projection) in-plane with Valencia. 95

Figure 52. CFD case I-Beams (+z beam longer) and Cable Trays (larger), relative temperature contour with velocity vector (projection) in-plane with Valencia. 96

Figure 53. Varying LAr-ullage interface height and near-surface geometries simultaneously, relative temperature contour with velocity vector (projection) in-plane with Valencia. 97

Figure 54. Relative temperature distribution with velocity vectors in-plane with the Valencia profile (x=3.414m), near surface geometries create “jetting” effect. 101

LIST OF TABLES

Table 1. Examples of inverse problem applications. 4
Table 2. Location and number of modeled temperature and impurity sensors..... 45
Table 3. LAr fluid properties assumed for CFD simulations. 51
Table 4. Solid continua (insulation and CPA) material properties assumed for CFD simulations. 51
Table 5. Summary of liquid continua physics model and solver settings..... 52
Table 6. Summary of solid continua (insulation and CPA) physics model and solver settings. 52
Table 7. Inlet Boundary Conditions: Mass Fractions and Fluid Temperatures. 55
Table 8. Properties of porous regions FC, APA, and GP in CFD model. 59
Table 9. LAr region boundary conditions. 60
Table 10. Insulation region boundary conditions. 60
Table 11. CFD base case, temperature profile mean squared errors and maximum deviation. 74
Table 12. CFD varying LAr heights, temperature profiles mean squared errors and maximum deviation. 76
Table 13. CFD varying CE heat, temperature profiles mean squared errors and maximum deviation. 83
Table 14. CFD varying FC heat, temperature profiles mean squared errors and maximum deviation. 89
Table 15. CFD varying I-Beam and Cable Tray geometries, temperature profiles mean squared errors and maximum deviation. 93

NOMENCLATURE

Abbreviations

APA	Anode Plane Assembly
CE	Cold Electronics
CFD	Computational Fluid Dynamics
CPA	Cathode Plane Assembly
DP	Dual Phase
DUNE	Deep Underground Neutrino Experiment
FC	Field Cage
GAr	Gaseous Argon
GP	Ground Plane
LAr	Liquid Argon
LBNF	Long Baseline Neutrino Facility
MSE	Mean Squared Error
SP	Single Phase
SURF	Sanford Underground Research Facility
RANS	Reynolds Averaged Navier Stokes

Variables

g	Acceleration due to gravity, (m^2/s)
h	Specific enthalpy, (J/kg-K)
k	Thermal conductivity, (W/m-K)

P	Pressure, (Pa)
T	Temperature, (K)
u	X-component of velocity ($u_1 = u_i$), (m/s)
v	Y-component of velocity ($u_2 = u_j$), (m/s)
$\vec{V}$	Velocity vector, (m/s)
w	Z-component of velocity ($u_3 = u_k$), (m/s)
β	Volumetric coefficient of thermal expansion, (1/K)
μ	Dynamic viscosity, (N-s/m^2)
ρ	Density, (kg/m^3)
τ	Shear stress, (N/m^2)

ABSTRACT

ASSESSING THE EFFECTIVENESS OF CFD TO SOLVE AN INVERSE PROBLEM OF THERMAL PROFILES FOR THE PROTODUNE-SP NEUTRINO DETECTOR

CECILIA STREFF

2021

Computational fluid dynamics (CFD) is a branch of fluid mechanics which is employed to numerically solve complex fluid, heat transfer, and multiphysics problems. Traditionally, CFD techniques are used to solve "forward" problems—using some known information of a system as inputs to a representative model to predict experimental measurements or expected system behavior. The work presented here demonstrates how CFD may be used to solve an "inverse" problem—given limited experimental data and some model, predict (previously unidentified) "input" system (or system model) parameters.

The case study for this research uses a validated CFD modeling approach of the liquid argon (LAr) region of the ProtoDUNE Single Phase neutrino detector. Incomplete experimental temperature data (which deviated from the expected, roughly-linear distribution with height for such a natural convection driven flow) are used to inform parametric changes to the base CFD model. Features such as the addition of previously neglected physical geometries and heat sources were parametrically added to the model in the commercial CFD program Star-CCM+, and the resulting temperature distributions were compared to the experimental data. Results of this study suggest that there are numerous possible causes for the abnormal experimental temperature distribution. Model

inputs such as increased heat from the cold electronics and the field cage (Faraday cage) and lowering of the LAr height caused a more nonlinear temperature distribution in the sensor region, improving CFD agreement. The addition of previously neglected flow obstructions near the LAr surface do not directly improve the temperature agreement but are significant to the flow patterns and thus should be included in future modeling. Confidence in the inverse problem solution is limited by uncertainties in “known” system information.

1 INTRODUCTION

Inverse problems are a unique and challenging class of problems in applied mathematics. This work aims to demonstrate an inverse problem solution through the application of computational fluid dynamics (CFD) to a particular engineering case study—the fluid temperature within a pressurized cryogenic tank of the ProtoDUNE-SP (ProtoDUNE Single Phase) neutrino detector. First, an introduction to inverse problems and inherent challenges in their solution will be introduced. Then, the research objectives will be presented in the context of CFD methodologies and the ProtoDUNE case study. Lastly, the rationale and objectives of this work are summarized.

1.1 Background

Engineers are often interested in analyzing, designing, or optimizing systems and processes and use associated natural phenomena and mathematical representations of the physical world to that end. In classical, deterministic problem solving the “forward” problem is addressed in which known (*a priori*) system information is used to fully define boundary conditions, initial conditions, and material properties necessary for mathematical representation and prediction of some measurable system output or performance. This procedure of *cause-to-effect* is referred to as the “direct,” “forward,” or “modelization” problem. By contrast, inverse problems arise when only partial information and indirect observations of the system are available. More specifically, if any part of the “direct” problem description (system material properties, boundary or initial conditions, and/or governing equations) is unknown and is sought after, the problem can be classified as an “inverse” or “indirect” problem. In this case, actual

system measurements are known, and the "hidden" system parameters of interest are the goal. Figure 1 depicts direct and inverse problems schematically.

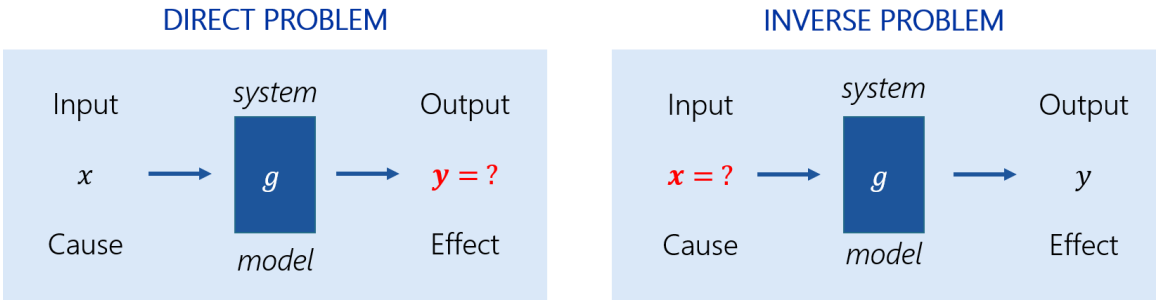

Figure 1. Comparison of direct and inverse problems. Direct problems solve for system outputs or effects "y." Inverse problems solve for system inputs "x" based on measurements of outputs "y."

Every direct problem has a corresponding inverse problem, so one may initially wonder if the assignment of "which is which" as arbitrary. To introduce the peculiarities of inverse problems, consider the classic direct problem of multiplication and its corresponding indirect problem of factorization (Figure 2). In elementary mathematics, we learn that multiplying two unique numbers yields one unique product. However, the inverse problem of factoring some number does not necessarily return the same pair of numbers. Rather a *set* or *landscape* of possible solutions exists for the indirect problem of factorization. Therefore, in inverse problems, constraints relevant to the physical system or situation must be put in place (i.e., do the factors belong to the set of real numbers? The set of positive integers? Or unconstrained?).

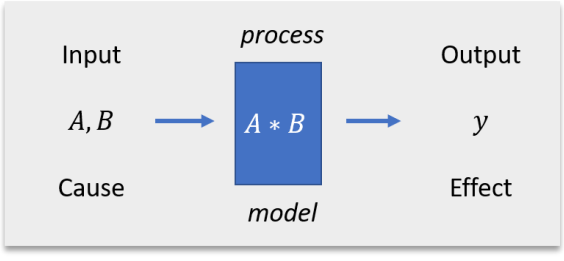

	Known	Find
Forward (Direct) Problem	$A = B = 12$	$y = ?$
Inverse Problem	$y = A * B = 144$	$A = ?, B = ?$

Figure 2. Comparison of direct and inverse problems by a simple example. The forward problem of multiplication has a unique solution. The corresponding inverse problem of factorization does not.

The goal of any inverse problem is the identification or quantification of previously unknown system information: either the inputs (parameters) *into* the system or the mathematical behavior (functional description) *of* the system. This gives rise to the two primary classifications of inverse problems: parameter estimation and function estimation. Parameter estimation (or "causation") problems are concerned with determining the inputs, loads, or sources applied on or into the system. Function estimation (or "model identification") problems, on the other hand, deal with identifying the mathematical models, equations, or model parameters which describe the system and its behavior in producing some "output" or observable data. In our previous example of multiplication and factorization, the parameter estimation problem may be determining A and B given the model of multiplication and the output y; the model identification problem may be determining the mathematical operation ("model") which relates known inputs A and B to the known output y.

The application of inverse problems extends far beyond simple algebraic examples. Table 1 lists a few general applications of inverse problems with their system definitions, measurable data, and parameters of interest identified. In every case, certain system measurements are available and unmeasurable or unobservable system information is the goal.

Table 1. Examples of inverse problem applications.

Problem Description	System	Observable Parameter(s)	Parameter of Interest
Tensile testing of material sample	Metal dog-bone sample	Elongation, Force Applied	Modulus of Elasticity
Medical imagining of human patient	Human body	Propagation of electromagnetic waves with time and position	Tissue density with location
Reconstruction of inner-Earth density profiles	Planet Earth	Seismic earthquake data (intensity, time, location)	Size and shape of Earth mantel layer
Estimate/ locate contaminant source in river	Water in river	Location, intensity, time history of downstream contaminants	Location, intensity of source

In addition to the many, diverse applications of inverse problems, there are likewise many available methods for approaching and solving this type of problem. Most inverse problems involve iterations of three main steps (Tarantola, 2005):

1. *Parameterization of the System:* Identifying the system of interest and all model parameters (system "inputs") which completely characterize the system (from a given point of view). The values of all model parameters are not known at this point—may be estimated or assumed.
2. *Forward Modeling:* Discovery of the physical laws (governing mathematical formulae) allowing us (for given values of the model parameters) to make predictions on the measurements of some observable parameters.
3. *Inverse Modeling:* Use of the actual results of observable parameter measurements to infer the actual values of the model parameters. Comparison between forward-modeled predictions and actual measurements occur during this step.

It is worth noting that solving inverse problems is not a linear or sequential process. Rather, there exists significant interdependence between each step of the process. Additionally, reasonable system definition and model parameter estimation in setting up an inverse problem requires significant knowledge of the system and the governing physics. Without sufficient knowledge of the system, the values of model parameters may be initialized to physically impossible values, for example, an error that would propagate through to the forward modeling step. Similarly, if the governing equations are not understood or do not properly approximate the system, the forward modeling step will not accurately predict the theoretical system performance for the given model parameters. Therefore, it is important to appropriately understand the governing equations, the modeling process, and how to apply the assumed and given model parameters.

1.2 Computational Modeling

Computational fluid dynamics (CFD) is a branch of fluid mechanics which uses data structures and numerical methods to solve the complex systems of equations which govern fluid flows. Modern CFD allows engineers to analyze the intrinsic relationship between fluid temperature, velocity, and pressure for mathematically and/or geometrically complex fluid problems, which otherwise are not analytically solvable. The flexibility of CFD lends itself to applications of engineering analysis, design, and optimization in fields such as aerodynamics, turbomachinery, heating ventilation & air conditioning (HVAC), and many more applications.

CFD is most commonly used for solving direct or forward problems in fluid mechanics. Known system information (fluid properties, system geometry, and boundary

and initial conditions) are applied to a computer-generated (CAD) model of the fluid geometry, and the mathematical representation of the fluid (governing equations) is also applied. Then, CFD calculates and predicts system outputs or performances based on the discretization of the fluid and the model settings. The overall model error in this case is taken as the difference between the CFD and experimental results of some key variable or observable parameter.

This work aims to demonstrate how CFD can, instead, be used to solve inverse problems, where the goal is to determine unknown or missing system information, not the system response of an observable parameter. In this case, the traditional modeling procedure will be applied, but just as the forward modeling step of the inverse method. Different, parametric cases of system inputs will be modeled, and the simulation results will be compared to experimental data. Global minimization of this error is the task, and the corresponding combination of system inputs which accomplish that minimization will be identified as significant (and previously unknown) system features.

1.3 Case Study: ProtoDUNE-SP Neutrino Detector

Computational fluid dynamics modeling as a tool for solving an inverse problem in engineering is demonstrated in this work for a particular case study—the natural convective liquid argon (LAr) flow of the ProtoDUNE Single Phase (ProtoDUNE-SP) neutrino detector. With limited known system operating parameters and discrete experimental data (namely temperature and impurity), the aim is to predict “missing” information of the system. A previously validated CFD model of the LAr volume is parametrically varied, and the temperature results compared to the experimental. The goal is to identify model inputs which are plausible for the actual system and which

minimize the error between the CFD predicted and experimentally measured temperatures. Such inputs (such as flow obstructions and heat sources) are considered the solution to the inverse problem.

The ProtoDUNE-SP neutrino detector is a prototype fluid system for the international physics experiment DUNE (Deep Underground Neutrino Experiment). The goal of this international research effort is to study the readily abundant, but largely misunderstood, subatomic particle called the neutrino. Neutrinos, due to their size and mysterious behavior, rarely interact with matter. However, physicists have discovered that by generating a beam (or source) of neutrinos and aiming it at extremely pure liquid argon (LAr) in a controlled and instrumented environment, neutrinos' interactions with matter can be observed and documented. The LAr of interest is housed in highly sophisticated, pressurized and thermally insulated tanks called "cryostats." Cryostats are outfitted with instrumentation and electronics which collect data of the neutrino

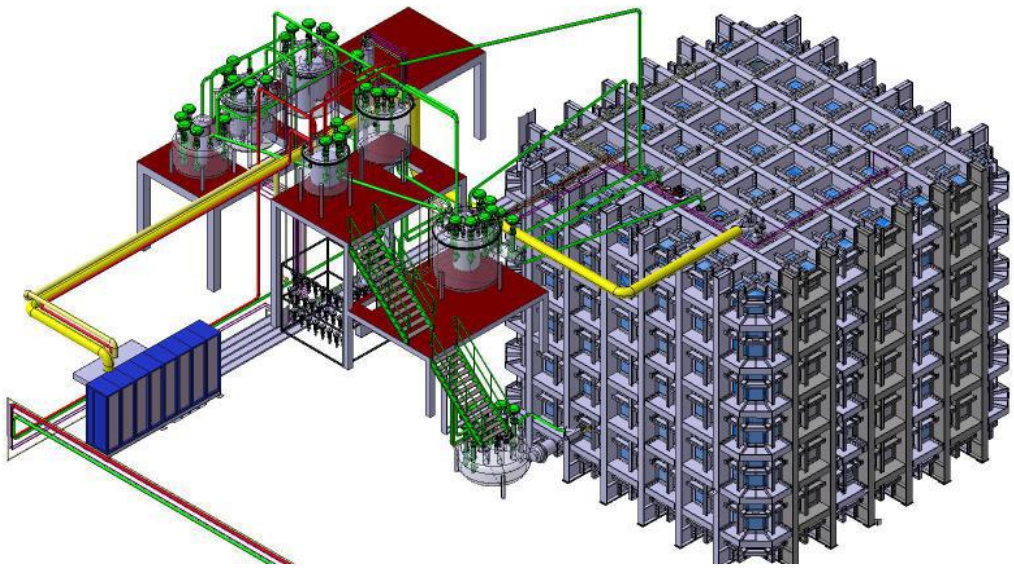

Figure 3. The fluid in the ProtoDUNE-SP detector (right) is cooled, purified, and circulated by adjacent cryogenic systems (left), (The DUNE Collaboration, 2017)

interactions, and which monitor the system operation. The ProtoDUNE-SP cryostat is shown at right in Figure 3.

The cryostat LAr is kept extremely cold (88K) and pure by the neighboring state-of-the-art cryogenic filtration system. During normal operation, the cryogenic filtration system pumps argon from the tank and purifies and cools it before returning it back to the cryostat volume. The LAr circulation rate is so low relative to the size of the fluid volume that the primary fluid motion is actually caused by thermal gradients in the fluid, not the pumping action. Heat transfer from the outside room-temperature air, through the detector insulation causes changes in fluid temperature. Changes (increases) in fluid temperature result in corresponding changes (decreases) in the fluid density. Then, the lower density fluid is driven upward due to buoyant forces. This phenomenon is called

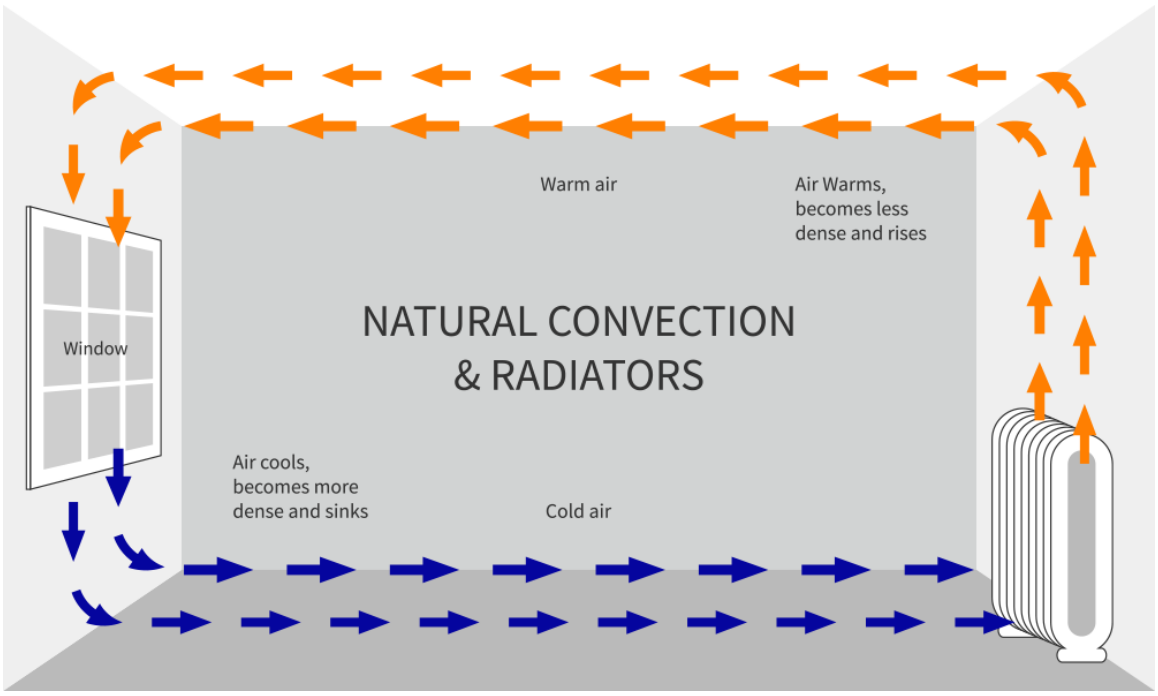

Figure 4. Natural convective air flow in this room is caused by the radiator heating the fluid (upward/ rising motion) and the window cooling the fluid (downward/ sinking motion). (AEL Heating Solutions, 2018)

natural or free convection. Natural convection in an enclosed room environment is illustrated in Figure 4.

Despite the filtration and cooling efforts, impurities such as oxygen and water molecules still threaten to contaminate the cryostat LAr, and subsequently, the quality of the neutrino physics experiments. Not only is the overall purity level important for neutrino detection, but so is the uniformity or distribution of impurities in the fluid, since even locally concentrated impurities may absorb neutrinos before being detected. It is assumed that impurities dissipate downward into the liquid argon from the gaseous layer at the top of the cryostat. Fluid motion (caused by temperature gradients and influenced by physical flow obstruction) carries the impurities throughout the fluid volume. Thus, there is also significant instrumentation within the cryostat, specifically for monitoring the fluid purity and temperature during operation.

A previously validated CFD model of the LAr region of the ProtoDUNE-SP detector has been used to predict the steady-state LAr temperature, velocity, and impurity profiles throughout the cryostat. With respect to temperature profile agreement, the CFD model predicts the temperature profiles of interest to within ±3mK. Near the top liquid region of the cryostat, experimental temperature profiles deviate from the roughly-linear profile predicted by the CFD model. Therefore, the cryostat features which may cause this slightly discrepant temperature result are of interest. Photos and reports of the actual system are used to identify previously neglected cryostat components which may be significant to the flow profiles and/or fluid temperature distributions. Physical component geometries (flow obstructions) and components which may generate and dissipate heat to the fluid are investigated.

1.4 Research Rationale and Objectives

The performance of the ProtoDUNE-SP neutrino experiments is highly dependent on consistent and uniform purity of the LAr in the neutrino detection region (the time projection chamber). To accurately predict the propagation of impurities and thus detector physics, the Fermilab researchers require even further refinement of temperature modeling.

The issue, however, is that available information about the actual detector is limited. The available experimental data and details of experimental procedures and associated precision are also limited. For example, for the large volume, temperature measurements are only available for a finite number of points, are time-averaged, and calibrated using an unclear procedure which is independent of this research. Additionally, even if every detail of the experimental system were available, the size and complexity of the modeled system would far exceed the limits of available computing resources. Therefore, when designing the model, it is important to make informed decisions about which physical and thermal features of the experiment are most significant. To that end, if we are able to identify and appropriately model the significant heat sources and/or flow obstructions of the system, we may be able to further improve the agreement between the predicted (modeled) and measured (experimental) temperature data.

It is hypothesized that if actual heat sources and flow obstructions are correctly modeled in CFD, agreement between simulated and experimental temperature profiles will improve. Therefore, the goals of this work are to (1) solve an engineering inverse problem of identifying CFD input parameters which may cause static temperature profile discrepancy near the top LAr surface in the ProtoDUNE-SP neutrino detector, and (2)

quantify the thermal effect (sensitivity) on the static temperature profile due to the different CFD model representations.

1.5 Organization of the Work

This work presents research on the solution of an engineering inverse problem with computational fluid dynamics. Chapter 2 reviews the history, definition, and application of inverse problems as well as the basics of CFD modeling. The particular case study of interest—the ProtoDUNE-SP neutrino detector—is presented in the context of the Deep Underground Neutrino Experiment and past CFD research. Chapter 3 details the methodology of this work starting with the forward CFD modeling procedures (geometry, physics models, boundary conditions, and numerical formulation). The parametric changes to the baseline CFD model (heat sources and flow obstructions) are then given. Lastly, the inverse modeling methods which relate the results of the parameterized forward models to the experimental data are introduced. Chapter 4 gives the results of the parameterized forward models and the inverse reasoning and discusses the significance and relevance of the cases. Chapter 5 summarizes the major conclusions of this work and speculates on potential future developments.

2 LITERATURE REVIEW

This chapter introduces fundamental concepts relevant to the application of computational fluid dynamics to solve an inverse problem in thermal-fluids engineering. First, the general definition and historical applications of inverse problems are presented. Then, CFD modeling methods and considerations are detailed. Finally, details of the ProtoDUNE-SP neutrino detector case study are offered with the project rationale and objectives.

2.1 Inverse Problems

Mathematical representations and physical theories of natural phenomena are central to engineering analyses. In traditional deterministic problem solving, sufficient given (or previously known) information of a physical system is used in conjunction with descriptive physical theories— "mathematical models"—to explain and predict system behavior or (often measurable) outcomes of the system. In other words, enough system information is available to carry out a well-defined, stable mathematical analysis to come to a unique solution. This is referred to as a "forward" or "direct" problem. However, not all systems analyses are so well-posed. Often, systems are not fully defined, and it is not possible or reasonable to directly measure or observe quantities of interest. In such "inverse problems," limited measurements and partial system information must be used to determine (hidden) quantities of interest of the system. (Tarantola, 2005)

Inverse problems constitute a prolific field of applied mathematics, both historically and in modern day. The engineering discipline has a dedicated journal *Inverse Problems in Science and Engineering* (2004) on the subject. Taking such names

as parameter estimation or identification problems and model or function identification problems, among others, inverse problems have found innumerable applications in fields such as medical imagining, astro- and particle-physics, satellite image reconstruction, geology, and, most relevant to this work, heat transfer and fluid mechanics (Argoul, 2012). With such wide definitions and applications, a comprehensive review of the definition, history, application, and methods of inverse problems is far beyond the scope of this work. Instead, a functional "engineer's" (as opposed to a rigorous "mathematician's") definition of inverse problems is presented. Then historical and modern applications of inverse problems are discussed with a focus on thermo-fluid systems. Finally, shortcomings and challenges of inverse problems for engineering applications are outlined.

2.1.1 A Brief History

The history and definition of inverse problems are, clearly, intertwined. In fact, this researcher finds that a general definition of inverse and ill-posed problems is best understood within their historical contexts. Therefore, a brief review of impactful inverse problems throughout history is given here.

- *400BC – Plato's Prisoner in a Cave Allegory.* Prisoner had to reconstruct the physical world by the observation of shadows cast on the cave wall and echoes heard from the outside. Demonstrated the problem of non-unique solutions and input-to-output dimensionality concerns.
- *380BC – Aristotle's arguments for the spherical Earth.* Indirect observations of the shadows that Earth casts on the moon to deduct the roundness of the

planet. Constituted the basics of modern *geometric tomography* and projective geometry.

- *1570's – Kepler's determination of elliptical planetary orbits.* Curve fitting Mars location data to deduce the shape and size of planetary orbits.
- *1600's – Newton's development of his First Law.* Seeking to mathematically explain Kepler's laws for planetary motion, Newton determines that the gravitational force between two objects (planets) is inversely proportional to the square of the distance between the objects. Numerous direct and inverse problems are presented in Newton's Principia.

2.1.2 Inverse Problem Formulation

An inverse problem, as previously mentioned, refers to the best possible reconstruction or missing system information to identify or estimate either: 1) the loads, sources, or causes of the system response, or 2) undetermined mathematical model parameters which describe the system (Tarantola, 2005). For the "Type 1" inverse problems, values and features of the system (such as material properties, geometries, boundary conditions, etc.) are unknown and are sought after. On the other hand, "Type 2" inverse problems seek to determine how to best represent a system mathematically. This could include seeking all or a portion of the governing physics/equation or could be used in justifying simplifying assumptions to the system model. In either case, inverse problems use measurements of the system to estimate unknown quantities of a physical system or process (Orlande, 2012). In thermo-fluids engineering applications, inverse problems are particularly useful when it is not possible to take direct measurements of

system parameters of interest, such as boundary or initial conditions, as one example. Another useful application is in engineering design when a desired system response is known, and the particular system parameters needed to accomplish that goal are unknown.

An inverse problem "system" is any object, machine, or process which may be represented mathematically—ideally with widely-accepted physical laws. As in deterministic problem solving, the system definition depends on the expert's knowledge of the problem, available information, and research goals. To a metallurgist, a system may be a dog-bone material sample for tensile testing. To a geologist, a system may be the planet Earth or a particular mountain. (Tarantola, 2005)

After the system is identified, the first step of solving an inverse problem is to parameterize the system. This includes identifying all model parameters and system inputs which fully characterize the system from a given point of view, and assigning values to the known quantities (Tarantola, 2005). Input signals into the system, physical material properties, system geometries, or boundary conditions are all examples of system input parameters since they influence the system response. In the case of heat transfer and fluid mechanics, system parameters often include fluid properties, flow rates, pressures, temperatures, heat fluxes, pipe or duct geometries, etc. For system parameters that are identified, but whose values are unknown, it is necessary to constrain them to whatever extent possible. This may include defining a range or limits to what is physically relevant or possible. For example, if an engineer were sizing a duct for some fluids problem with desired flow rates and pressure drops, one could constrain the duct dimensions with upper limit defined by the installation space. The lower limit to the duct

dimensions could be enforced by specifying a cross-section greater than zero. Further reasoning and information of the unique application may inform additional constraints such as the order of magnitude of the duct dimensions, pressure drops, etc.

After the system parameters are identified and defined (where possible), the next step is forward modeling. The “model” is a mathematical representation of the physical system which simulates or predicts the system behavior for some set of known parameters and estimates of unknown parameters. The model may be as simple as a single equation, a set of equations, or as complex as a high-fidelity computer program. Regardless, the model must (from the given point of view) be able to predict the system response with the chosen parameters as inputs to the model. This forward modeling step is repeated iteratively with updated guesses for the unknown system parameters. These estimated or “guessed” system values do not take any meaning until the final step.

The final step of solving an inverse problem involves leveraging the direct modeling results to find relationships between the input model parameters and the system response (Woodbury, 2000). First, the problem “residuals” or “error” is taken as the difference between system measurements and the calculated (direct method prediction) values (Orlande). For a properly validated forward model that appropriately models the system behavior for some input parameters, the residuals should be minimized (Jaluri, 2020). Then, an “objective function” is defined (explicitly or implicitly) which expresses the mathematical goal of the inverse problem—most typically, minimizing residuals or some function of the residuals with respect to the modeled system inputs. At this point in the solution process, the inverse problem often becomes an optimization problem—seeking to identify which combination(s) of system parameters minimize the difference

between the modeled and measured data, thus resulting in new understanding of the physical system.

A popular approach currently is applying machine learning (ML) schemes such as neural networks (NN) to find interesting trends in experimental and calculated data (Yaman, 2013). In such a problem, many simulations (forward model calculations) must be carried out over ranges of model input parameters, else resulting in a "sparse" dataset. The results of the numerous simulations are then used to "train" the ML algorithm (Tamaddon-Jahromi, 2020). The result of a successfully trained algorithm is a code which can predict system outputs or responses on-demand.

2.1.3 Intricacies of Inverse Problems

There are a few unique characteristics of inverse problems from a mathematics perspective. Direct or forward problems are generally well-posed. The three necessary conditions for a well-posed mathematical problem are solution stability, existence, and uniqueness (Argoul, 2012). Inverse problems, on the other hand, often do not satisfy all these conditions, which presents a challenge for the interested researcher. Therefore, it is particularly important to properly and fully constrain any inverse problem through the explicit definition and application of available system information called *a priori* information (Tarantola, 2005).

The dimensionality of the system "inputs" and "outputs" are also a concern in defining, constraining, and solving inverse problems. For example, system inputs and outputs may be continuous (like a sinusoidal electrical signal) or discrete, and there may

be singular or an infinite number of inputs and outputs. It is therefore important to consider the complexity and dimensionality of the problem when parameterizing system.

These challenges considered, it is worth pointing out the paradox of inverse problems. If we are after "missing" system information, we try to solve inverse problems. However, in order to ensure the problem is solvable (solution existence) and to increase the accuracy of the solution (reduce number of solutions), one must know ahead of time a great deal about their chosen system. For example, knowledge of the governing equations and physical situation may help in determining reasonable simplifying assumptions; in constraining or restricting the domain of plausible solutions; etc. Consequently, to determine missing information about an incompletely defined system, you have to know (at least roughly) how to define the system, its inputs, and its behavior mathematically.

2.1.4 Applications in Fluid Mechanics

There are innumerable examples of inverse problems in engineering applications, including fluid mechanics. Of particular relevance to this research are the heat source identification problem; flow obstruction identification problem; and impurity source identification problem. In the source (heat or contaminant) identification problems, the goal may be the location and or the magnitude of the source based on indirect measurements of the ambient fluid temperature or contaminants, respectively. In the flow obstruction identification problem, downstream fluid velocities are used to reconstruct or estimate upstream geometries.

Heat Transfer Boundary Conditions. A classical application of inversion in fluid mechanics and heat transfer is the determination of boundary conditions from free-stream

measurements. The heat flux or temperature condition of a surface-fluid interface, for example, may be back-figured from fluid temperature measurements. Huang and Özisik (1992) presented a general analysis of inversely determining unknown wall heat flux values using free stream measurements of laminar forced flow through a parallel duct. The numerical optimization method "conjugate gradient method" was used to correlate those measurements to the spatially-varying flux wall condition. Bangian-Tabrizi and Jaluria (2018) similarly applied optimization—in this case a search-based algorithm—to the estimate the isothermal and flux wall boundary conditions in a natural convective flow. In this case, many forward models were calculated in CFD to act as the system response ("experimental") dataset.

An extension of this problem is the deduction of wall convective heat transfer coefficients by fluid temperature measurement (Farahani, Najafi, Kowsary, & Ashjaee, 2016). This has been found particularly useful with the complex geometries often found in heat exchanger or heat sink applications (Kumar & Nagarajan, 2018). The inverse problem solution not only helps in understanding the given experimental system, but also aids in developing correlations for the heat transfer behavior of the specific problem or problem type. Chen and Chou (2006) demonstrated an inversion technique of finite differencing and least squares regression to determine the natural convective heat transfer coefficients on an experimental square fin on a round pin. Temperature measurements were taken in the free stream as well as at eight locations on the fin. The spatially varying (local) heat transfer coefficients were then estimated by minimizing the squared differences between calculated (finite difference) and measured temperatures. The same research team (Chen, Lin, & Chang, 2018) expanded on this work to study the natural

convective heat transfer on a rectangular fin in a heated cavity, and how to best model it in CFD. First their inverse methods and experimental measurements were used to determine the heat transfer coefficients. Then, the same situation was modeled in CFD under different model settings and the calculated fin temperatures were recorded. Finally, the most appropriate CFD models and solvers for the problem were determined by comparison of the experimental and CFD results.

The thermal boundary condition case has also been extended to design problems, where desired surface temperature and heat flux values are specified (and treated as "experimental data") and the question is which system input values (heat strength) create the desired behavior. The inverse thermal boundary determination problem is ubiquitous with inverse heat transfer, so there are many related cases in literature. (Li & Yan, 2000), (Zhang et al., 2016), (Zueco et al., 2005),

Identification of Flow Obstructions. In some cases, one may be interested in inversely understanding upstream fluid conditions. In the biomedical field, for example, intervascular flow obstructions such as blood clots and plaque buildup are blood flow obstructions with deadly consequences.

Alvarez, Conca, Lecaros, and Ortega (2008) developed a numerical procedure to identify the shape and size of an arbitrary rigid body immersed in a steady, viscous cavity flow by downstream fluid velocity measurements. Through robust mathematical derivation and two-dimensional inverse modeling, they successfully demonstrated that Cauchy force and velocity data may recreate, with some confidence, the size and location of the flow obstruction. Karageorghis and Lesnic (2020) similarly developed a general framework for identifying the size and shape of an upstream flow obstruction in an

annular incompressible flow based on fluid velocity measurements. They recognize that the solution is highly unstable and sensitive to error in measurement data.

Identification of Heat and Contaminant Sources. Another modern application of inverse fluid mechanics is the identification and qualification of air and water contaminant sources, particularly in indoor environments. Matsuo, Shimadera, and Kondo (2019) developed inverse methods for identifying the location and emission rates of some flow field contaminant source for the cases of one and multiple sources.

The optimization methods employed in most of these cases are only relevant for the identification of system inputs which are continuous (not discrete). If the research question is whether a known physical component significantly contributes to the experimentally measured fluid velocity, there are only two discrete forward modeled cases to test: physical component present and physical component not present. In this simple case, the optimum would be taken as whichever best recreated the experimental findings. Therefore, inverse analyses of actual engineered systems with well-understood geometries, operating conditions, and governing physics can take a different, simpler approach.

Another inverse modeling approach, which will be employed in this work, consists of parametric forward modeling and regression analysis. For situations where the system and the system behavior are largely understood, it is possible to solve the "forward problem" by creating a representative system model and validating it against experimental data or published results. Parametric application of reasonable system inputs and their values are iteratively applied to the validated model, and the theoretical system response recorded. How the simulated system responds due to changing input

parameters can inform which input values (or combinations thereof) best represent or recreate the actual system behavior. (Jaluria, 2020)

As an example, consider a case seeking to understand the cause(s) of a system's thermal response due to N input parameters P_j (for $j = 1 \ldots N$) and where system temperature measurements from M sensors Y_m (for $m = 1 \ldots M$) are available, the inverse problem is solved by minimization of objective function $S(\boldsymbol{P})$. If vectors $\boldsymbol{P}$ and $\boldsymbol{Y}$ contain the estimated and measured temperature at each sensor m, the objective function can be written as (1) which is the sum of square differences between the measured temperatures Y_m and the estimated temperatures $T_m(\boldsymbol{P})$. The estimated temperatures are obtained from solution the forward model for some parameterization (set of estimates on the unknowns). (Osiki, 2000) By parametric forward modeling and inverse modeling by minimization of the objective function, the inverse problem is solved with the result being estimates of the N unknown parameters P.

$$S(\boldsymbol{P}) = \sum_{m=1}^{M} [Y_m - T_m(\boldsymbol{P})]^2 \tag{1}$$

2.2 Computational Fluid Dynamics (CFD)

Computational fluid dynamics is a branch of fluid mechanics which calculates numerical solutions to the complex systems of equations which describe fluid flows including the conservation of mass, momentum, and energy. The Navier-Stokes equations, which are partial differential equations that govern Newtonian fluid flows, can only be solved analytically in a few simple cases. Therefore, the power of CFD is that fluid mechanics analyses of large, complex, and diverse systems are possible by applying

numerical methods with modern computing (Munson, Okiishi, Huebsche, & Rothmayer, 2013).

A computer generated (CAD) model of the fluid volume of interest is prepared for CFD by defining its boundaries (surfaces) and subsequently discretizing the geometry into small, finite elements called cells. The partial differential equations of the Navier-Stokes equations are likewise discretized into sets of algebraic equations for each cell. The result of this discretization is a finite set of much simpler equations which relates the calculation of one volume element (cell) to the calculated value of its neighboring cell. Thermophysical fluid properties (such as fluid density and viscosity) and boundary conditions (such as inlet flow rates, pressures, and wall shear conditions) are also applied to the numerical domain. Finally, calculation of the discretized equations at each cell location are performed. Due to the form of the discretized equations, the flow field values (fluid velocity, pressure, temperature, etc.) of a particular cell is dependent on the flow field values of adjacent cells. Therefore, all CFD calculations are performed iteratively so that changed (calculated) values at each cell can propagate to its neighbors; effectively "updating" each cells' values for the following calculation. Iterative calculations repeat until (ideally) the flow field solution across the entire domain is no longer changing with subsequent calculation. In the limit of infinitesimally small cells, iterative calculation of the Navier-Stokes equations across the full domain estimates (approaches) the actual continuum flow field. For the case of time dependent (transient) models, the time domain must also be initialized and discretized; and the spatially meshed flow field is calculated at each discretized point in time.

One of the first successful demonstrations of CFD to solve the Navier-Stokes Equations was by researchers at Los Alamos National Laboratory in the 1950's. The research team successfully developed a variety of two-dimensional, transient (time-dependent), incompressible models using in-house code (Johnson, 1996). Numerical solution of a generalized three-dimensional flow was presented shortly after in 1967. Hess and Smith presented the finite-element definition of potential external flow around arbitrary three-dimensional bodies (Hess & Smith, 1967).

Commercial CFD programs first developed in the 1980's and 90's have replaced the "custom" CFD codes of the late 1960's. In some cases, limited CFD packages are offered as an integrated feature to computer aided design (CAD) or parametric solid modeling programs. SolidWorks CFD (Dassault Systèmes SolidWorks Corporation, 2020) and Autodesk CFD (Autodesk Inc., 2020) are two examples which interface basic CFD modeling within their base CAD 3D-modeling programs. The CAD-embedded CFD options may be a convenient option for engineers who have preexisting experience with the base programs and who require only the simplest fluid mechanics modeling. A popular and cost-effective option for stand-alone CFD modeling is the open-source program OpenFOAM (OpenCFD Ltd., 2019). In addition to the free download, OpenFOAM has a large, active community which allows collaboration with other users from industry and academia. COMSOL CFD Module (COMSOL Inc., 2020) has "semi-robust" fluid mechanics capabilities in addition to its multi-physics features such as solid-mechanics and electromagnetism modeling (Resolved Analytics, 2019). There are two industry leaders which offer comprehensive CFD packages: ANSYS Fluent (ANSYS Inc., 2021), and, as is applied in this work, Star-CCM+ (Siemens, 2021). Both Fluent and

Star-CCM+ offer a multitude of accurate and validated fluid physics including various turbulence models and transient time models, as well as built-in meshing or discretization capabilities (Resolved Analytics, 2020). In addition to their ease of use, these commercial software options also boast graphical user interfaces and built-in analytics and visualizations which aid in quality result post-processing. Ultimately, the choice of CFD program depends on the required simulation accuracy and problem physics.

2.3 Case Study – ProtoDUNE-SP Neutrino Detector

The cryogenic ProtoDUNE-SP neutrino detector is introduced here in the context of the international physics experiment DUNE. Then, relevant details of its design and operation are introduced. Accomplishments and shortcomings of previous detector CFD models are given and are then related to the motivation for this work.

2.3.1 The DUNE Experiment

The Deep Underground Neutrino Experiment (DUNE) is an international particle physics experiment under the leadership of the U.S. Department of Energy's Fermi National Accelerator Laboratory (Fermilab) and the European Organization for Nuclear Research (CERN). The collaboration, which consists of researchers from over 180 institutions across 30 countries, works together on all aspects of the conceptualization, design, operation, and analysis of the experimental systems and processes necessary to investigate the subatomic particle called the neutrino. It is hypothesized that a better understanding of neutrinos and their behavior may help answer fundamental questions about the origin and stability of matter—effectively revolutionizing our understanding of the universe. (Fermi National Accelerator Laboratory, 2020b).

Neutrinos are the most abundant subatomic particle in our universe, but since they are so incredibly small and rarely interact with matter, they are not well understood. Neutrinos are so small, in fact, that up until recently, they were thought to be entirely massless (Fermi National Accelerator Laboratory, 2020a). The DUNE project aims to experimentally generate and send a source ("beam") of neutrinos to a large, controlled environment ("neutrino detector") where the neutrinos can be captured and their behavior observed (Fermi National Accelerator Laboratory, 2020c).

Figure 5 shows an overview of the full-scale experiment which is currently in development. The main principle of the experiment is that observable neutrino-matter interactions can take place by intersecting a dense neutrino source with a highly pure, controlled environment of liquid argon called a neutrino detector. The neutrino source or beam for the DUNE experiment begins at Fermilab in Baltiva, Illinois in the proton accelerator called PIP-II. Here, a source of positively charged subatomic particles (protons) are propelled by a series of powerful electromagnets which continually add speed and energy to the protons as they pass through the 700-foot-long pathway. By the end of the initial accelerator pathway, the protons travel at 84% the speed of light, and strike a cylindrical "target" of graphite, releasing neutrinos (neutral) and other particles (charged). Leveraging the charged particles released in neutrino production, a set of electromagnets then focuses the beam along a precise, underground path. In its first two thousand feet of travel, the neutrino beam descends about 200 feet, passing through the first neutrino detector called the near detector. After being measured in the near detector, the neutrino beam passes through an additional 800 miles of earth before reaching the Sanford Underground Research Facility (SURF) in Lead, South Dakota which houses the

Long Baseline Neutrino Facility (LBNF) (Fermi National Accelerator Laboratory, 2020c). At LBNF at SURF, the beam encounters the active volume (LArTPC) of the "far detectors" where the neutrino interactions with matter (the cryogenic liquid argon) can be recorded and reconstructed with "image-like precision." (The DUNE Collaboration, 2020)

By observing neutrino behavior at both the near and far detectors under different source conditions, DUNE researchers hope to gain a new understanding of neutrinos and answer fundamental questions in particle and astro-physics.

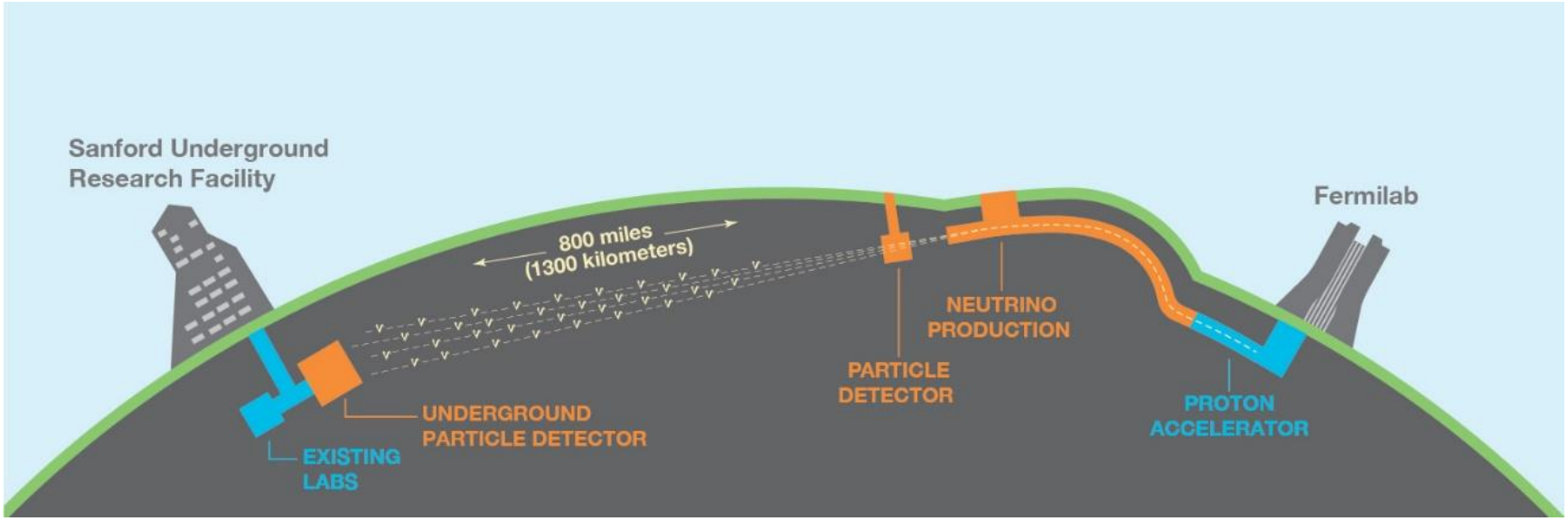

Figure 5. Overview of the components of Deep Underground Experiment (DUNE), (Fermi National Accelerator Laboratory, 2020a).

2.3.2 The ProtoDUNE-SP Detector

Significant engineering effort has been dedicated to the design and testing of the full-scale cryogenic, liquid argon (LAr) neutrino detector and its supporting systems. The Single Phase ProtoDUNE detector is a scale prototype of the LBNF far detectors. The goal of ProtoDUNE-SP is to demonstrate and finalize component design, operation, instrumentation, and data analysis for the full-scale detectors.

The ProtoDUNE Single Phase (ProtoDUNE-SP) detector is a large, insulated pressure vessel which consists of state-of-the art technology and instrumentation submerged in liquid argon. The roughly-cubic inner volume—called the cryostat—holds nearly 600 cubic meters of argon, of which roughly 94% is liquid and the remaining 6% gaseous ullage (GAr) layer to allow for expansion and changes in LAr level. During normal operation, argon temperature and purity is maintained by the adjacent cryogenic filtration system which continually suctions off 1.668 kg/s liquid argon, purifies and cools it, before pumping it back into the cryostat (Figure 3). An external view of the detector is shown in Figure 6.

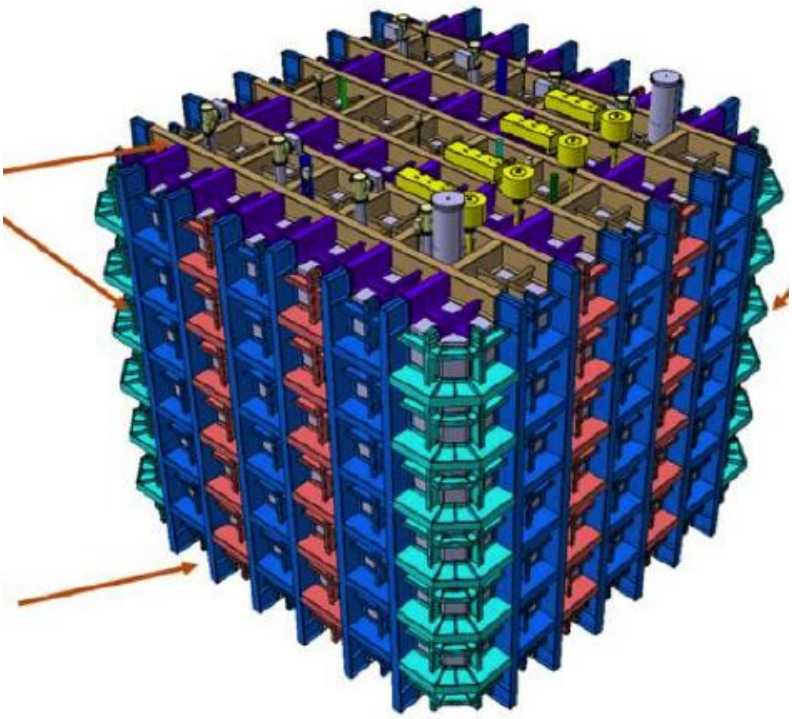

Figure 6. External structure of the ProtoDUNE-SP neutrino detector.

The cryostat components directly associated with neutrino detection make up the time projection chamber (TPC). The TPC, defined by the set of field cages, encapsulates most of the LAr volume since this is where neutrino-argon interactions can be observed. Electrically charged panels suspended vertically in the fluid (positively charged anode plane array (APA) and negatively charged cathode plane array (CPA)) create an electric field to direct the motion of neutrinos interactions in the TPC. Given the argon is adequately pure, neutrinos which enter the inner detector may interact with the relatively large argon atoms giving off light ("scintillation") and negatively charged ionization electrons. The negative electrons are repelled from the like-charged CPA towards the oppositely charged APA at either extent of the TPC volume, as data acquisition in the APA record the horizontal movement "drift" behavior over time, as shown in Figure 7. This whole process of interaction, drift, and data acquisition happens incredibly

quickly—with the goal (minimum) drift time of 3 milliseconds. (The DUNE Collaboration, 2017)

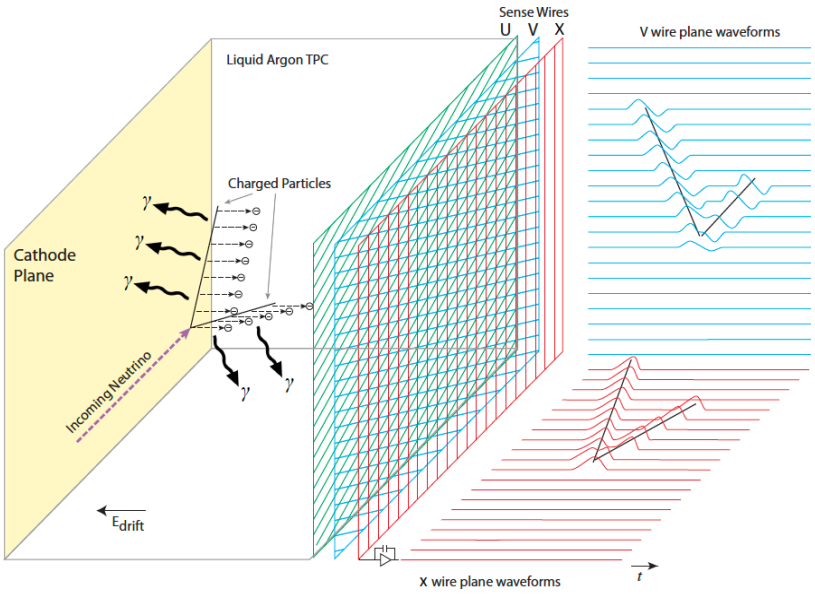

Figure 7. The working principle of neutrino detection in the ProtoDUNE-SP detector. Negatively charged particles released by neutrino interaction with argon are repelled from the like-charged CPA (left) towards the oppositely charged APA (right). (The DUNE Collaboration, 2020)

Impurities such as water and oxygen molecules threaten to absorb neutrinos or otherwise interfere with released particle drift behavior—shortening the drift time. Therefore, the experimental impurity monitors are a vital component in monitoring experimental conditions. Similarly, continual fluid temperature measurement assists with monitoring system operations and detecting abnormal events which may interfere with the experiment.

The impurity and temperature sensor placements throughout the ProtoDUNE-SP cryostat are shown in Figure 8. Experimental temperature data for the two vertical sensor arrays and the 12 “pipe” probes have been provided in support of this research. The “static” or “Valencia” temperature profiler, as it is called, consists of 48 sensors vertically arranged within a protective cage. The “dynamic” or “Hawaii” temperature profiler

captures temperature at 24 vertical locations by translating a set of temperature sensors along a vertical railing system. The Valencia and Hawaii instrumentation both take the namesake of the institutions (universities) responsible for their design— Institute for Corpuscular Physics (IFIC) of Valencia, Spain, and University of Hawaii of Honolulu, HI, respectively.

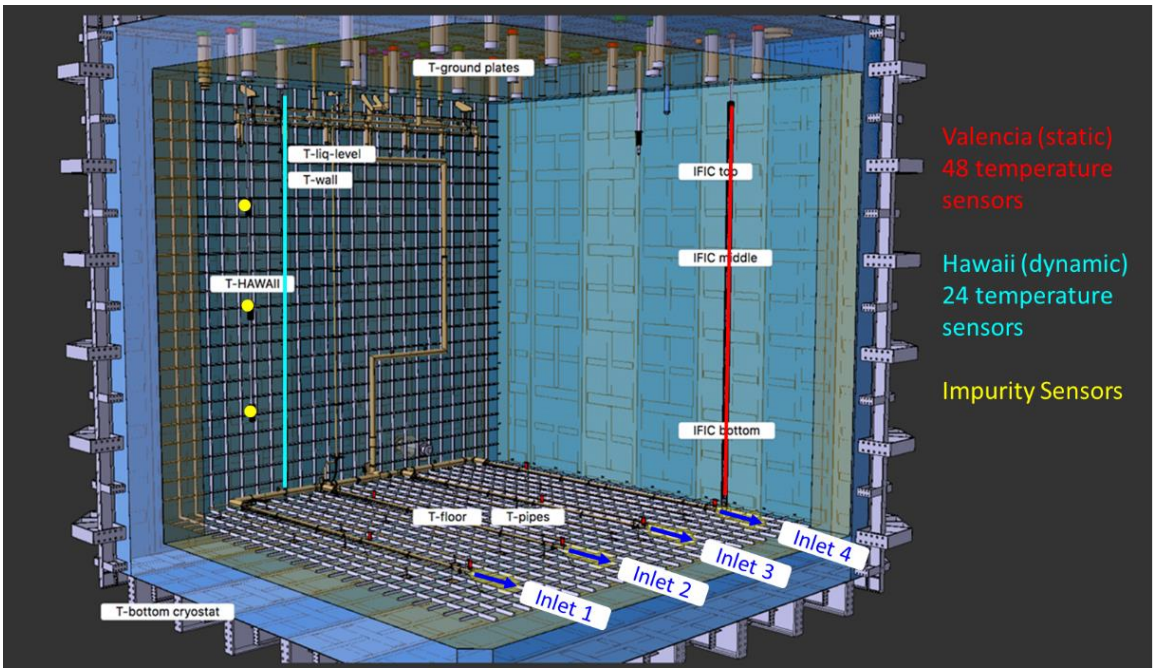

Figure 8. Location of Valencia and Hawaii temperature sensor arrays, adapted from Cervera (2019).

2.3.3 Previous ProtoDUNE-SP Modeling

Collaborators with the Thermal and Fluids Engineering groups at Fermilab were the first to investigate the ProtoDUNE-SP detector with CFD. In particular, Fermilab mechanical engineer Erik Voirin established the fundamentals of modeling both the liquid and gaseous regions in the program ANSYS CFX. He successfully demonstrated his modeling procedures through many investigations of various prototype detectors,

including preliminary designs of the LBNF detector (Voirin, 2015) and the 35-ton prototype detector (Voirin, 2016).

Expanding upon Voirin's work, South Dakota State University researcher Propst (2017) independently developed initial CFD modeling procedures for the ProtoDUNE-SP liquid region in Star-CCM+. Major accomplishments included simplifying the physical geometries of the cryostat, determining appropriate physics models for the fluid, and representing the more geometrically complex components (APA, ground planes, and FC) as much simpler porous regions. Since the simulation work predated experimental procedures, Propst's work was successfully validated against Voirin's CFD simulations completed at Fermilab.

Propst showed that the fluid flow within the ProtoDUNE-SP cryostat was driven primarily by buoyancy effects or natural convection. The forced (pumped) fluid flowrate into and out of the cryostat is significantly small compared to the buoyancy-induced fluid motion. Through his validated methods, the liquid argon temperature and purity distributions were calculated for steady-state operating conditions.

Pedersen (2019) expanded on Propst's liquid-region modeling work by improving the external insulation heat transfer and completing a boundary condition study of the LAr-ullage interface. In the case of the detector insulation, the temperature-dependent conduction through the insulative layer more accurately captured the heat transfer to the fluid compared to the uniform heat flux condition assumed by Propst. Additionally, an investigation of the thermal and shear representations of the modeled liquid-gaseous interface improved simulated temperature agreement with experimental data. Pedersen determined that a "slip" shear specification and a constant temperature thermal condition

most accurately represented the LAr surface. Since the Pedersen models recreated the experimental temperature distributions so closely, within 5 mK, the modeling procedures of the liquid region are considered valid.

2.4 Key Findings

Relevant conclusions from the presented review on the definition and application of inverse problems and computational fluid dynamics as they apply to the case study of thermal profiles in the ProtoDUNE-SP neutrino detector are summarized here.

- Inverse problems involve using indirect experimental measurements and forward (direct) modeling to estimate unknown system parameters of interest.
- Inverse problem-solving method consists of iteratively: (1) parameterizing the system, (2) forward modeling (theoretical predictions), and (3) inverse modeling through comparison of predicted and actual experimental data.
- Inverse problems are ill-posed (solution existence and uniqueness are not guaranteed) and their solutions are sensitive to error propagation (experimental and computational).
- Fully defining known system information (a priori) can combat inverse problem challenges.
- Computational Fluid Dynamics (CFD) can be used in the forward modeling step of inverse problem-solving of fluid mechanics problems.

- Inverse CFD has been used to identify, locate, and/or quantify heat and contaminant sources as well as flow obstructions. There is codependence between these parameters.
- SDSU's previous modeling procedures of the ProtoDUNE-SP liquid region are adequately validated against experimental temperature data to be used in the forward modeling step of this study.
- It is assumed the validated CFD model is missing key cryostat features (geometric and thermal) which may alter the static temperature profile. Appropriately modeling significant components should improve CFD-experimental temperature agreement.

3 METHODOLOGY

The goal of this thesis is to identify ProtoDUNE-SP cryostat features that may be significantly influence experimentally measured temperature profiles, and thus ought to be included in the liquid region CFD model for accurate thermal profile predictions. To that end, computational fluid dynamics will be applied to identify cryostat flow obstructions and heat sources which significantly impact the experimental fluid temperature profiles—particularly the “static” or “Valencia” profile. Cryostat features which significantly alter (improve) the theoretical-experimental fluid temperature agreement will be considered as potential solutions of this inverse problem.

The application of CFD to solve the inverse problem of thermal profiles in the liquid region of the ProtoDUNE-SP neutrino detector begins with previously validated CFD modeling methods of the system. The governing concepts, simplifying assumptions, and boundary conditions of the validated model are first summarized. Revised techniques for reporting the quasi-steady state temperature solution which were applied to generalize comparisons between simulations and to gain statistical information on the solution steadiness are then presented. Actual cryostat features which may be significant to the theoretical fluid temperature predictions are then identified based on their existence in the experiment and proximity to the experimental temperature probes. These flow obstructions and potential heat sources are then applied by parametric changes to the geometry and boundary conditions of the base cryostat representation in CFD. Forward modeling of each parameterization is carried out by applying the changes to the base LAr CFD model and calculating the fluid temperature solution in Star-CCM+. The inverse

modeling step consists of quantifying the temperature profile agreement between the CFD solution and the experimental data.

Generalized trends between model input parameters and temperature agreement/ error are observed. Finally, global minimums of the temperature error within the parameterized results are identified, and the corresponding system representation (or model inputs) are considered potential solutions to the inverse problem.

3.1 Forward Modeling the LAr Cryostat in CFD

The sealed, internal volume of the ProtoDUNE-SP neutrino detector is called the cryostat. During normal operation, the cryostat is full of extremely cold and extremely pure argon. Of the roughly cubic internal volume, 94% of the cryostat's 7.9-meter height is comprised of liquid argon. Gaseous argon (called the ullage) lies above the liquid region and comprises the remaining 6%. Since the LAr region is the primary interest of this investigation, only the bottom 94% (7.40m) of the detector is modeled in this study. The ullage, physical components within the ullage, and the insulation volume surrounding the ullage are not considered in the CFD model.

The liquid argon (LAr) region of the ProtoDUNE-SP neutrino detector cryostat has been previously modeled in CFD (Propst, 2017) (Pedersen, 2019), and their modeling methods are employed here as the "forward modeling" step of the inverse problem solution. There are three major types of regions within the preexisting CFD model: (1) the outer insulation which holds the fluid and is in contact with the surrounding room-temperature air; (2) the LAr which is contained within the insultation; and (3) the physical cryostat components submerged in the liquid. Each region type has unique

geometries, boundary conditions (or operating parameters), and physics models governing its behavior in the CFD simulation. The CFD model set up for this quasi-steady state, turbulent, natural convective flow is presented here.

3.1.1 Geometry Simplifications

The insulation assembly is constructed of multiple layers of structural steel, insulative panels, adhesives, and an internal liquid-tight barrier called the "inner membrane" or "inner walls." The complexities of the insulation's construction are not significant to the fluid modeling since the many layers do not provide either significantly large thermal conduction or thermal resistance. Rather, the insulative structure is simplified to an isotropic, uniform-thickness (0.8m) material which surrounds all sides of the modeled fluid. The inner-most layer of the insulation is the "inner membrane" which is in direct contact with the fluid. Although these inner walls are actually corrugated stainless steel, the corrugations are quite small relative to the scale of the fluid volume and thus are neglected in the CFD model (i.e., walls are assumed smooth). The bottom, inner wall defines the y = 0m for the model (with x = 0m, z = 0m centered on the 8.548m square face). Figure 9 shows cross-sectional views of the actual and simplified insulation assembly.

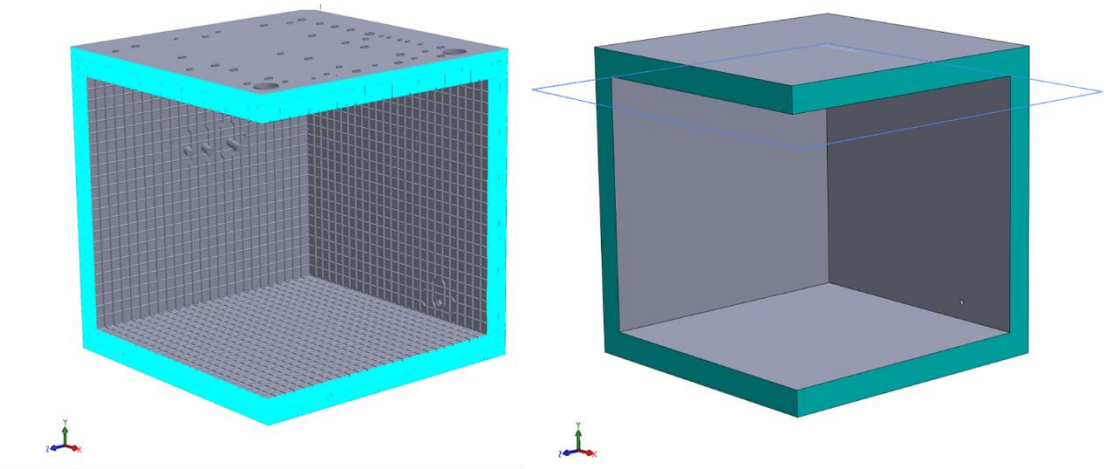

Figure 9. Cross sectional views of the actual (left) and simplified (right) insulation geometry. Plane on right is the location of the LAr ullage interface.

Also shown in Figure 9, is the location of the LAr-ullage interface. In this work, only the LAr and corresponding components are modeled (i.e., everything that lies at or below this reference plane). Everything above the plane, such as the ullage fluid, physical components in the ullage, and the insulation surrounding the ullage are not modeled. Therefore, this interface is the top surface of the modeled LAr and defines the equilibrium condition between the liquid and gaseous ullage regions where the LAr "boils off" into the ullage. Further details of the interface representation are discussed in subsequent sections.

Within the inner membrane of the insulation, there are many complex physical components submerged in LAr, each with unique functions (Figure 10). The subset of LAr volume where neutrino interactions are observed called the time projection chamber (TPC). On both the +z and -z extremes of the TPC are vertically oriented planes of electrically charged wires meshes which comprise the anode plane assemblies (APAs). The cathode plane assembly (CPA) is oriented parallel to and equidistant from each APA,

defining the center of the TPC. During the experiment, the positively charged APAs and the negatively charged CPA create an electric field which directs the motion of neutrino interactions towards the center of the TPC. Essential to directing and containing this electric field is the field cage (FC) which constitutes the other four walls (+/- x and +/- y sides) of the TPC volume. The FC panels act as a Faraday cage to effectively shield the TPC electric field. The FC panels, which are constructed of long, parallel ellipsoid bars, are not completely solid, and thus allow some fluid to pass through (much like the wire-mesh of the APAs). The ground planes (GPs) lie exterior to TPC—one above (y = 7.02m) and one below (y = 0.45m) of the horizontal FC panels. The GPs (shown as yellow and

blue Figure 10) are large, thin sheet metal assemblies with a grid-pattern of 6mm-diameter holes throughout.

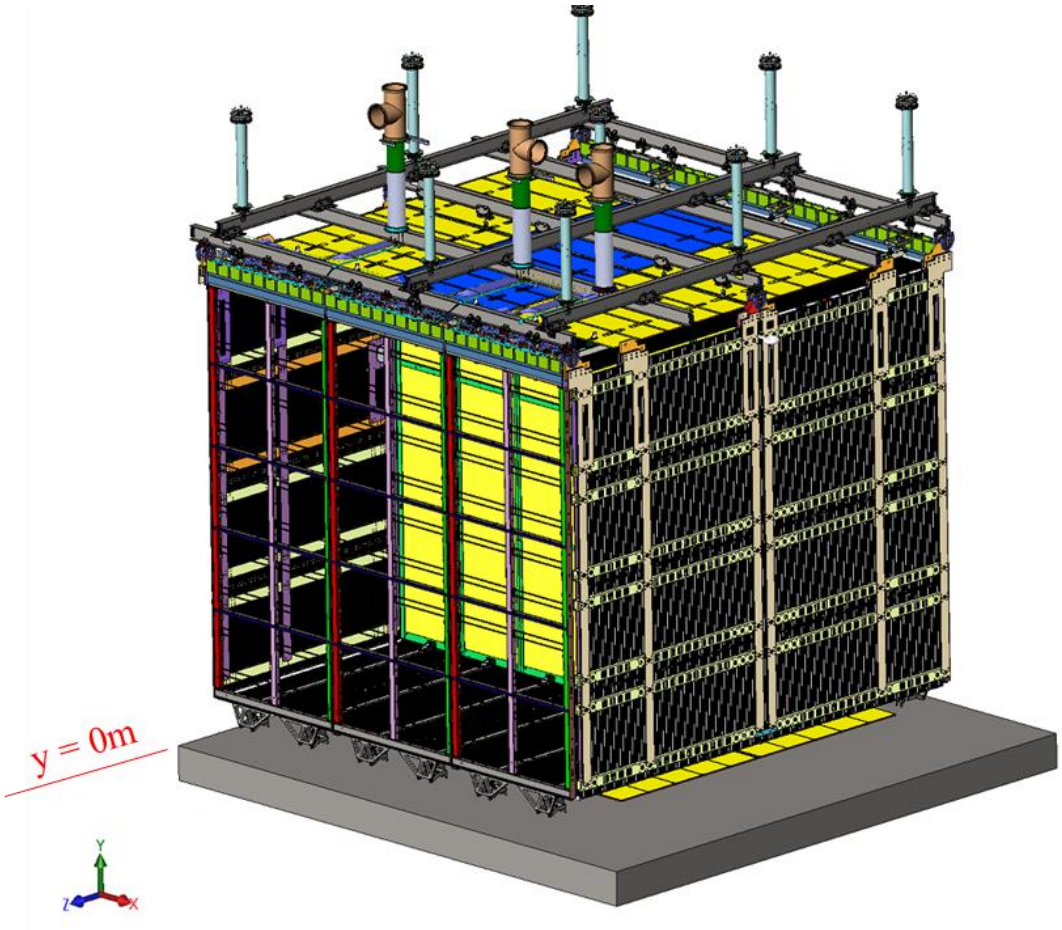

Figure 10. The physical geometries within the cryostat are too complex to model in their entirety. The bottom (gray) component represents the bottom wall (floor) of the inner membrane; its bounds in the x and z directions represent the locations of the inner walls.

Propst (2017) was responsible for many of the geometric simplifications to the internal geometries. The simplified framing which supports the FC and APAs are pictured in Figure 11. Like the framing, the modeled CPA is smooth and impermeable to fluid flow. The other primary geometries, however, are not completely solid. The FC, APA, and GP panels each have relatively small geometrically repeating features which allow some fluid flow through the regions. As such, each of these is modeled as

representative porous region with a volumetric footprint of their full geometries. The simplified porous regions of each are shown in Figure 12. In the case of the field cage (FC) and anode plane assemblies (APAs), the porous region volumes completely fill their impermeable frames, and are flush with the frame surfaces. The ground plane porous regions are similarly smooth and flat, but do not have any impermeable framing or supports. The model specifications which constrain the fluid flow through the porous regions (viscous and inertial resistances; porosity) are based off the actual, complex geometries and are detailed in the *Boundary Conditions* section.

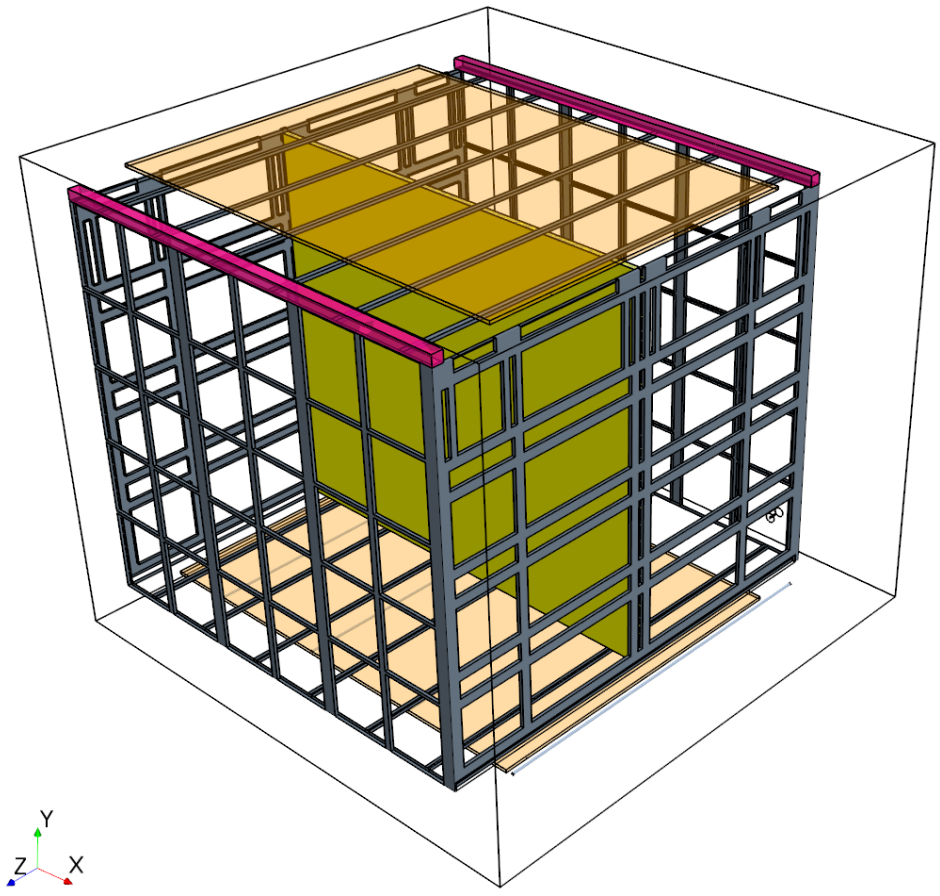

Figure 11. CFD geometry impermeable components: framing (gray), cold electronics (pink), and CPA (yellow).

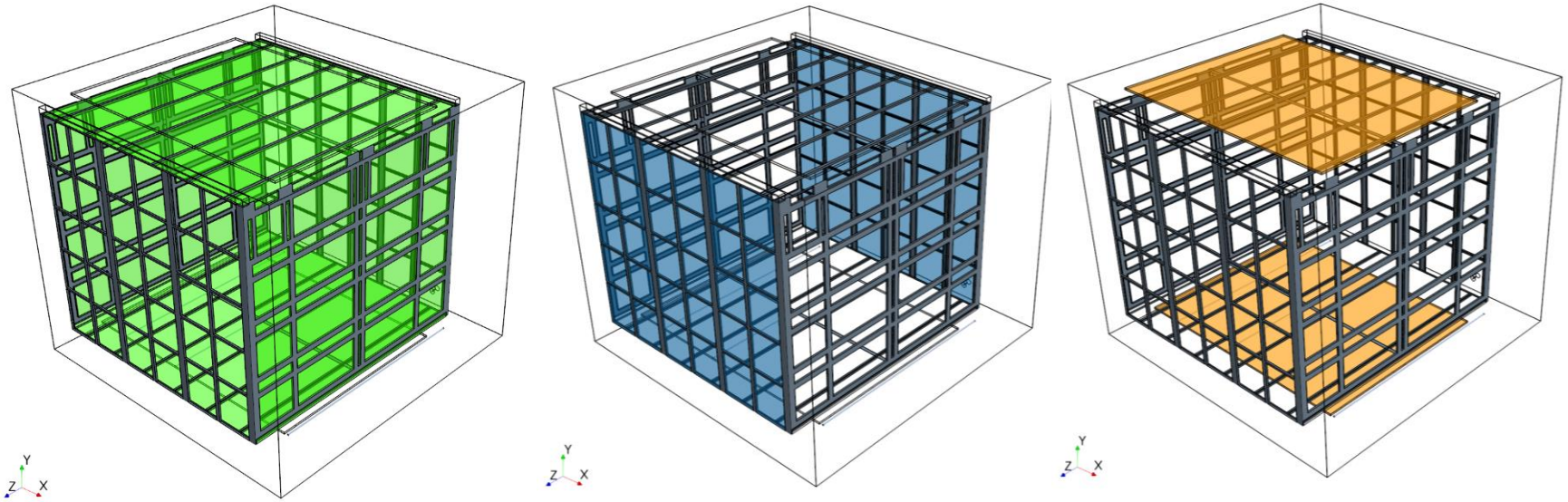

Figure 12. CFD geometry of porous components (from left to right): field cage (FC), anode plane assemblies (APAs), and ground planes (GP).

Liquid argon (LAr) completely fills the inner insulation boundary, surrounding all physical components within the bottom 7.40 meters of the cryostat. Assumedly pure LAr from the external cryogenic filtration system is pumped into the cryostat in the positive z direction through four, 38.4mm diameter pipes located below the bottom ground plane (y=0.24m). The inlet pipes were previously not modeled in Propst's (2017) and Pedersen's (2019) work. However, to accommodate heat transfer from the pipes, the horizontal, 6-meter-long pipes, which extend in the negative z direction from the inlet surfaces, were included. LAr is simultaneously pumped out of the cryostat (in negative z direction) by one 154mm diameter pipe ("suction valve") on the bottom of the negative z wall (y=0.70m). The modeled outlet was altered slightly from the existing CFD models to alleviate some continuity convergence issues. Starting from the LAr outlet surface an outflow stream (representative of the exiting pipe) was extruded in the -z direction by 2m such that the modeled outflow extends beyond the exterior insulation boundary.

Cold electronics (CE) boundaries were also added to accommodate newly provided heat transfer boundary conditions. Near the LAr surface and inline with the top edge of the +z and -z APA frames, are arrays of closely spaced electronics modules running the entire width of the APAs (Figure 13). The small spaces between adjacent CE modules were neglected due to their relatively small size, and instead solid beams of their approximate outside footprint (0.18m square) were modeled to represent the CE flow obstructions. The heat source thermal condition was supplied by DUNE researchers and is discussed in more detail in the *Boundary Conditions* section.

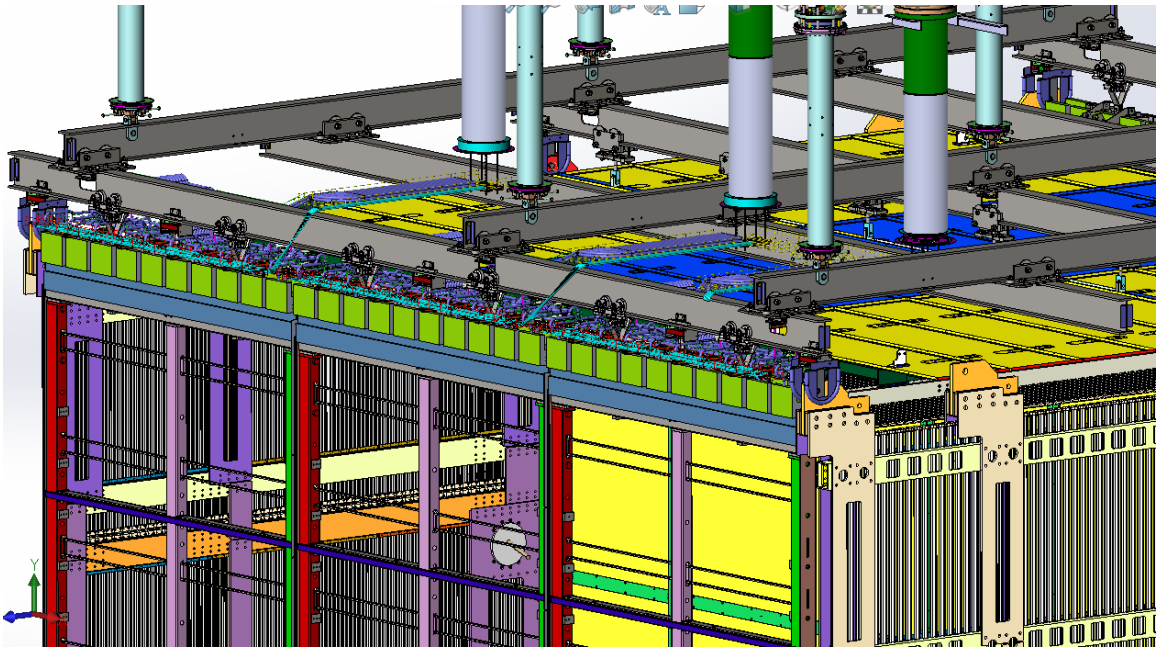

Figure 13. Model of actual cold electronics geometry (green boxes).

The physical geometries of the temperature profiles of interest, Valencia and Hawaii, were neglected, but computational datums were defined at the same locations as the experimental sensors. Table 2 lists the location of each vertical sensor profile and the number of sensors in that profile.

Table 2. Location and number of modeled temperature and impurity sensors.

	X Location (m)	Z Location (m)	Number of Vertical Datums
Valencia (static temperature profile)	3.41	2.759	46
Hawaii (dynamic temperature profile)	-1.98	-3.578	20
Impurity Probes	-3.00	-3.574	3

Figure 14 shows the full, simplified detector geometry as modeled for CFD simulations with important regions and features labeled. The governing concepts, physics conditions and fluid properties applied to these geometries are detailed further in the following section.

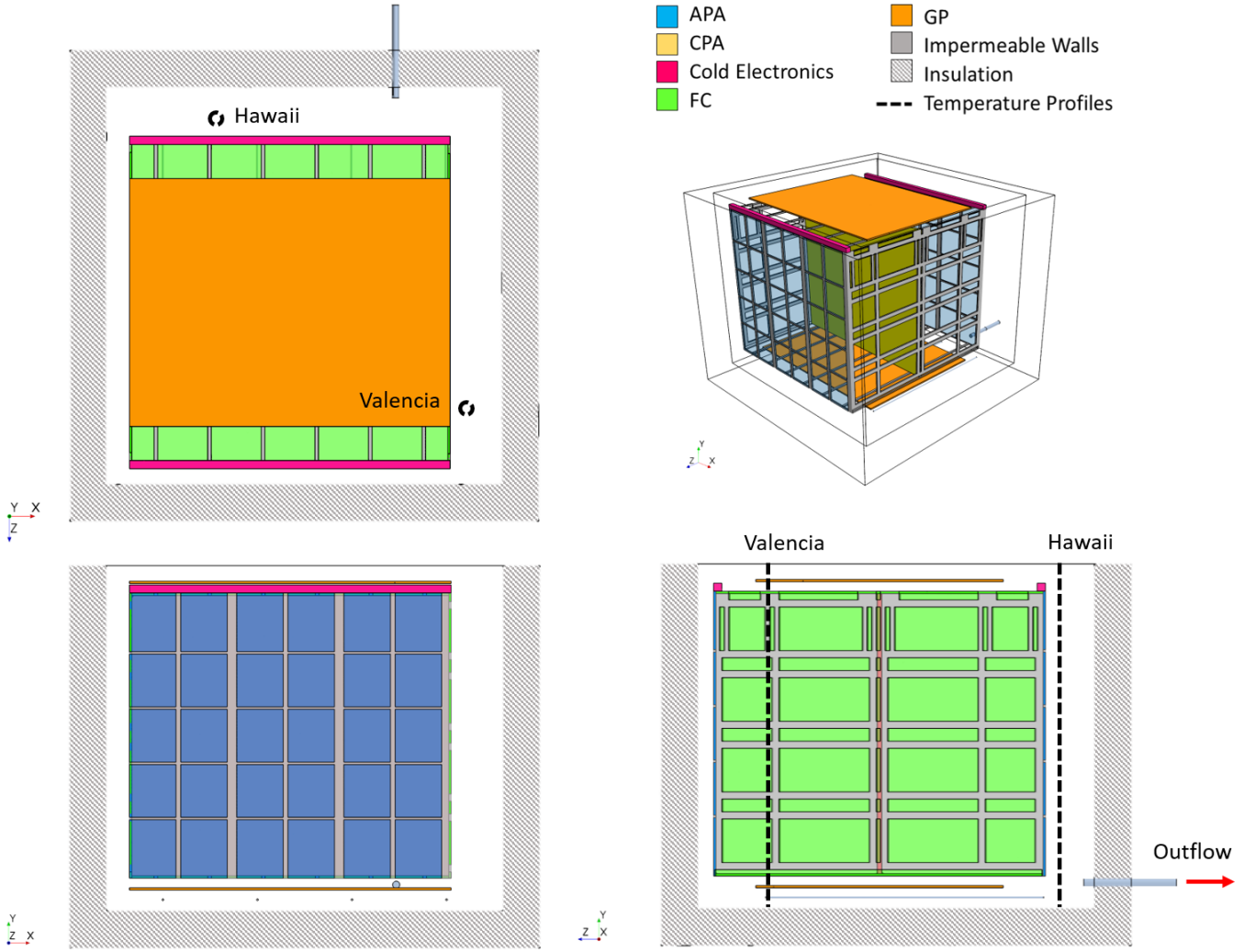

Figure 14. Simplified geometries in base CFD model. Temperature profiles Valencia and Hawaii are main basis of comparison with experimental.

3.1.2 Physics

The fluid flow in the LAr region is calculated through the numerical approximation of the following equations. The Continuity Equation ensures that mass is conserved, and the Navier-Stokes equations govern the conservation of fluid momentum. Together, when coupled with the Energy Equation and the simplifying Bousinessq approximation, these equations fully account for the intrinsic relationships between fluid velocity, pressure, and temperature.

Governing Equations

The Continuity equation, or the conservation of mass, enforces that fluid is not created or destroyed in a fluid mechanics process. For Continuity to be satisfied, the time rate change of fluid within the control volume must be balanced by the corresponding inflow(s) and outflow(s). Equation 2 gives the differential form of the Continuity equation.

$$\frac{\partial \rho}{\partial t} + \frac{\partial \left(\rho u_j\right)}{\partial x_j} = 0 \tag{2}$$

The Navier-Stokes equations, or the conservation of momentum, balance the forces (shear, normal, and body forces) experienced by a fluid element in motion based on the fluid velocity components (i.e., Newton's Second Law applied to the fluid). Equation 3 gives the Navier-Stokes equation for a viscous Newtonian fluid.

$$\rho \frac{D\vec{V}}{Dt} = -\vec{\nabla} P + \mu \nabla^2 \vec{V} + \rho \vec{g} \tag{3}$$

The Energy equation, or the conservation of energy, is the application of the First Law of Thermodynamics to the fluid problem. For some differential fluid element, the energy equation (4) balances the heat transfer to the fluid; work done by the fluid due to body and shear forces; and the temperature of the fluid element.

$$\rho \frac{Dh}{Dt} = \rho \dot{q} + div\left(k\vec{\nabla}T\right) + \tau_{ij}\frac{\partial u_i}{\partial x_j} + \rho\vec{g}\cdot\vec{V} \tag{4}$$

Turbulent fluid flows are inherently unsteady, and an exact steady-state solution does not exist. For numerical approximations of these flows, though, turbulent fluctuations about a field mean are calculated with the Reynolds-averaged Navier-Stokes (RANS) equations resulting in a so-called "quasi-steady state" solution. The particular RANS turbulence model used in this work is the K-Omega SST Menter model. The reader is encouraged to consult Propst (2017) for a detailed comparison of turbulence models for natural convective flows.

Natural Convection Simplification

The bulk flow in the LAr region is driven by natural convection. In natural convection, changes in fluid density (due to changes in fluid temperature) cause buoyancy gradients, which in turn causes fluid motion as the system seeks equilibrium. The Boussinesq approximation is often employed for natural convective flows where the thermal expansion coefficient is large for small temperature differences. In this approximation, it is assumed that all fluid properties are constant except for density. Further, it is assumed that density changes linearly with temperature and only influences the buoyancy term of the Navier stokes equations. Therefore, the gravity physics model was also enabled. The Bousinesq approximation is given by (5) (Nellis & Klein, 2009).

$$\rho_{T=T_\infty} - \rho = -\beta\rho(T_\infty - T) \tag{5}$$

Passive Scalar (Impurity) Representation

The LAr impurities such as oxygen and water molecules, because of their low concentration, are virtually massless and thus do not influence or affect the fluid flow. However, their presence, location and concentration are significant to the physics and success of neutrino detection. Therefore, the impurities are modeled with a passive scalar representation which uses the driving fluid motion to calculate the distribution (or local concentrations) of an arbitrary "passive" fluid constituent. The passive scalar representation of the impurities can be thought of as a colorful dye carried by the flow that does not influence the flow field solution. The convection-diffusion equation which describes the passive scalar transport is given by (6).

$$\frac{\partial c}{\partial t} = \nabla \cdot (D\nabla c) - \nabla \cdot (vc) + R \tag{6}$$

It is assumed that the primary source of passive scalar in the LAr region is the diffusion of contaminants from the ullage region. Therefore, the only non-zero passive scalar boundary condition is a source term at the liquid-ullage interface. After calculation, the resulting impurity distribution is scaled to a known, experimentally measured impurity value.

Liquid Argon (LAr) Representation

The liquid argon (LAr) was modeled as being incompressible (constant density) except as density changes apply to the Boussinesq approximation. All other relevant LAr properties (density, viscosity, specific heat capacity, thermal conductivity, thermal

expansion coefficient, and Prandtl number) were also assumed constant at the values listed in Table 3. The LAr flow field was solved as quasi-steady state with the SST k-ω turbulence model, and by segregating (instead of coupling) the equations for mass, momentum, and energy at each iteration.

Table 3. LAr fluid properties assumed for CFD simulations.

Property	Value
Density	1387 kg/m^3
Viscosity	2.4982E-4 Pa-s
Specific Heat	1118.9 J/kg-K
Thermal Conductivity	0.12647 W/m-K
Thermal Expansion Coefficient	0.0045075 /K
Turbulent Prandtl Number	0.9

Solid Region Representation

The CPA and insulation regions are both solid continua with constant material properties as listed in Table 4. As in the liquid region, the solid continua were solved with a steady-state time scale and with segregated solver settings.

Table 4. Solid continua (insulation and CPA) material properties assumed for CFD simulations.

Region, Material	Density (kg/m^3)	Specific Heat (J/kg-K)	Thermal Conductivity (W/m-K)
Insulation	2702	903	Linear with T
Cathode Plane Assembly (CPA), 320 stainless steel	8055	480	15.1

Summary of Physics Settings

The physics model and solver settings for the liquid (LAr) and solid (insulation and CPA) continua are summarized in Table 5 and Table 6 respectively. In both cases, as is reflected in the tables, selecting certain physics models automatically enabled other models (e.g., selection of the segregated solvers enables the gradients solver).

Table 5. Summary of liquid continua physics model and solver settings.

Physics Model	Selection	Automatically Enables
Space	Three Dimensional	
Time	Steady State	
Material	Fluid	
	Constant Density	
Viscous Regime	Turbulent	Reynolds-Averaged Navier Stokes
	SST (Menter) K-Omega	Exact wall distance, All y+ wall treatment
Solvers	Segregated Fluid Flow	Gradients
	Segregated Fluid Temperature	
Optional Models	Passive Scalar	
	Boussinesq Model	
	Gravity	

Table 6. Summary of solid continua (insulation and CPA) physics model and solver settings.

Physics Model	Selection	Automatically Enables
Space	Three Dimensional	
Time	Steady State	
Material	Solid	
	Constant Density	
Solvers	Segregated Solid Energy	Gradients

3.1.3 Boundary Conditions

Boundary conditions are operational parameters applied to the numerical model which constrain the physics calculations. Some boundary conditions define where and how fluid mass: can or must flow (openings, inlets/ outlets); cannot flow (walls, flow obstructions); or where the flow is restricted (porous regions). Other boundary conditions constrain the thermal behavior of the fluid boundaries with temperature or heat transfer specifications. For this CFD modeling of the LAr in the ProtoDUNE-SP cryostat, all boundary conditions are presented in the context of the simplified CFD geometry and applied physics conditions.

Heat Transfer Through Insulation

Heat transfer by conduction occurs from the warm ambient air (at 26°C), through the insulation and to the LAr. The primary resistance to conduction is the thermal resistance provided by the 0.8m-thick insulative panels—the relatively thin metal membranes do not significantly contribute to conduction. Likewise, any contact resistance between insulation layers is also neglected. Importantly to its representation, the thermal conductivity of the insulation is temperature dependent (Pedersen, 2019). Equation 6 gives the thermal conductivity for the insulation in W/m-K where the temperature, T is in Kelvin.

$$k_{ins} = (1.222\text{E} - 4)T + 0.0048706 \quad (6)$$

Fluid Pumped into and out of Cryostat

LAr is pumped into the cryostat through an inlet manifold system which splits a single source into four (38mm-diameter) horizontal pipes below the -y ground plane (GP)

before discharging the warm LAr into the +z direction. The outer surfaces of the horizontal pipe sections are modeled, and the circular “fluid faces” at each +z discharge define the inlet boundaries.

The total flow delivered by the four pipes is 1.668kg/s, but due to the asymmetric geometry of the inlet manifold system, the mass flow is not split uniformly between the four pipes. An investigation of the inlet manifold system (Figure 15) yielded the mass flow percentages and fluid temperatures listed in Table 7. These flow-split percentages and fluid temperatures are applied as “mass flow inlet” boundary conditions in the LAr CFD model. Since the fluid is supplied to the cryostat after purification, it is assumed that no impurities (zero passive scalar) enter the cryostat through the inlet pipes.

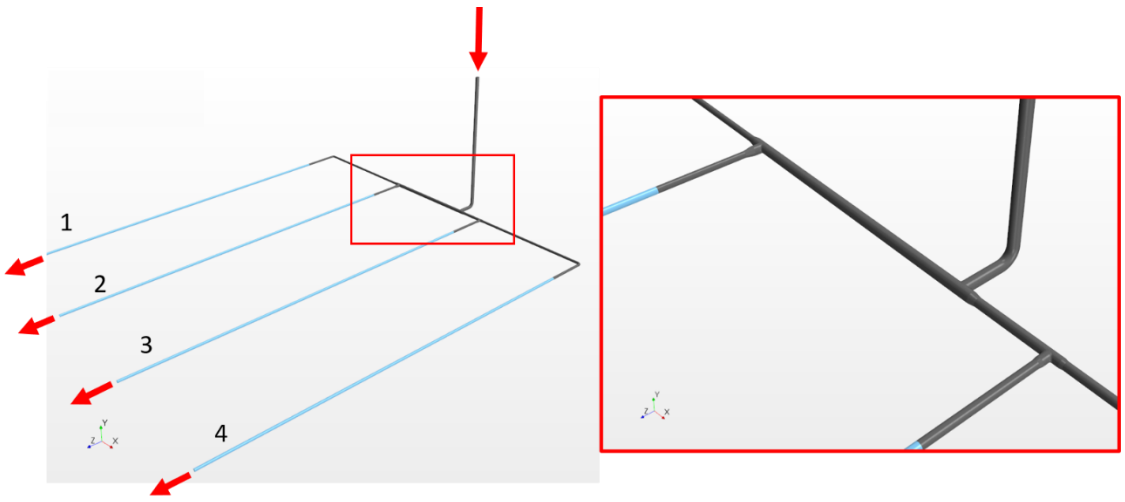

Figure 15. Inlet pipes manifold system is asymmetric. Blue, horizontal segments (1-4) are modeled explicitly in base CFD model.

Table 7. Inlet Boundary Conditions: Mass Fractions and Fluid Temperatures.

	X Location (m)	Flow Rate Fraction (%)	Temperature (K)
Inlet 1	-3.06	25.39	88.219
Inlet 2	-1.02	28.20	88.234
Inlet 3	1.02	21.65	88.203
Inlet 4	3.06	24.76	88.220

There is also forced (pumped) LAr flow out of the cryostat. The single LAr outlet is near the cryostat floor (y = 0.56m) on the -z wall and directs fluid back to the external filtration system. This "flow-split outlet" boundary condition satisfies continuity by enforcing an outlet flow split of 100%.

It is worth noting that previous LAr CFD studies also modeled a "pumps off" cryostat operating condition (flow rate of 0 kg/s). Based on the DUNE researchers' priorities at the time of this study, only the "pumps on" case was modeled in this study.

LAr-Ullage Interface

The division between the liquid (LAr) and gaseous (ullage) argon regions is represented by a smooth, horizontal surface in the LAr CFD model, as previously discussed. This surface, which represents the thermal equilibrium condition between the liquid and gas, is measured experimentally by a so-called "Level Meter." At the time of temperature measurements, the surface was reported to be at a height of 7.40m from the cryostat floor. In the base CFD model, the LAr-ullage interface height is likewise modeled at 7.40m. The smooth surface is modeled as impermeable to fluid flow and the

mass transfer associated with the LAr boil-off into the ullage is neglected since it is small relative to the forced flows.

There are also shear and thermal specifications constraining the LAr at this interface. Pedersen (2019) demonstrated that constraining the surface with a slip shear specification and a uniform, constant temperature equal to the saturation temperature at the ullage pressure best captured the experimental behavior. The slip shear specification effectively deletes boundary layer effects by allowing a non-zero fluid velocity at the surface. The constant interface temperature specification is 87.597K based on an experimentally measured ullage pressure of 1046mbar.

The final boundary condition constraining the LAr-ullage interface is an impurity (passive scalar) source. The prevailing theory amongst DUNE researchers is that the main source of cryostat impurities are components in the ullage region. For example, it is hypothesized that the Teflon electrical wire coatings dissipate impurities at a temperature-dependent rate. If that is the case, and if the ullage-region impurities can drift down to the LAr-ullage interface, they subsequently may propagate into and through LAr region where they threaten neutrino detection. A uniform passive scalar (impurity) in flux of 1.0 kg/m^2-s is therefore applied at the LAr-ullage interface to simulate this phenomenon. Since the actual impurity influx is unknown, the modeled value is arbitrary, but is scaled to the model volume-average to better understand the relative impurity concentrations and spatial distributions.

Solid Geometries

Solid boundaries in the LAr region (such as the inner membrane walls, the CPA, and TPC framing) are defined by impermeable surfaces with a no-slip shear specification. The default thermal specification is thermally conductive, and no heat generated, but solid bodies may be alternatively constrained with temperature or heat source values, as will be the case in parametric variations to the base CFD model.

The cold electronics (CE) on either +/-z APA continually receive electrical power input and dissipate heat to the surrounding LAr. Each of the two CE assemblies reportedly reject 336W. It is assumed that the heat rejection occurs uniformly across the surface of the representative CE rectangular prisms in the CFD models.

The horizontal segments of the LAr inlet pipe manifold which are explicitly modeled (length = 6m) are assumed to reject some heat to the bulk LAr due to frictional losses of the internal pipe flow. Another result of the CFD investigation of the inlet manifold (which produced inlet flow splits) was an estimate of the heat rejected by the inlet pipes. The resulting pipe heat flux as a function of axial location (Figure 16) was applied as a thermal boundary condition in the LAr CFD model.

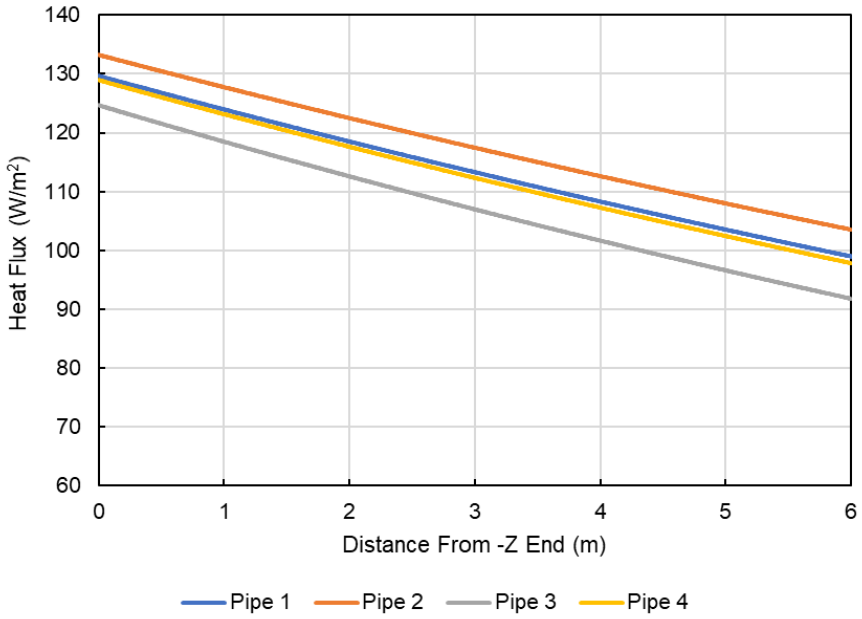

Figure 16. Inlet pipe boundary condition: heat flux with position.

Porous Regions

The APA, FC, and GP regions are each constructed of small and repeating geometries which, if modeled explicitly, would add unrealistic amounts of complexity to the CFD models. Therefore, the regions are instead represented by porous volumes occupying the same footprint. The porous representations effectively recreate the flow restriction that occurs in the actual, full geometry. Propst (2017) derived these porous region constants—viscous and inertial resistances—by simulating flow through small subsections of the actual APA, FC, and GP geometries. The resulting pressure drop versus fluid velocity is a second-order polynomial whose coefficients define the viscous and inertial resistances used here. Table 8 gives the porous region porosities, and viscous and inertial resistances used in the CFD models.

Table 8. Properties of porous regions FC, APA, and GP in CFD model.

Region	Porosity (-)	Inertial Resistance (kg/m^4)	Viscous Resistance (kg/m^3-s)
Field Cage (FC)	0.23	279020	247.38
Anode Plane Assembly (APA)	0.73	11264	118.63
Ground Plane (GP)	0.28	279020	4.67
Cathode Plane Assembly (CPA)	0.00	-	-

Summary of Boundary Conditions

The boundary conditions for the liquid region and insulation region are listed in Table 9 and Table 10, respectively. The porous regions (FC, APA, and GP) interact with the LAr regions through permeable interfaces with no explicit thermal or shear specification.

Table 9. LAr region boundary conditions.

Boundary	Boundary Type	Boundary Condition	Selection
Liquid-Ullage Interface	Wall	Shear Specification	Slip
		Constant Temperature	87.5947 K
		Impurity Flux	1.0 kg/m^2-s (arbitrary, scaled later)
Solid Walls	Wall	Shear Specification	No-Slip
Electronics	Wall	Shear Specification	No-Slip
		Heat Source	336 W (each)
Inlets	Mass Flow Inlet	Mass Flow Rate	Unique, (Table 7)
		Temperature	Unique, (Table 7)
		Impurity	0
Inlet Pipes	Wall	Shear Specification	No-Slip
		Thermal Specification	Heat Flux, varying with position (Figure 16)
Outlet	Flow-Split Outlet	Split Ratio	1.0 (100%)

Table 10. Insulation region boundary conditions.

Boundary	Boundary Type	Boundary Condition	Selection
Outer Walls	Wall	Constant Temperature	26℃
Top (cross section in line with LAr-GAr interface)	Wall	Thermal Condition	Adiabatic

3.1.4 Numerical Solution

Volume Discretization

The previously described model insulation, physical components and LAr regions must be discretized into small, finite volumes (called “cells”) for the computational approximation of the flow fields. The mesh, as it is called, is controlled by a few primary parameters, as presented in detail by Propst (2017). For example, Propst details how certain meshing models (which control the shape and distribution of the cells) are better suited for different flow regimes, and that proper mesh settings are necessary for an accurate, but computationally efficient numerical solution. This balance between efficiency and accuracy is accomplished by increasing the number (and decreasing the size) of cells in locations where the flow field is complex. For the turbulent, natural convection of the ProtoDUNE-SP LAr, the trimmed cell mesher in Star-CCM+ has proven to be both computationally efficient and sufficiently accurate. The trimmed cell meshing model creates rectangular prism (quadrilateral) cells were possible, and polyhedral cells elsewhere, particularly near curved edges. The prism layer specification, which controls the size and distribution of cells adjacent to boundaries, is another important mesh specification. It is important to have many fine cells near boundaries to capture boundary layer (near-wall) effects.

The computational mesh settings for all ProtoDUNE-SP CFD models were based on the validated methods of Propst and Pedersen. The LAr region was discretized by the trimmed cell meshing model with a base size of 7cm and six prism layers. Further refinement of the LAr mesh was accomplished with curve control on all sharp edges having target surface size 25% of the base size; inlet surface refinement having target

surface size 6.25% of the base size; volumetric control in vertical region on +z side of +z APA having target z-direction anisotropic size 50% of the base size; and volumetric control in horizontal regions between (i) the +y FC and the LAr-GAr interface and (ii) the -y FC and -y GP both having target y-direction anisotropic size 50% of the base size. The insulation region was also discretized with a trimmed cell mesh but with base size of 5cm and four prism layers. The APA, CPA, FC, and GP regions were all meshed with a polyhedral "thin mesher" with two thin layers and a 7cm base size. The resulting mesh for the base CFD model (Figure 17) was composed of 8.2 million liquid region cells and 8.9 million solid region cells.

Although forward modeled parameterizations with geometric changes required remeshing (and thus resulted in slightly different cell counts) the mesh settings remained the same between all simulation versions.

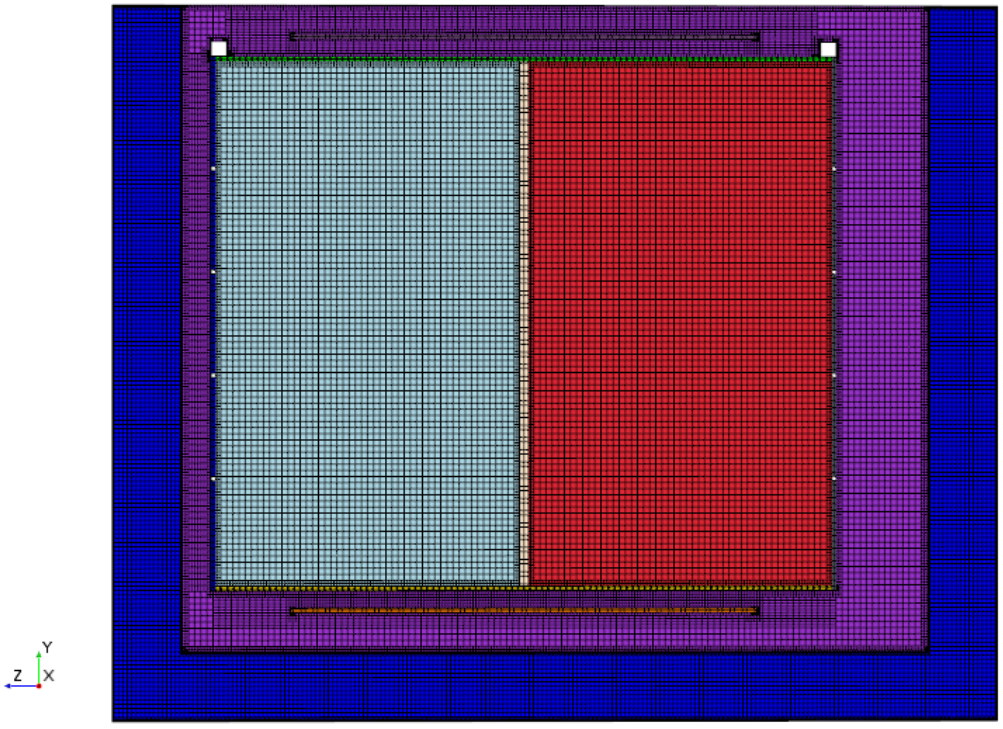

Figure 17. Cross sectional view of base CFD model mesh at x = 0.0m.

Quasi-Steady State Temperature

The main basis of comparison between the CFD and experimental results are the quasi-steady state temperatures, and both the experimental and calculated temperatures are assumed to be time independent, or steady state. Even though turbulent fluid flows are inherently unsteady, and thus change with time, it is computationally prohibitive to model the time effects within the cryostat. Further, experimental observation during normal detector operation has shown that the thermal conditions remain approximately constant with time. Therefore, it is reasonable and computationally economical to neglect time effects by implementing a "steady state" time model. The calculated CFD solution is referred to as a "quasi-"or "semi" steady state because, as previously mentioned, turbulent flows will never truly reach a steady solution; the calculated solution is only an approximate of a hypothetical steady flow field.

The LAr fluid temperature solutions from the Pedersen CFD modeling techniques, although validated against the data available at the time, were found to have significant unsteadiness even at solution convergence. In particular, the local fluid temperature was fluctuating about a central value, even when the "steady" turbulent solution appeared to have converged. Figure 18 shows the slight variations between three temperature profiles for the static, Valencia, probe at three instantaneous "converged simulation" stopping points (in the neighborhood of 100,000 iterations). Therefore, to achieve the desired temperature modeling precision required by the project sponsors, further solution-steadying techniques were implemented. In this new technique, after the simulation had come to convergence (as before), the local temperatures were averaged over a number of iterations, thus "honing in" on the central value. Figure 19 shows the

iteration-averaged Valencia temperature profiles for three different iteration ranges (100, 1,000 and 2,000). Ultimately it was determined that averaging the final 1,000 iterations produced a steady temperature result.

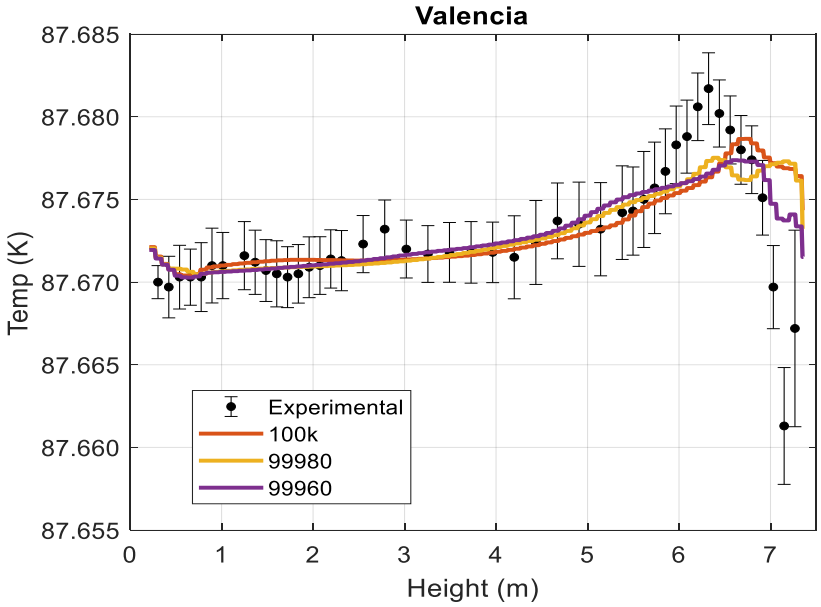

Figure 18. Motivation for iteration-averaged temperature reporting. Previous CFD modeling methods resulted in slight unsteadiness in the temperature solution at convergence.

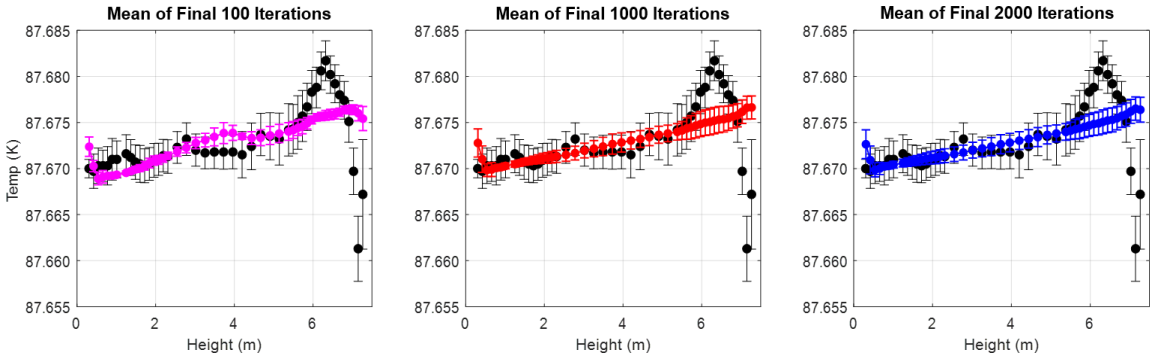

Figure 19. Iteration-averaged temperature reporting steadies the solution by taking the mean of the final 1,000 temperature calculations (iterations).

Instead of reporting one instantaneous, calculated temperature distribution at the end of a sufficient number of CFD iterations, we now have a more consistent way of reporting and comparing calculated temperature fields. Additionally, new statistical information about the temperature solution steadiness at convergence is available.

3.2 Parameterization

To expand upon previous CFD modeling works to solve the thermal profile inverse problem, it is necessary to identify previously neglected cryostat features such as flow obstructions and heat sources which may be significant to the thermal modeling. Newly provided detector operating conditions such as the ullage pressure, the LAr height, and the LAr flow rate distribution were used to update the base model, as previously described. Then, DUNE experiment reports and photos of the detector were reviewed to identify physical geometries and potential heat sources upstream or in close proximity to the temperature probes of interest.

For each simulated case, the previously presented "forward modeling" methods were applied. Physical components, for example, were iteratively added to the base CFD model as impermeable, smooth walls with geometries (volume, external dimensions) and locations approximated from available detector literature. Heat sources were added to new and existing physical geometries by changing the thermal boundary condition on the component's walls to a specified heat value. In practice, the heat source (power) value is then distributed uniformly across the simulated surface area.

Iterative variations of the existence of the flow obstructions and the intensity of the heat sources were carried out in the previously outlined modeling procedures. The thermal profile solutions were then calculated in Star-CCM+ and were stored for data analysis and inverse modeling purposes. Parameterized cases which produced favorable changes to the calculated thermal profiles were noted, and informed other iterations of model changes.

3.2.1 LAr-Ullage Interface Height

The boundary separating the LAr from the ullage is assumed to be smooth, flat, and held at a constant height of 7.4-meters from the cryostat floor, as measured by the "level meter." Physically, it must be that the LAr and GAr remain in thermodynamic equilibrium as the LAr boils off into the ullage, which is why the surface is modeled at saturation conditions. However, because of the unsteady nature of the turbulent LAr flow and inevitable variations in operating conditions, the LAr height must also change over time. It is unclear over what timescale and to what extent this level varies, although it has been reported to vary between 7.2 and 7.5m. Also, the accuracy of the experimental "level meter" is somewhat disputed, and any LAr waves or ripples at the liquid-gas interface are not well understood.

With these uncertainties of reported LAr height in mind, two forward modeled cases were modeled: LAr height of 7.25m and 7.16m, to investigate whether LAr surface height may significantly influence temperature modeling.

3.2.2 Cold Electronics Heat Source

The cold electronics (CE) on the top of either APA dissipate some unknown amount of heat by ohmic dissipation. As previously mentioned, DUNE researchers have estimated the heat transfer from either CE assembly as 336W, but the certainty in this value is unknown. It is hypothesized that since the CE's are upstream from and in close proximity to the top Valencia sensors, that a greater heat source value may explain the temperature profile non-linearity near the LAr surface.

To explore the effect of the CE heat source value, four cases of varying cold electronics heat were modeled as multiples of the base simulation heat:

- No CE heat, 0*336W = 0W
- Half CE heat, 0.5*336W = 168W
- Medium CE heat, 1.5*336W = 504W
- High CE heat, 2.0*336W = 672W

3.2.3 Field Cage Volumetric Heat Source

Similarly to the cold electronics, the Field Cage (FC) may also dissipate heat since it is constantly receiving electrical power input during normal operation. The FC heat has not been previously modeled in CFD, but it is assumed that since the FC panels are large, numerous, and distributed throughout the cryostat, any heat from the components may have a significant impact on the fluid temperature results. Three cases of varying FC volumetric heat were modeled: 32 W/m^3, 320 W/m^3, and 800 W/m^3. This was implemented for each of the four FC regions by specifying a non-zero "energy source" of type "constant volumetric heat source."

3.2.4 Cable Tray and I-Beam Geometries

Oriented parallel to and located above the cold electronics (on both +z and -z APA) are cable trays which route electrical wires to various sensors, cameras, and other features throughout the cryostat (Figure 20). The geometry of these two cable trays were previously neglected in the CFD model, but it is hypothesized that their presence will greatly influence the fluid flow profiles, and thus the fluid temperature profiles. There are

also previously neglected I-beams located at the LAr interface (i.e., the interface intersects the I-beams lengthwise).

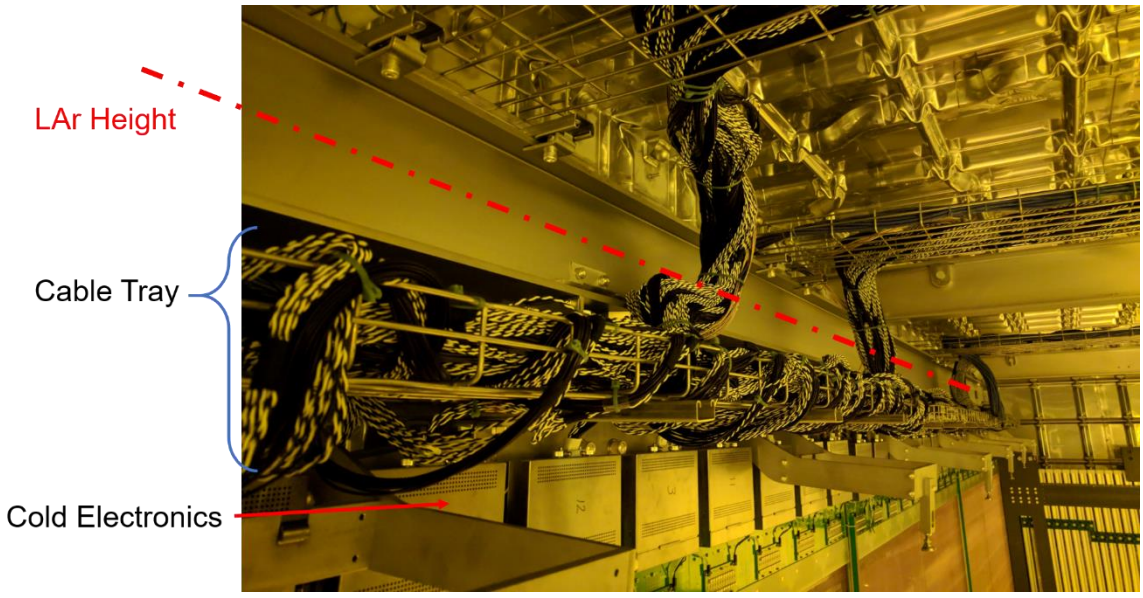

Figure 20. Photo of cable trays and cold electronics (CE) above APA.

A series of simulations were completed to investigate the effect of these flow obstructions: I-Beams and Cable Trays; I-Beams and no Cable Trays; I-Beams and larger Cable Trays. The Cable Tray and I-Beam parameterizations were applied to the LAr model by adding impermeable, smooth walls which approximate the exterior bounds of the flow obstruction—essentially creating a negative space where the fluid may not flow. Figure 21 illustrates the relative size and location of the cable trays (in yellow) and I-beam geometries, where (a) shows the original cable tray size and (b) is the "larger" cable tray case.

3.2.5 Combined Effects

After the original set of parametrizations were modeled, the combined effects of LAr height and cable tray/ I-beam geometries, and LAr height and FC heat were studied. It was hypothesized that the superposition of favorable simulation improvements could improve agreement even further.

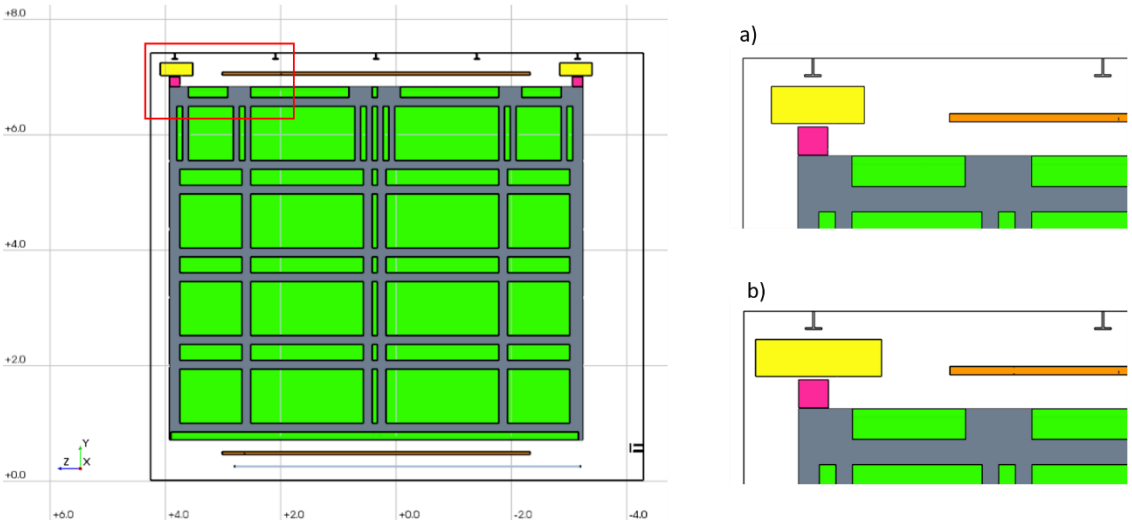

Figure 21. Location of modeled cable trays and I-beams (left). Cable tray sizes (a) original and (b) larger modeled separately.

3.3 Inverse Modeling

Analysis of each CFD model parameterization is based on the comparison of the calculated temperature profiles with the experimental temperature data. As was done by Pedersen (2019), the raw CFD temperature data was first corrected slightly to allow direct comparison to the experimental temperature data. Since the experimental probes are not calibrated absolutely, it is valid to look at only the relative temperature values and the shape of the temperature profiles. The profile correction involves translating the CFD temperature results (or rather adjusting the CFD data temperature scale) by an amount equal to the difference in mean experimental temperature and mean CFD temperature for

a given profile—effectively equating the mean CFD and experimental temperatures for each the Static and Dynamic temperature profiles. Figure 22 illustrates this correction process for the Valencia (static) profile in the base CFD simulation: by translating the Valencia temperatures by 49mK, the profile average temperature for experimental and CFD are made equal, and a direct comparison of the relative profile shapes is possible. Also at this step, the corrected CFD profile is filtered to include only temperatures at the same discrete heights defined by the experimental profiles. Since the fluid temperature is not known between experimental datum, it is not reasonable to assume (by interpolation or otherwise) the true temperatures at these locations. Therefore, the CFD error is taken by comparison to experimental only at those reported profile heights.

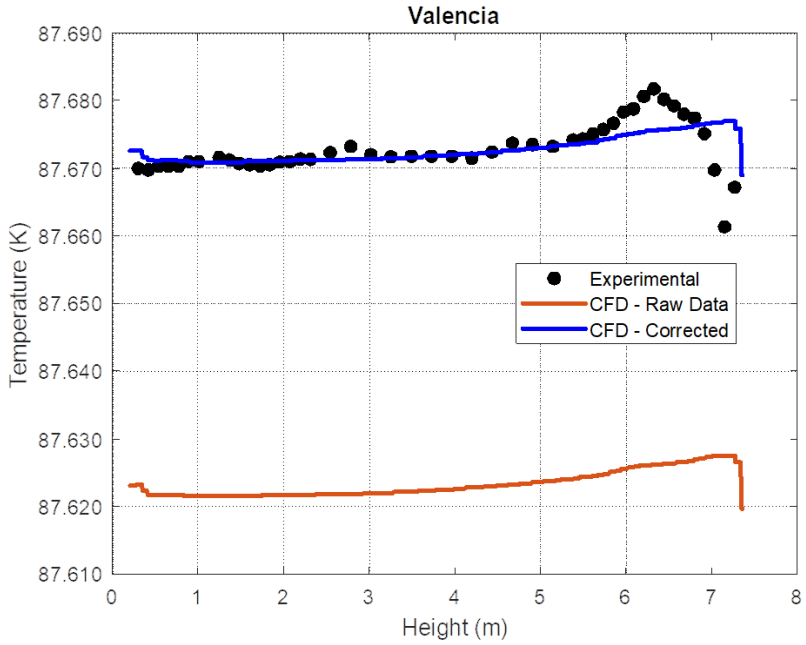

Figure 22. CFD Valencia temperature profile correction.

The error of the calculated (CFD) temperature data, then, is considered by calculating the mean square error (MSE) of each profile. The MSE estimates the error of a CFD temperature against a "true" experimental temperature by taking the square of the

difference, repeating that calculation for the temperatures at each profile height, and averaging the squared difference over the full profile height. The MSE, then, gives a singular quantifier of CFD and experimental temperature agreement. Additionally, as opposed to the sum of square errors metric, the MSE allows for direct comparison between Valencia and Hawaii errors, since the values are normalized to the number of profile sensors. If the sum of squared errors was used instead, the Valencia error would appear disproportionately large since it has twice as many data points (sensors) as Hawaii.

In addition to the full-profile MSE, since the main motivation for this work is associated with the cause of the highly non-linear temperature distribution of the static (Valencia) profile, and since the most error is observed very near the LAr surface, a second error quantifier was defined for the profile heights less than 7-meters. The MSE calculation was essentially repeated for only those profile temperatures in the region from the cryostat floor (zero meters) to a height of 7-meters, thus neglecting the disproportionately large error near the LAr-GAr interface.

Quantitative measures are useful in assessing the effects of a given CFD parameterization, but qualitative comparisons were also needed to better understand the flow field. The LAr flow patterns, for example, are an important consideration in analyzing each simulation case. Velocity streamlines throughout the fluid volume were generated by propagating “point seeds” from the LAr inlets and plotting their resultant path throughout the cryostat. The streamline figures were exported and compared between CFD parameterized cases to observe changes in flow patterns due to model changes. Velocity vector scenes in-plane with the Valencia profile were also used.

The original parameterizations were modeled and simulated as previously described. A combination of these quantitative (MSE) and qualitative (temperature plots, streamline figures) methods were used to (1) identify model changes which significantly altered (or improved) temperature results and (2) identify by what mechanism or factor initiated that different result.

Using this, subsequent parameterizations were selected (or eliminated) based on whether that model or feature alteration/addition may influence the model by a similar mechanism. For example, by assessing those parameterizations which improved the temperature modeling, if the temperature improvement appeared to be caused by a change in fluid flow patterns, potential model changes would likewise be weighed against whether they may similarly influence the flow patterns and paths. Alternatively, if an increase in a heat source appears to be improving the temperature results, further increases in heat were considered based on whether they were still physically possible and were implemented until an optimum heat value was identified.

It is worth noting, again, that inverse problems do not result in unique solutions. Instead, the goal of this work is to identify potential causes and assess the relative importance of different model features with respect to temperature modeling.

4 RESULTS AND DISCUSSION

The goals of this work were centered around recreating the local, experimental temperature profiles of the ProtoDUNE-SP LAr with computational fluid dynamics. Through a parametric series of "forward modeled cases" and comparisons to available experimental data, inverse reasoning was employed to speculate on which discrete geometries and heat sources may be significant to include in CFD representations of the LAr. Identifying and quantifying detector/ cryostat features which are impactful (from a fluid mechanics and heat transfer perspective) can help in optimizing CFD procedures, improving temperature prediction (modeling), and possibly interpreting experimental measurements in the future.

4.1 Base CFD Simulation

The base CFD simulation includes updates to detector operating conditions and iteration-averaged temperature reporting and serves as a baseline for all parameterized modeling cases. The static Valencia and dynamic Hawaii temperature profiles are compared to the experimental in Figure 23 where the CFD Valencia profile was corrected by 49.4mK and Hawaii by 57.7mK. The mean square error (MSE), and maximum profile error for both profiles are listed in Table 11.

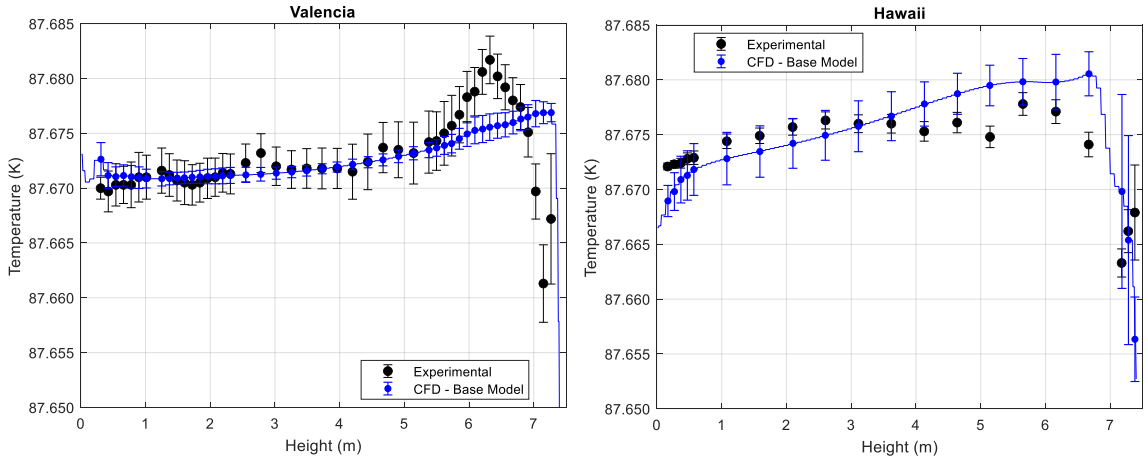

Figure 23. CFD base case, temperature profiles Valencia (left) and Hawaii (right) compared to experimental.

Table 11. CFD base case, temperature profile mean squared errors and maximum deviation.

	MSE*10^6	Bottom (<7m) MSE*10^6	Max Deviation (mK)
Valencia	11.8	3.7	15.58
Hawaii	14.8	7.0	11.56

As was the case in the preexisting ProtoDUNE-SP LAr model, the base CFD model did not capture the desired non-linear temperature “bump” in the 6.3m region of Valencia. However, for all heights below 6m, the Valencia profile is in agreement with the experimental. The calculated Hawaii profile likewise captures the general trend in the temperature distribution but fails to recreate the slight decrease and then increase in the range of 4.5 to 6m. The full mean squared error (MSE) and the “bottom” MSE were both slightly better for the Valencia profile than the Hawaii with an MSE*10^6 of 11.8 for the full profile and a MSE*10^6 of 3.7 for heights less than 7 meters (“bottom” MSE).

4.2 Initial Model Parameterizations

The original changes to the base CFD model for the first round of forward modeling included parametric changes to: the LAr-ullage interface height; the cold electronics (CE) heat source magnitude; the field cage (FC) volumetric heat source magnitude; the existence of cable tray and I-beam geometries. For each case, a separate STAR-CCM+ CFD simulation was set up and calculated using the previously described forward modeling methods, and the pertinent temperature results were exported for subsequent comparisons and inverse modeling.

4.2.1 Effect of LAr-Ullage Interface Height

The location of the LAr-GAr interface was varied from the base model 7.40m height in two cases: 7.25m and 7.16m height. The resulting temperature profiles are shown in Figure 24 and Figure 25 and the profile errors are given in Table 12.

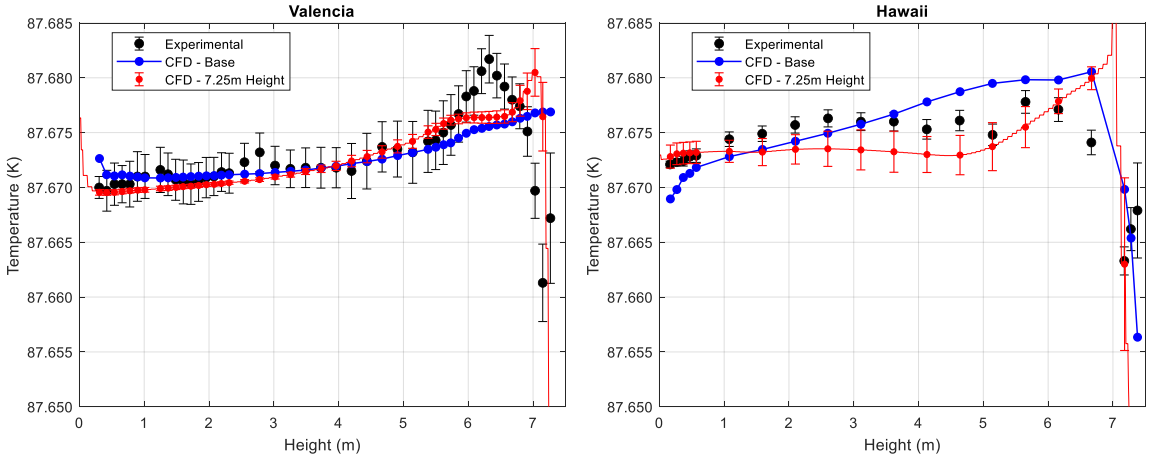

Figure 24. CFD case LAr height = 7.25m, temperature profiles Valencia (left) and Hawaii (right).

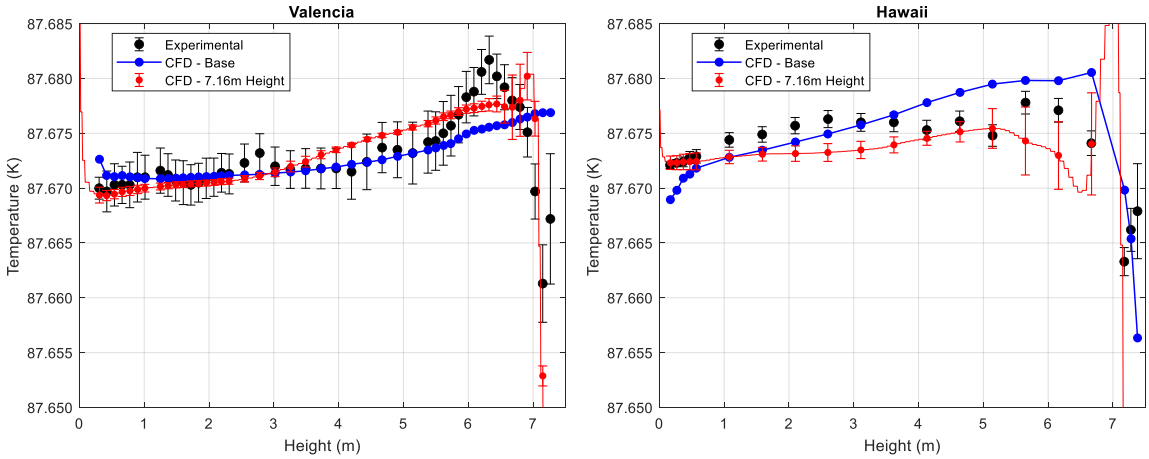

Figure 25. CFD case LAr height = 7.16m, temperature profiles Valencia (left) and Hawaii (right).

Table 12. CFD varying LAr heights, temperature profiles mean squared errors and maximum deviation.

LAr Height (m)	*Valencia*			*Hawaii*		
	MSE*10^6	Bottom (<7m) MSE*10^6	Max Deviation (mK)	MSE*10^6	Bottom (<7m) MSE*10^6	Max Deviation (mK)
7.40 (Base Case)	11.8	3.7	15.58	14.8	7.0	4.12
7.25	10.4	2.8	15.15	5.0	5.2	5.86
7.16	5.1	2.7	8.43	3.7	3.7	11.56

Lowering the LAr interface height positively impacted both the Valencia and Hawaii temperature profiles. In the case of Valencia, both shortened height cases resulted in a steeper gradient of temperature versus height towards the top of the cryostat, approaching the experimental behavior in that region. Both height cases also demonstrated a sharp temperature peak in the Valencia profile of the same magnitude as the experimental "bump," but at a higher height of about 7m. This resulted in a much-improved Valencia MSE*10^6 of 10.4 for the 7.25m case, and 5.1 for the 7.16m case.

The CFD Hawaii profile also demonstrated decreasing error with decreasing LAr height. The MSE*10^6 for the 7.25m and 7.16m cases were found to be 5.0 and 3.7, respectively. The maximum profile deviation, however, was worse for the 7.16m case with a value of 11.56mK.

Figure 26 shows the propagation of velocity streamlines originating at the LAr inlets and traveling throughout the cryostat. The contours superimposed on the velocity streamlines and the contour planes represent the fluid temperature distributions. It is worth noting that the temperatures shown here are not iteration-averaged as was reported for the quantitative analyses. Rather, the temperatures and velocity paths in Figure 26 are of the instantaneous calculated solution at 100,000 iterations. It would be computationally prohibitive to calculate the iteration-averaged temperatures and iteration-averaged velocities at all locations in the cryostat. Also, since they are just used for qualitative observation and comparison, and not quantitative error calculations, unsteady effects are not as important.

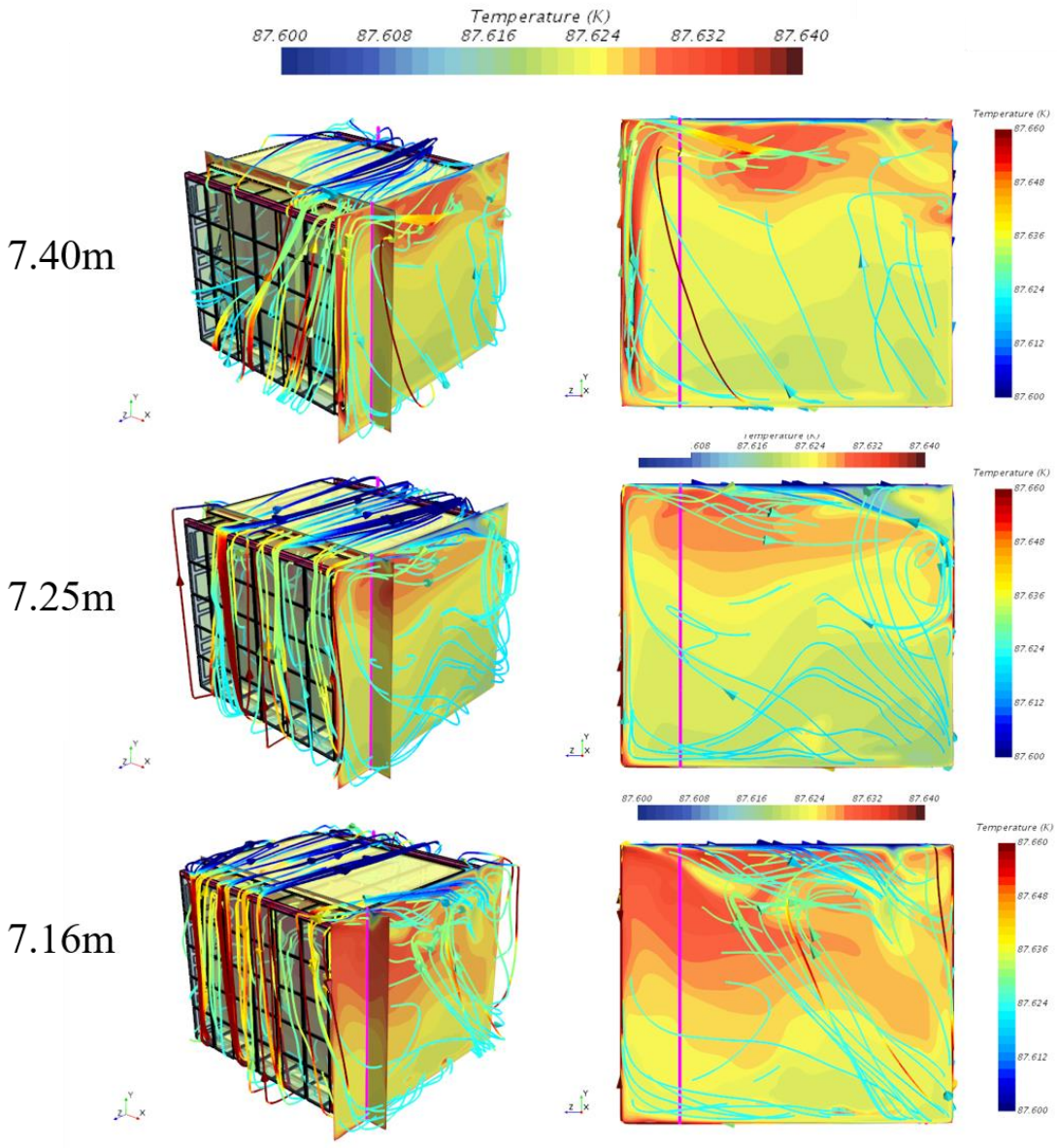

Figure 26. CFD varying LAr-ullage interface height, velocity streamlines with temperature contours, isometric (left) and +x normal (right).

The shortened LAr height cases of 7.25m and 7.16m heights resulted in better Valencia profile agreement. By inspection of the left column of Figure 26, it is interesting to note that the streamlines of the favorable cases travel nearly straight upward along the +z side, instead of drifting in the +x direction as is the case in the less favorable case of

7.4m. In all cases, the warm fluid from the inlets travels upward (+y) until it encounters the cool LAr interface where the fluid is redirected by the boundary and is cooled. In the base 7.4m case, the 4 warm inlet plumes seem to converge and encounter the LAr interface in the upper +x+z corner and are redirected in the -x-z direction as the now-cooled fluid sinks due to buoyant forces. In the shortened height cases, the inlet plumes do not experience as significant movement in the x direction, but remain uniformly distributed as they are redirected by the interface in the -z direction (no significant x component). This allows for some of the cooled fluid to descend on the +x side of the TPC (the same region as the Valencia profile). The effect of the sinking fluid on the -z side of this zone is a local warm "pocket" of LAr near the ullage interface.

Each LAr-ullage interface height case demonstrated a similar "warm" zone of LAr near the surface, as shown in Figure 27 through Figure 29 where the relative temperature contours are based on a datum at a 1m height on the Valencia profile. Interestingly, it appears that by shortening the LAr surface height, the zone moves closer to the Valencia profile.

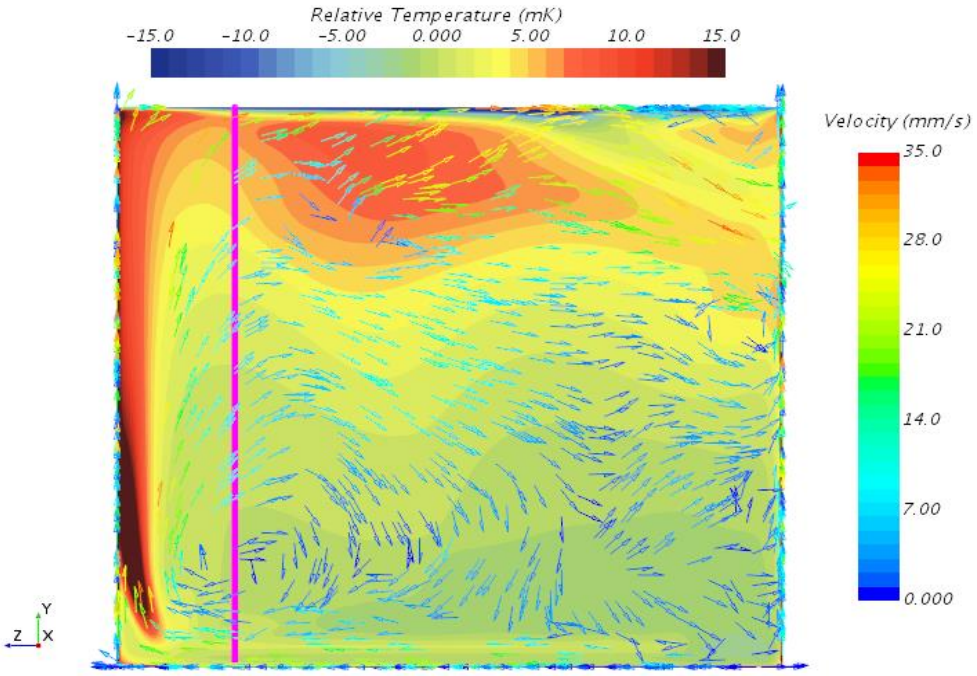

Figure 27. Varying LAr-ullage interface height 7.40m (base) case, relative temperature contour with velocity vector (projection) in-plane with Valencia.

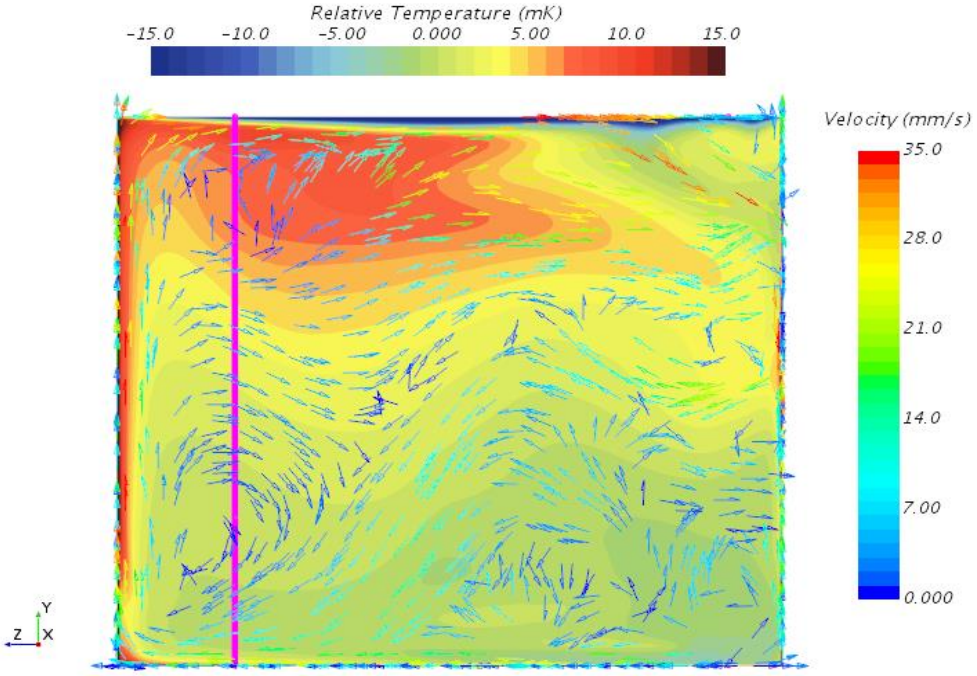

Figure 28. Varying LAr-ullage interface height 7.25m case, relative temperature contour with velocity vector (projection) in-plane with Valencia.

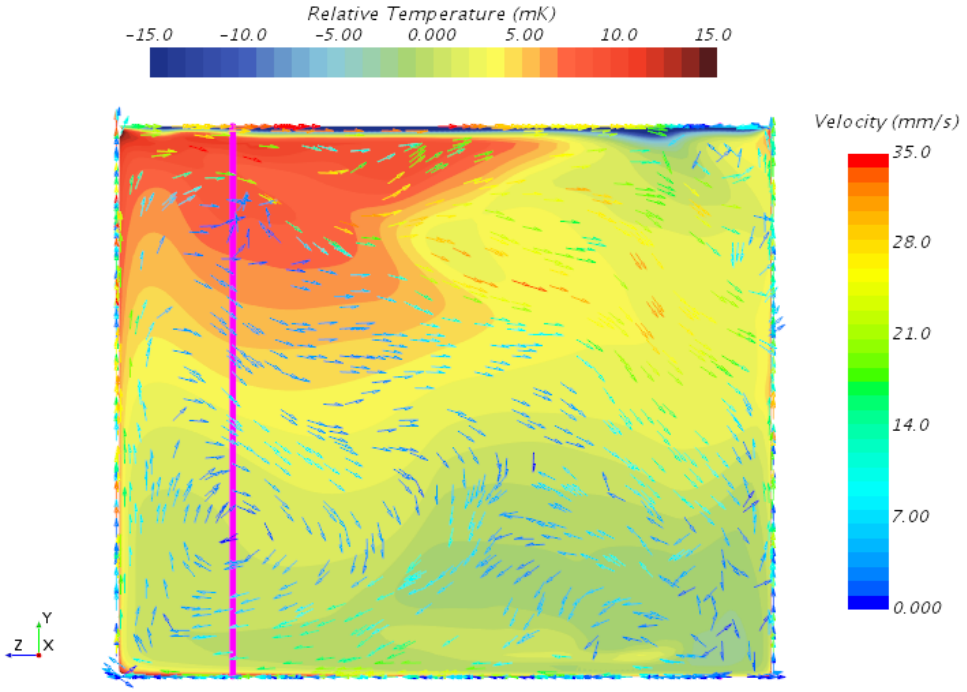

Figure 29. Varying LAr-ullage interface height 7.16m case, relative temperature contour with velocity vector (projection) in-plane with Valencia.

4.2.2 Effect of Cold Electronics Heat Source

The heat (power) source value applied to each of the two cold electronics (CE) regions was varied from the base 336W. In multiples of the base value, four cases were simulated to study the effect of the heat source on the simulated temperature. Figure 31 through Figure 33 illustrate the calculated Valencia and Hawaii temperature profiles for each case. Table 13 summarizes the error metrics for these cases.

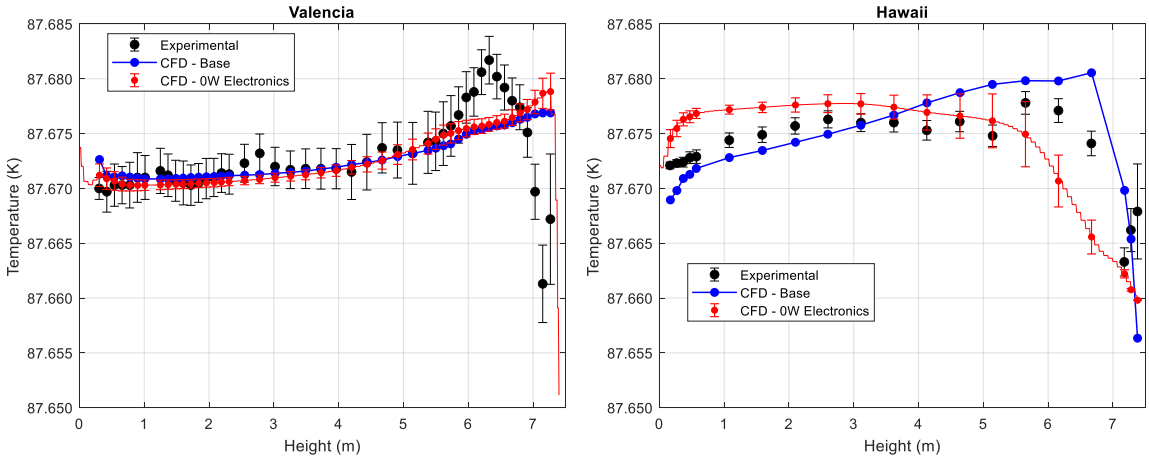

Figure 31. CFD case No CE Heat (0W), temperature profiles Valencia (left) and Hawaii (right).

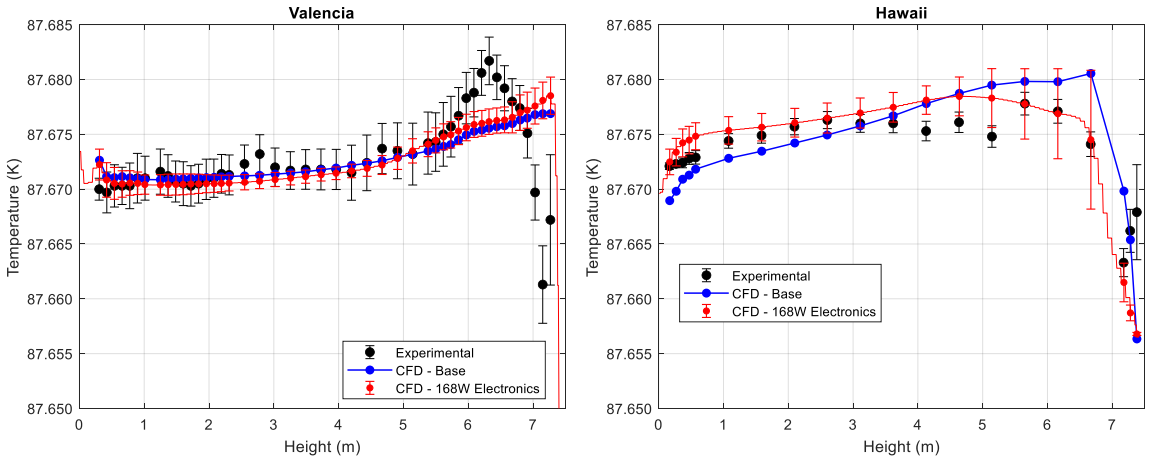

Figure 30. CFD case 0.5*CE Heat (168W), temperature profiles Valencia (left) and Hawaii (right).

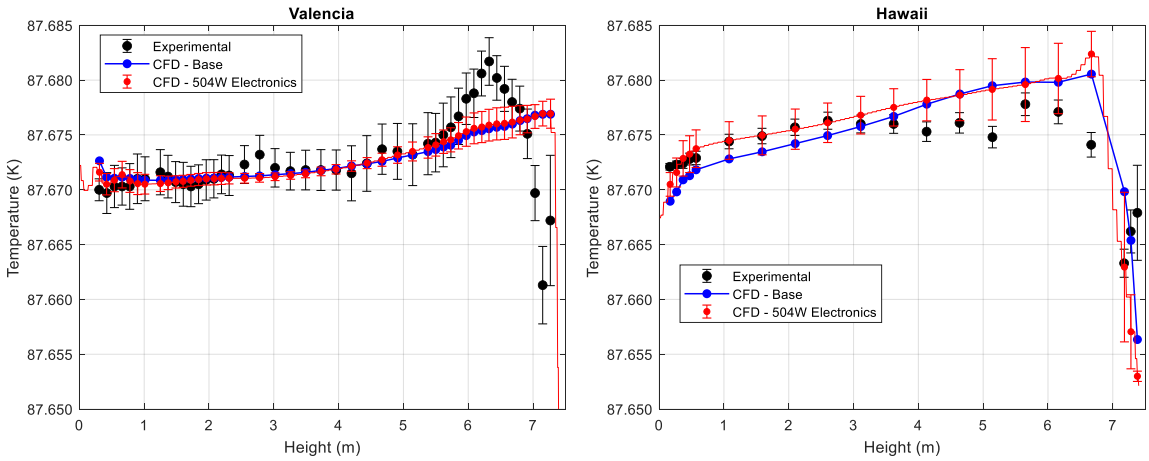

Figure 32. CFD case 1.5*CE Heat (504W), temperature profiles Valencia (left) and Hawaii (right).

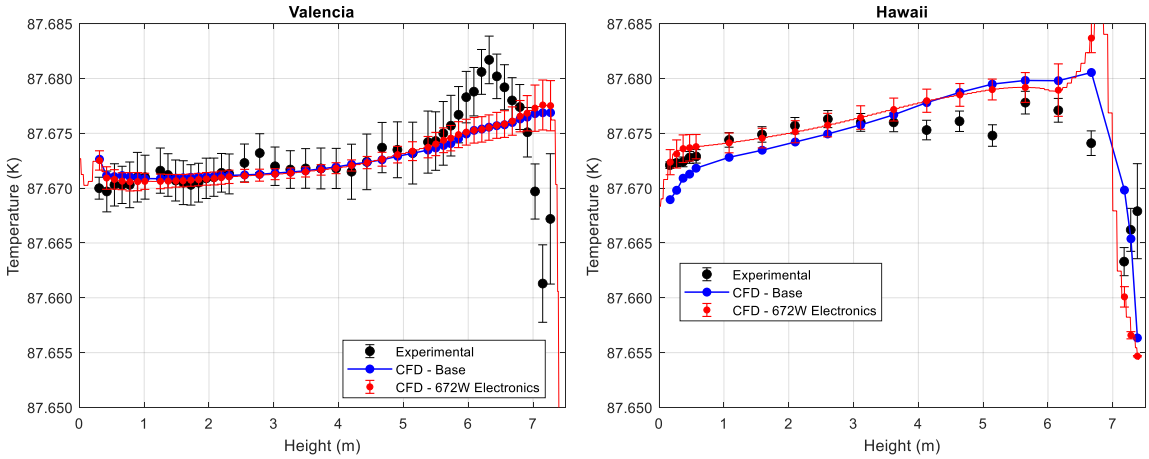

Figure 33. CFD case 2.0*CE Heat (672W), temperature profiles Valencia (left) and Hawaii (right).

Table 13. CFD varying CE heat, temperature profiles mean squared errors and maximum deviation.

CE Heat (W)	*Valencia*			*Hawaii*		
	MSE*10^6	Bottom (<7m) MSE*10^6	Max Deviation (mK)	MSE*10^6	Bottom (<7m) MSE*10^6	Max Deviation (mK)
0	13.9	3.1	17.38	15.4	12.5	8.53
168	13.0	2.9	16.79	11.2	2.5	11.10
336 (Base case)	11.8	3.7	15.58	14.8	7.0	11.56
504	11.3	3.1	15.65	21.4	7.2	14.91
672	12.6	3.5	16.28	20.6	7.9	13.23

The simulated and experimental Valencia profiles agree well for all CE heat cases. Lowering the CE heat input from 336W to half (168W) or zero created a slight concave-up temperature distribution in the upper (>5m) Valencia region—opposite of the desired behavior. The best CE heat source in terms of Valencia profile agreement was found to be 504W (1.5*base) with an improved MSE*10^6 of 11.3 and bottom MSE*10^6 of 3.1. The maximum deviation for Valencia did not improve drastically in the 504W case over the base case.

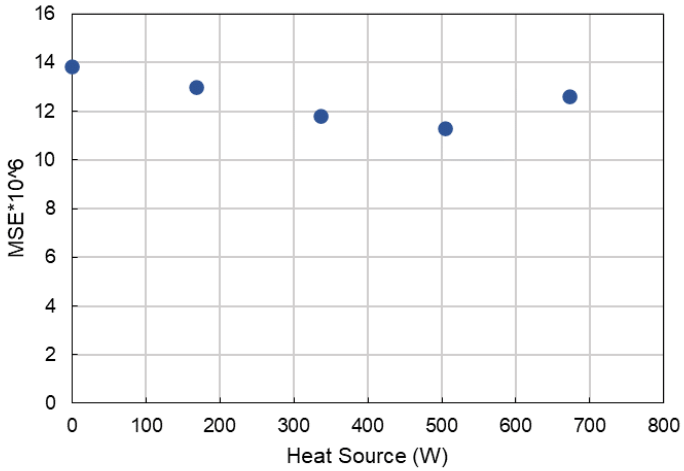

Figure 34. CFD Valencia MSE*10^6 with varying CE Heat.

Reducing the CE heat source impacted the Hawaii profile by flattening the temperature distribution in the lower height range (0 to 5m) and making it a more gradual decrease in the upper height range, which deviates from the experimentally observed behavior. Increasing the CE heat did not significantly impact the lower height range of Hawaii but did add some non-linearity in the upper range. Whereas the experimental predicts a slight increase (3mK) at height of 5.5m, the increased CE heat cases predicted a local maximum at a height of 6.6m (2mK for 504W and a more dramatic 48mK for 672W).

It is known that the reported quantity for heat dissipated by the cold electronics (CE) assemblies is simply an estimate, but the uncertainty in the reported value is not known. Since there is a local minimum in Valencia MSE at CE heat of 504W, it is possible that the reported CE heat input is an underestimate, and that the actual (higher) heat value contributes to the Valencia "bump." Although this CE heat value does not necessarily improve the Hawaii profile agreement, it does not significantly hurt it either. The relative shape of the Hawaii profile is virtually unchanged in the lower (0-6m) height region.

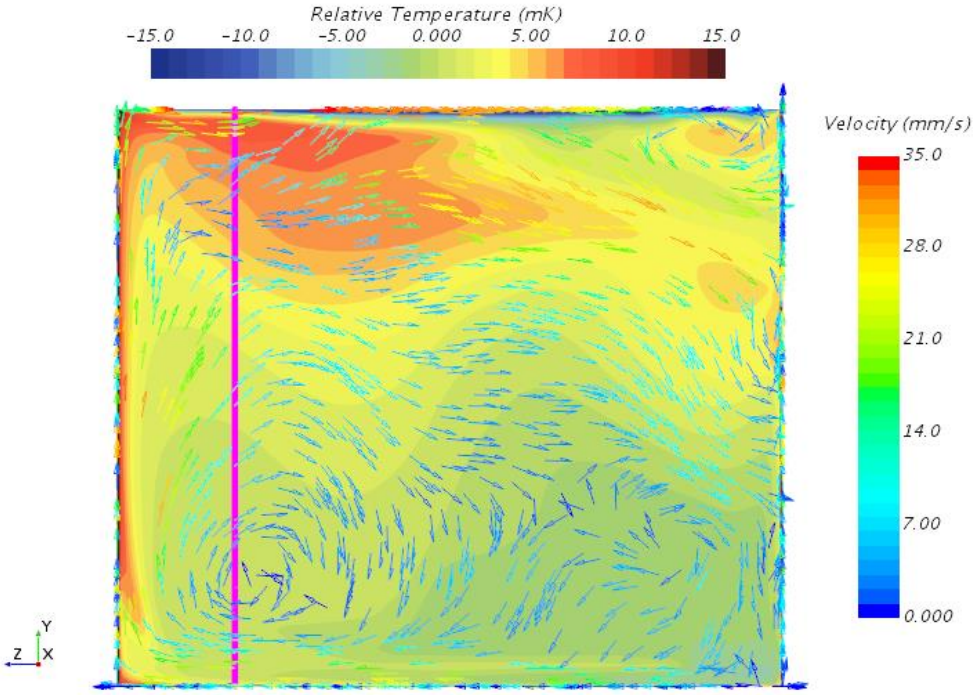

Figure 35. Varying CE Heat Source 0W case, relative temperature contour with velocity vector (projection) in-plane with Valencia.

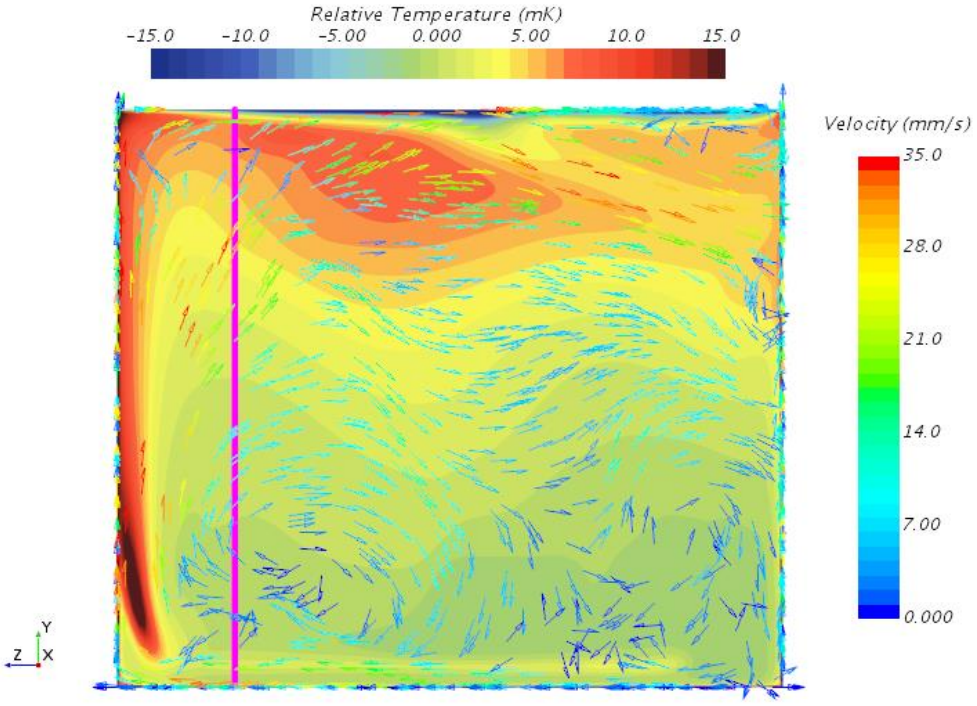

Figure 36. Varying CE Heat Source 168W case, relative temperature contour with velocity vector (projection) in-plane with Valencia.

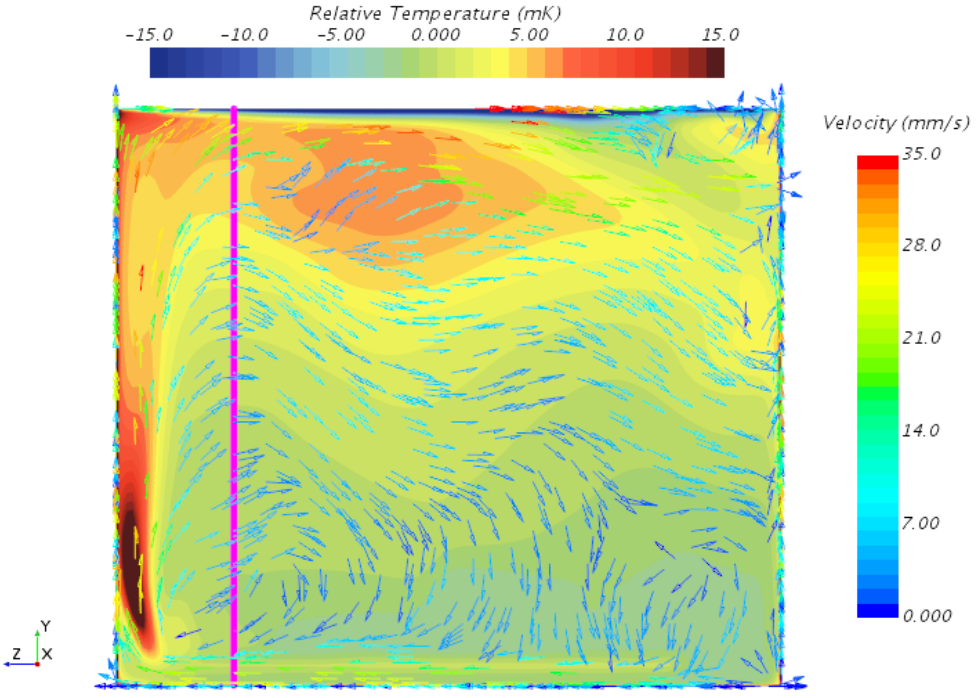

Figure 37. Varying CE Heat Source 504W case, relative temperature contour with velocity vector (projection) in-plane with Valencia.

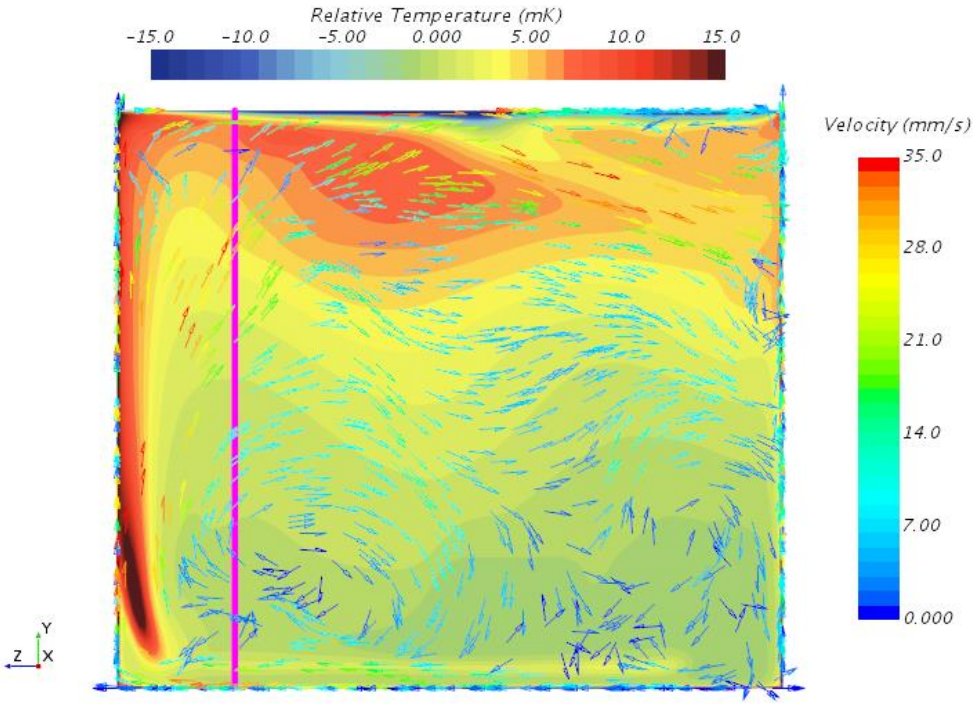

Figure 38. Varying CE Heat Source 672W case, relative temperature contour with velocity vector (projection) in-plane with Valencia.

4.2.3 Effect of Field Cage Volumetric Heat Source

Volumetric heat source magnitudes varying from 0 (base case) to 800W/m^3 were considered for the field cage (FC) regions, and their effects on fluid temperatures were compared. Figures 39, 40 and 41 illustrate the temperature distribution results from the three FC heat cases.

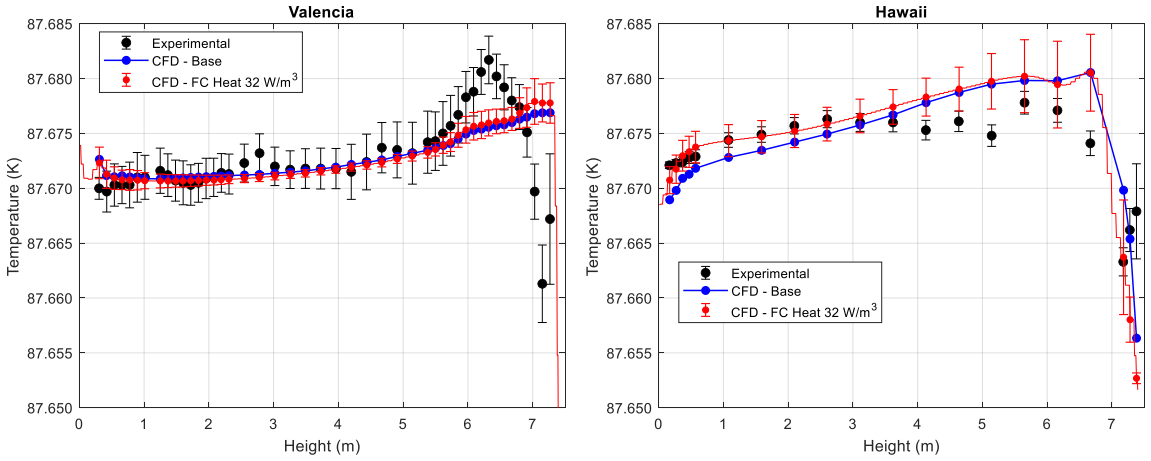

Figure 40. CFD case FC Heat 32W/m^3, temperature profiles Valencia (left) and Hawaii (right).

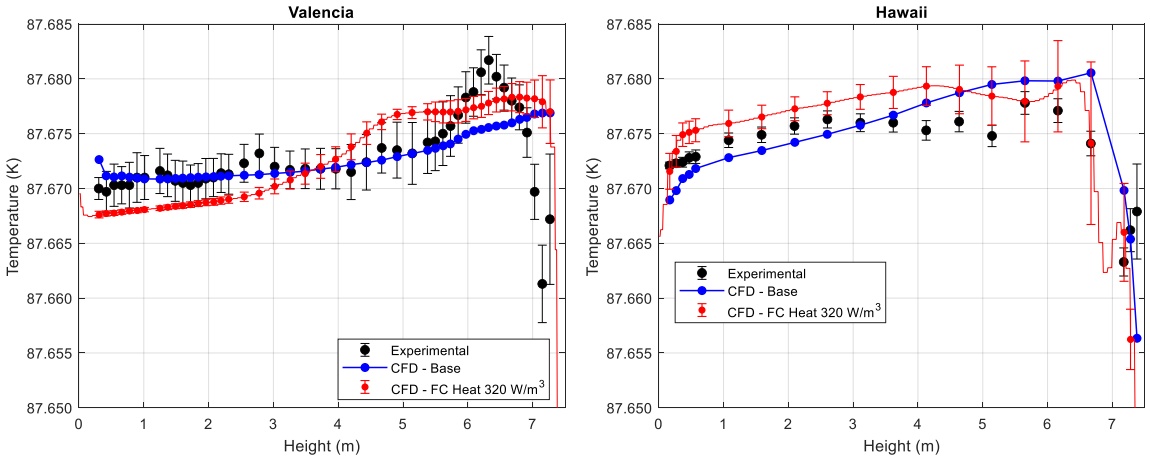

Figure 39. CFD case FC Heat 320W/m^3, temperature profiles Valencia (left) and Hawaii (right).

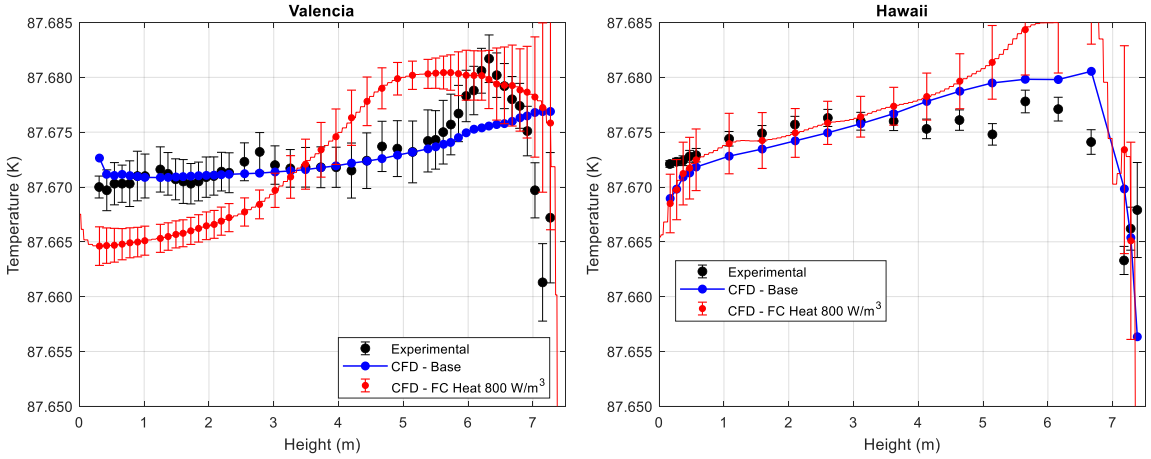

Figure 41. CFD case FC Heat 800W/m^3, temperature profiles Valencia (left) and Hawaii (right).

Table 14. CFD varying FC heat, temperature profiles mean squared errors and maximum deviation.

FC Heat (W/m^3)	*Valencia*			*Hawaii*		
	$MSE*10^6$	Bottom (<7m) $MSE*10^6$	Max Deviation (mK)	$MSE*10^6$	Bottom (<7m) $MSE*10^6$	Max Deviation (mK)
0 (Base case)	11.8	3.7	15.58	14.8	36.0	7.0
32	12.8	3.2	16.48	20.0	53.7	6.0
320	14.8	5.5	16.61	40.5	106.1	5.0
800	27.1	19.7	15.95	100.0	278.9	20.3

The addition of volumetric FC heat had a positive impact on the lower height regions (<7m) of both Valencia and Hawaii. The “bottom” MSE*10^6 for Valencia improved from 3.7 in the base case to 3.2 in the 32 W/m^3 FC heat case, and for Hawaii improved from 7.0 in the base case to 6.0 and 5.0 in the 32 W/m^3 and 320 W/m^3 FC heat cases, respectively. Although increasing the FC heat above 320 W/m^3 added desired nonlinearity to the Valencia profile, the nonlinear effect was too drastic, and the Hawaii profile showed significant disagreement with experimental.

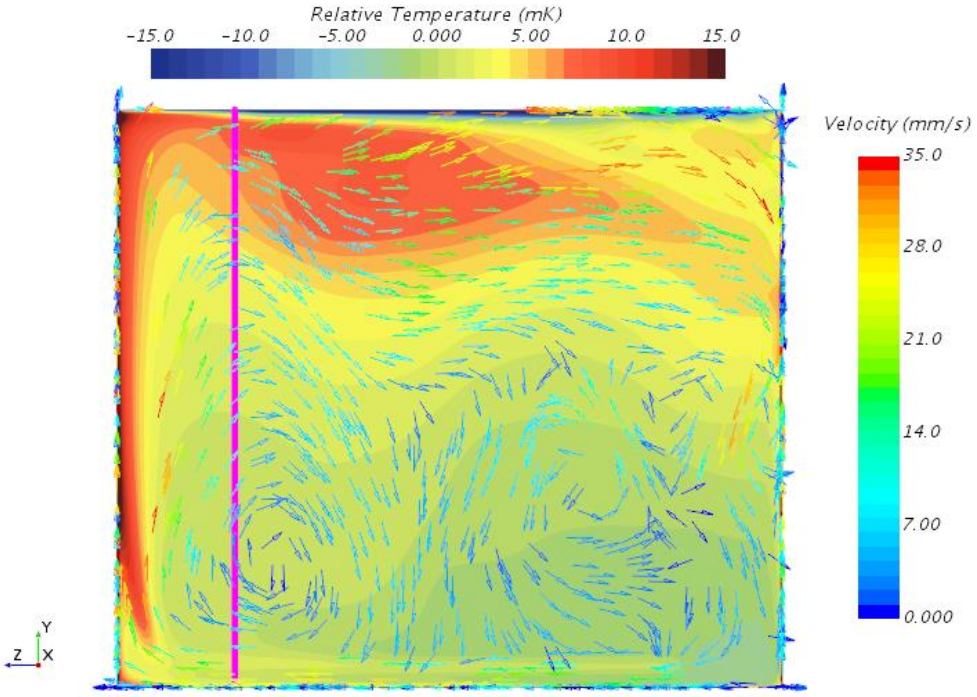

Figure 42. Varying FC Heat Source 32W/m^3 case, relative temperature contour with velocity vector (projection) in-plane with Valencia.

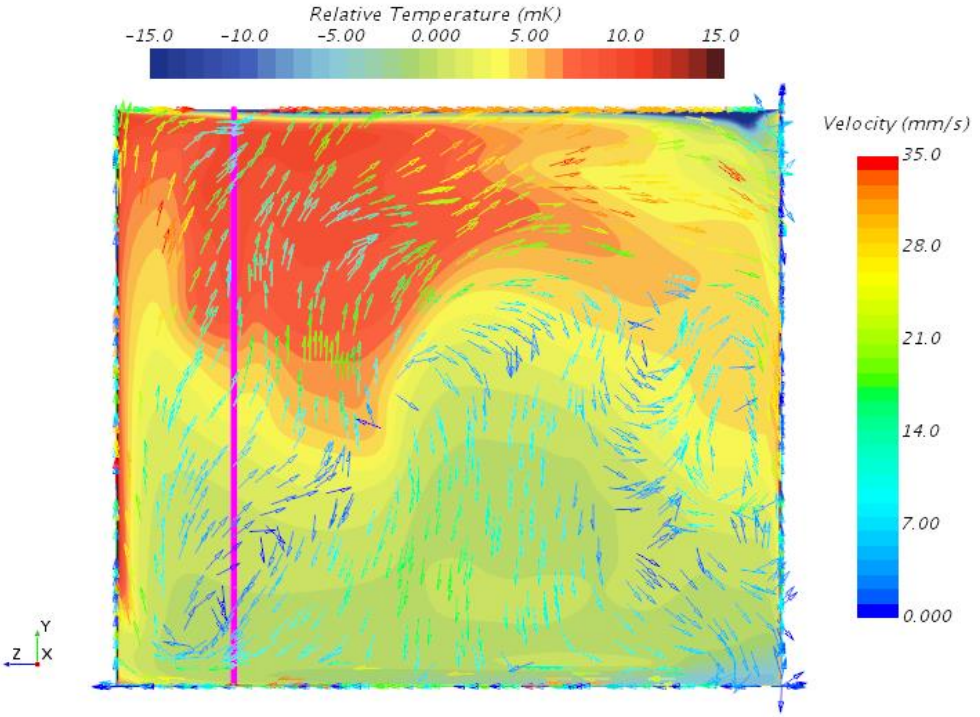

Figure 43. Varying FC Heat Source 320W/m^3 case, relative temperature contour with velocity vector (projection) in-plane with Valencia.

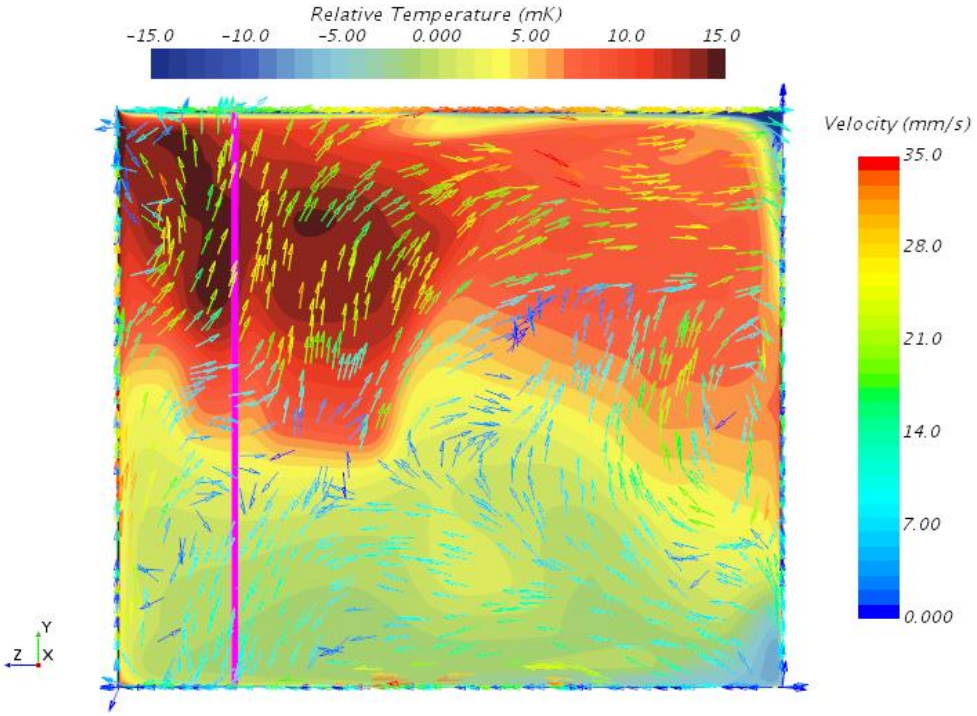

Figure 44. Varying FC Heat Source 800W/m^3 case, relative temperature contour with velocity vector (projection) in-plane with Valencia.

4.2.4 Effect of Cable Tray and I-Beam Geometries

Physical geometries (flow obstructions) which were identified as potentially significant to the thermal modeling, namely the cable trays and I-beams, were parametrically added to the base CFD model. Figure 47 illustrates the case of I-beams and no cable trays; Figure 46 shows the case of I-beams with cable trays. Figure 45 and 48 are variations of the I-beams and cable tray case with larger cable trays and extended +z side I-beam, respectively.

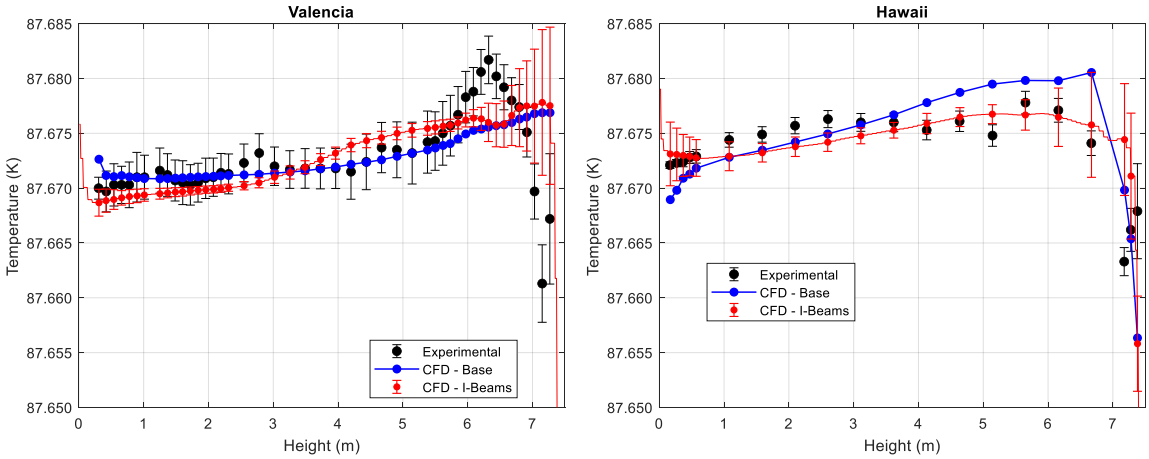

Figure 47. CFD case I-Beams, temperature profiles Valencia (left) and Hawaii (right).

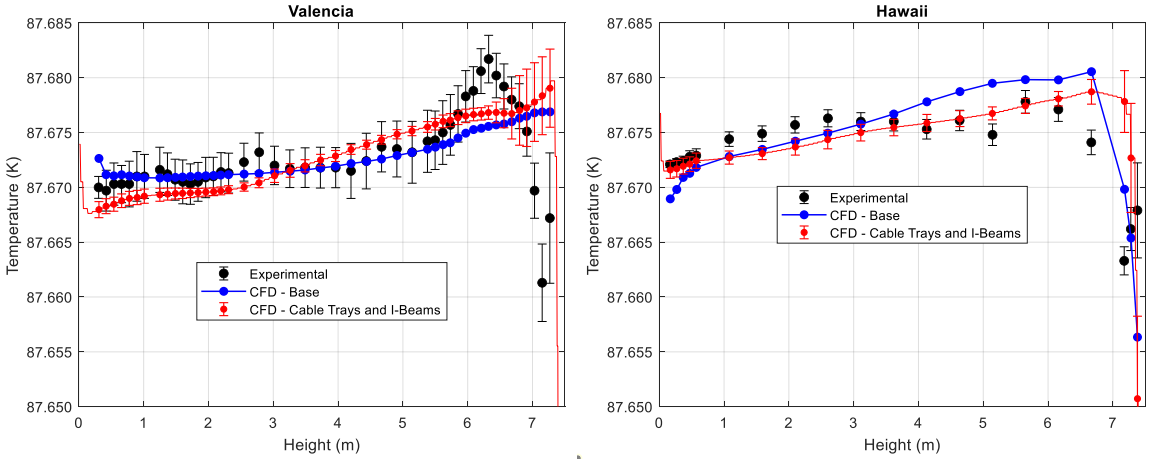

Figure 46. CFD case I-Beams and Cable Trays, temperature profiles Valencia (left) and Hawaii (right).

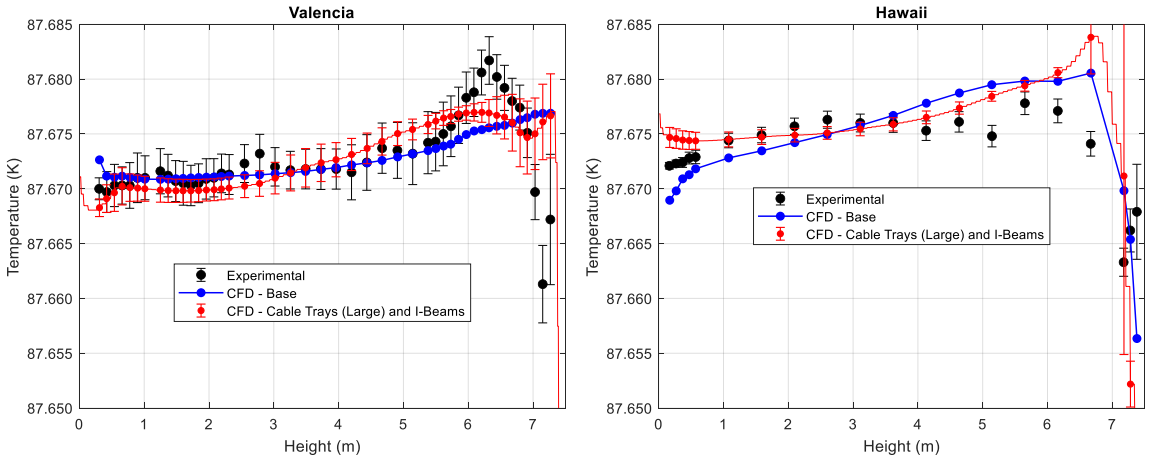

Figure 45. CFD case I-Beams and Cable Trays (larger), temperature profiles Valencia (left) and Hawaii (right).

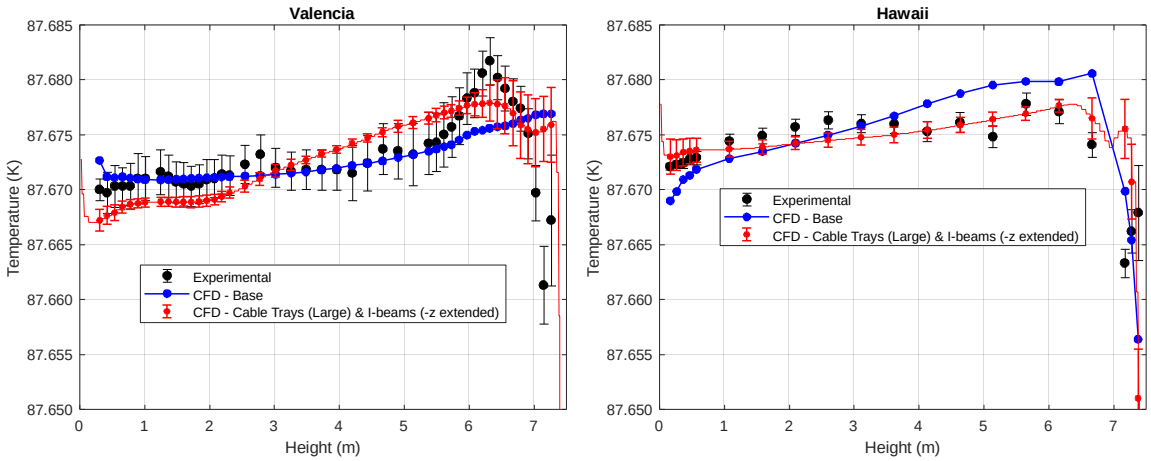

Figure 48. CFD case I-Beams (+z beam longer) and Cable Trays (larger), temperature profiles Valencia (left) and Hawaii (right).

Table 15. CFD varying I-Beam and Cable Tray geometries, temperature profiles mean squared errors and maximum deviation.

	Valencia			*Hawaii*		
	MSE*10^6	Bottom (<7m) MSE*10^6	Max Deviation (mK)	MSE*10^6	Bottom (<7m) MSE*10^6	Max Deviation (mK)
None (Base Case)	11.8	3.7	15.58	14.8	7.0	11.56
I-Beams	13.1	3.8	16.52	16.0	1.5	12.09
I-Beams & Cable Trays	14.0	3.4	17.06	29.6	2.6	17.18
I-Beams & Larger Cable Trays	10.0	2.9	14.79	44.4	8.7	21.94
I-Beams (+z extend) & Cable Trays	10.4	4.0	14.19	23.9	1.3	16.93

The addition of near-surface geometries such as I-beams and cable trays had an interesting effect on the Valencia temperature profile. Firstly, all parameterizations in this category resulted in greater temperature solution unsteadiness in the Valencia profile near the surface (>6m), as demonstrated by the larger error bars in Figures 45 through 48. This

is likely due to greater recirculation and turbulent effects induced by the added geometries. Further, these cases demonstrated some favorable non-linear temperature behavior in the upper region of the Valencia profile. In particular, the cases of (i) I-beams and larger cable trays and (ii) I-beams and cable trays (with +z beam extended in the -x direction) both produced a concave down Valencia distribution in the region of the experimental "bump," and both improved the Valencia MSE metric 10.0*10^6 in (i) and 10.4*10^6 in (ii).

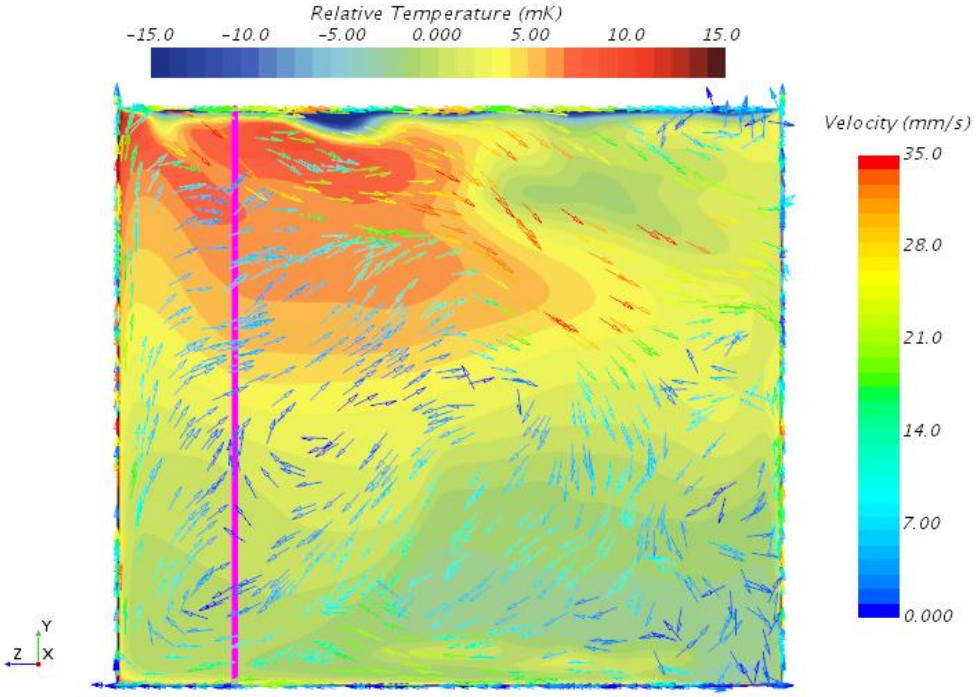

Figure 49. CFD case I-Beams, relative temperature contour with velocity vector (projection) in-plane with Valencia.

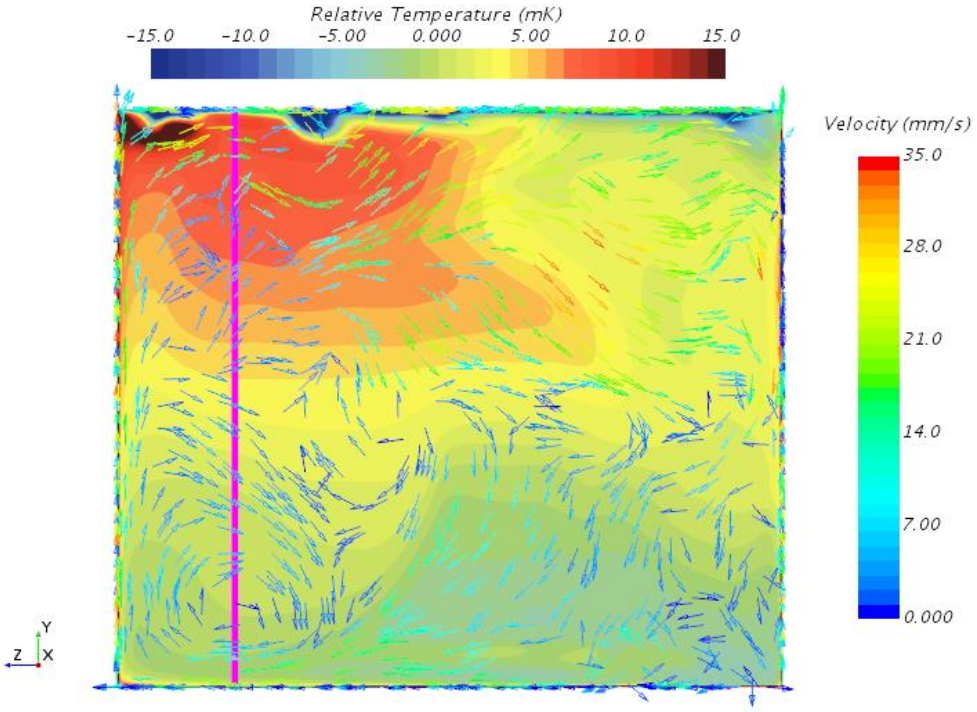

Figure 50. CFD case I-Beams and Cable Trays, relative temperature contour with velocity vector (projection) in-plane with Valencia.

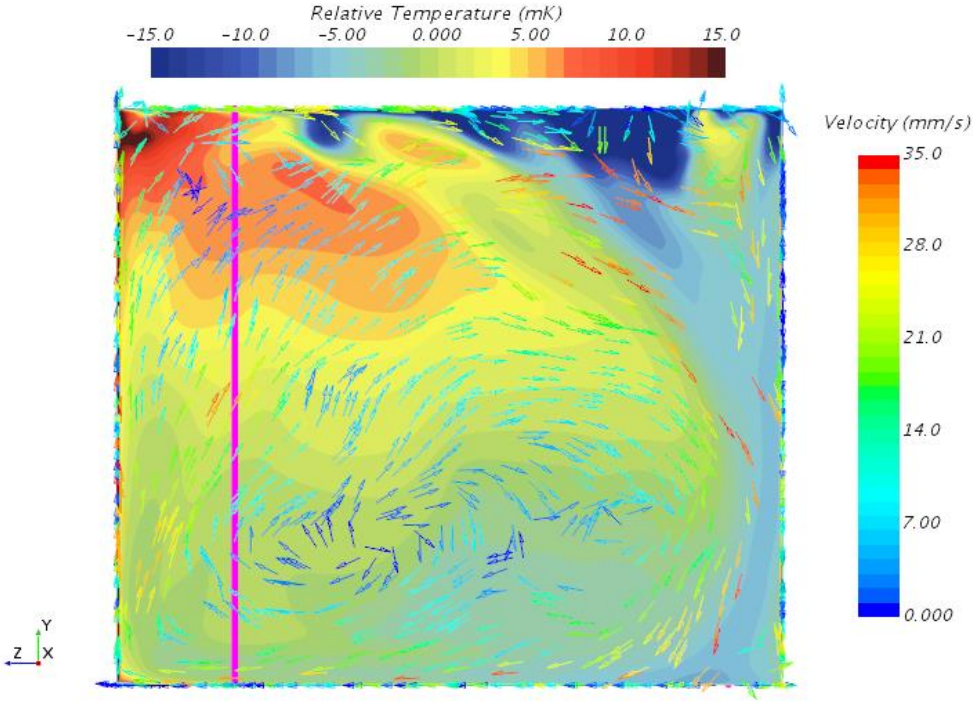

Figure 51. CFD case I-Beams and Cable Trays (larger), relative temperature contour with velocity vector (projection) in-plane with Valencia.

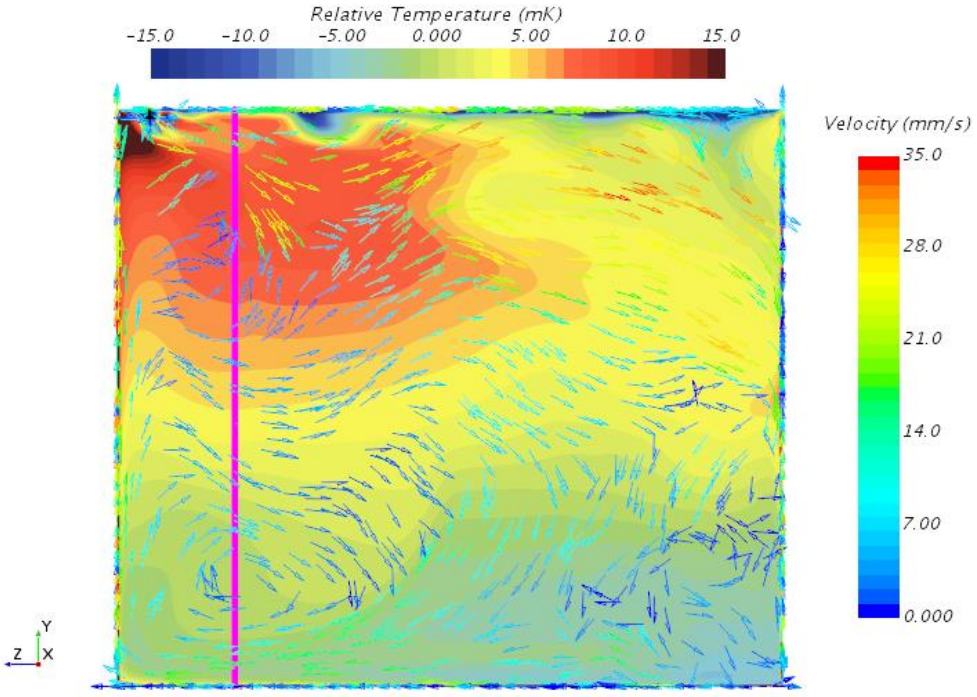

Figure 52. CFD case I-Beams (+z beam longer) and Cable Trays (larger), relative temperature contour with velocity vector (projection) in-plane with Valencia.

4.3 Combined Effects

The combined effects of varying LAr-ullage interface height and the near-surface geometries (I-beams and cable trays) simultaneously were considered since both features demonstrated improvements to the CFD predicted Valencia temperature profile. Figure 53 shows relative temperature contours and velocity vectors in-plane with Valencia (x normal) for LAr surface heights 7.4m, 7.25m, and 7.16m with varying near-surface geometry conditions (with and without cable trays).

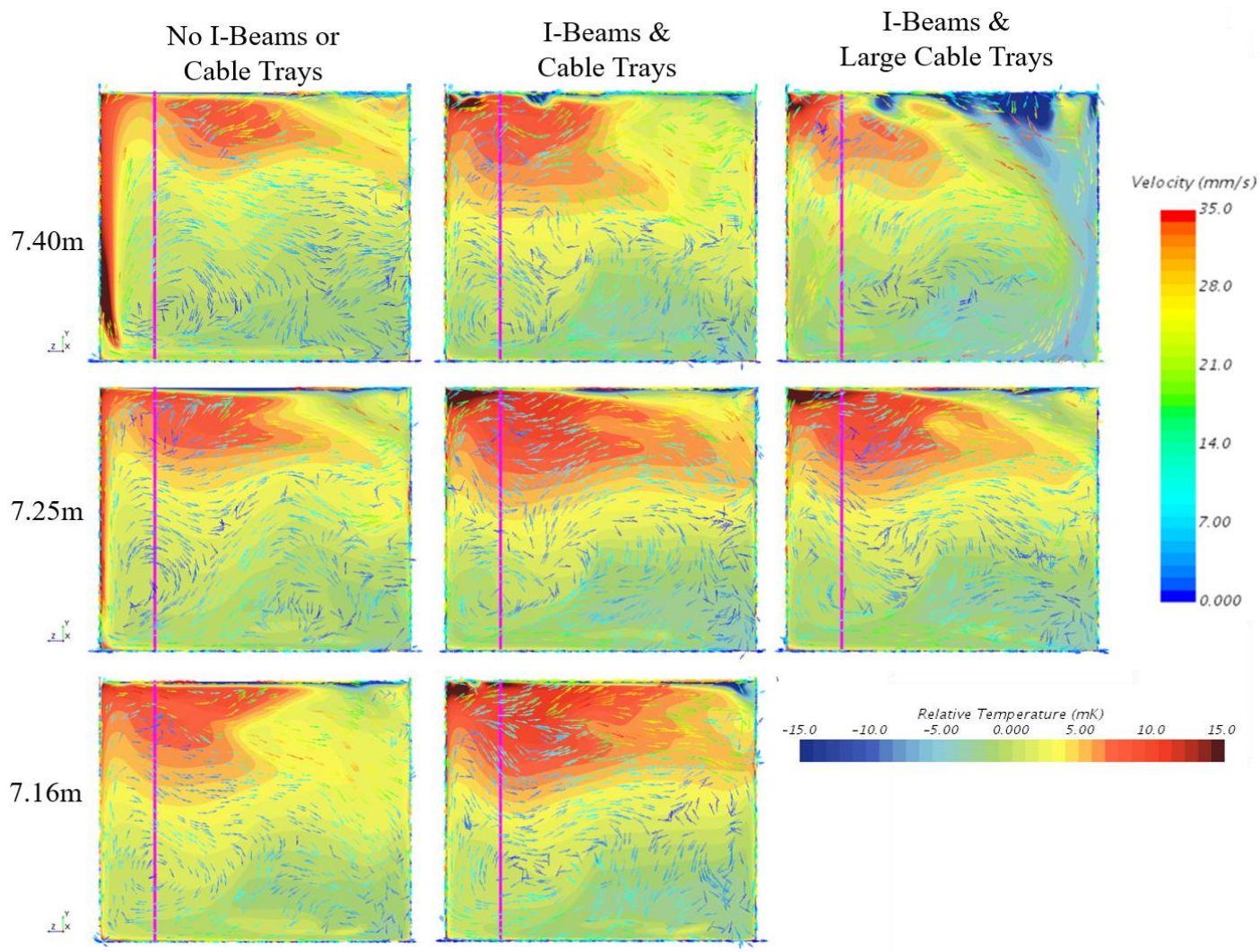

Figure 53. Varying LAr-ullage interface height and near-surface geometries simultaneously, relative temperature contour with velocity vector (projection) in-plane with Valencia.

4.4 Discussion

Previous CFD modeling efforts—although largely successful in terms of agreement with experimental data—exhausted available information of the detector and its operating conditions in trying to recreate the unusual LAr temperature profile observed by the static Valencia temperature probe. The purpose of this work, therefore, was to find plausible (physically relevant and theoretically sound) fluid mechanics and heat transfer explanations for the experimentally observed temperature phenomena—that is, to solve the inverse problem of source identification and/or estimation.

However, this is not a trivial question. Even in solving (forward modeling) the simplest buoyancy driven flows, there is an interdependent relationship between fluid temperature, fluid properties, and fluid velocity—that is, a change in one necessitates a change in the other. Additionally in such problems, the fluid domains' boundary geometries, thermal conditions, and relative orientation to the direction of gravity are important considerations. Thus, in the case of the LAr flow in the ProtoDUNE-SP neutrino detector, the intricate and numerous physical geometries (flow obstructions); unknown/ ill-defined heat sources (which change the fluid temperature, speed, and direction); and vast scale of the fluid domain add layers of uncertainty to the prediction of flow field values. In addition to the assumptions related to simplifying the buoyancy calculation, there are additional sources of uncertainty in traditional "forward modeling" in CFD. For example, there is inherent error in the spatial discretization of the fluid volume. Computational power is used more efficiently by concentrating high refinement (small cell size, large cell density) in regions where there are steep fluid temperature or velocity gradients and conversely specifying large cells in regions that have more

uniform field values. The discretization in time is also a matter of interest. As previously discussed, the models in this work assume that the flow field is quasi-steady state.

Other errors in the "forward modeling" are related to the uncertainty in the "known" detector operating conditions and geometries. The boundaries and boundary conditions in the base CFD model are largely based on reported values of the ProtoDUNE-SP operation. However, many of these values are from experimental measurements or from scientists' calculations/ estimates. In the case of experimental measurements, sensor precision and calibration are sources of uncertainty. In the case of scientists' estimates, error or uncertainty may be anything from rounding errors to simplifying assumptions. This is all speculation, though, since the reported values taken as "known" or "true" in defining the ProtoDUNE-SP LAr base CFD simulation did not have accompanying uncertainty data.

By inspection of the Valencia and Hawaii results, it is possible that representing the LAr-ullage equilibrium surface at a lower-than reported height may account for the non-linear behavior of the observed temperature. Since the height reported by the experimental "level meter" is disputed amongst DUNE researchers, and since the steadiness and flatness of the quasi-surface (interface) are unknown, it is possible that the actual equilibrium "surface" is lower than previously thought.

The effect of cold electronics heat on the Valencia temperature distribution was less pronounced than hypothesized. Although the +z CE region is in close proximity to and is upstream from the Valencia profile, the heated LAr does not directly encounter the sensor profile. None the less, it is possible that the reported estimate of CE heat (336W)

may be lower than the actual heat rejected since a slight increase to 504W slightly improved the relative temperature distribution of the Valencia profile.

The addition of field cage region volumetric heat improved the relative temperature distributions of the Valencia and Hawaii profiles by adding previously uncaptured nonlinearity to the Valencia profile. The physical relevance of the heat source magnitude is not well understood. It was previously reported that the FC heat was 1600 W/m^3, but it is hypothesized that this value is only applicable for the solid geometry. Therefore, for the isotropic porosity of 0.23 would result in a "reported" FC heat of 368 W/m^3. According to the results of the CFD FC heat study, it appears that this value is an overestimate of the actual volumetric heat rejection.

The addition of cable trays and I-beams results in a much more accurate representation of the actual geometries in the ProtoDUNE-SP cryostat. Their location and orientation normal to the +z side flow streams also make them very significant to the LAr flow patterns. These parametric investigations suggest that an impact on the flow fields is a slight "jetting" effect in the region of the Valencia profile as the +z side flow is redirected by the geometries and the LAr-GAr interface (Figure 54). This seems to create a recirculation of LAr in the vicinity of the CE and the top of the Valencia profile such that there is a relatively warm zone of LAr near the experimentally predicted "bump" of the Valencia. This demonstrates that it is important to model flow obstructions that are

large and that are normal to the flow. It also suggests that the near-surface geometries may cause the non-linear Valencia temperature distribution.

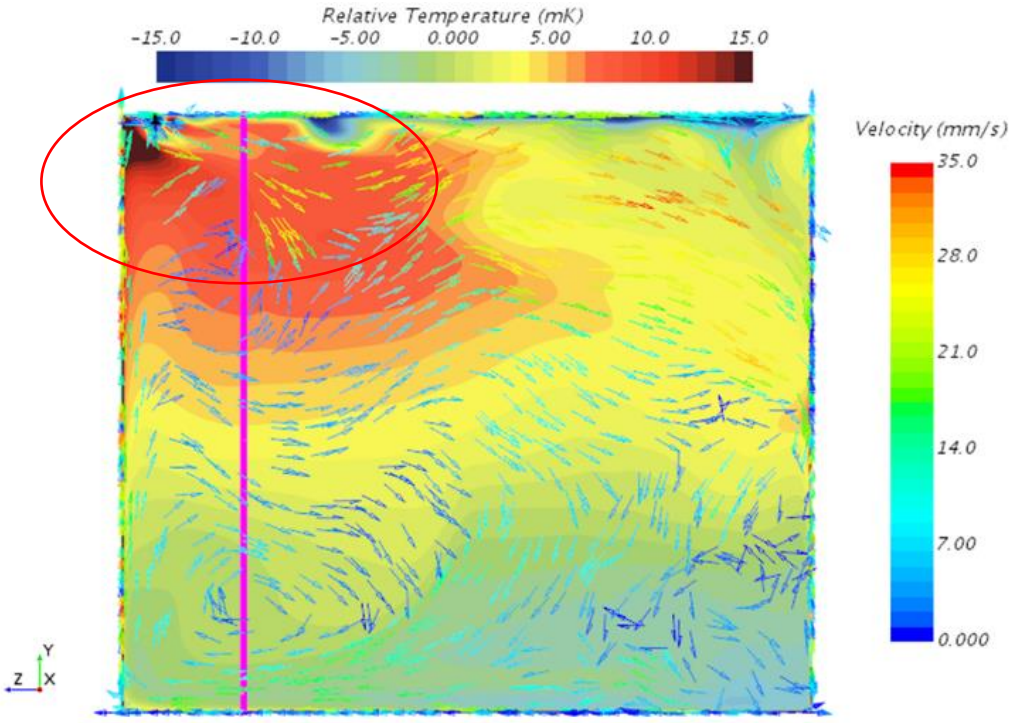

Figure 54. Relative temperature distribution with velocity vectors in-plane with the Valencia profile (x=3.414m), near surface geometries create "jetting" effect.

5 CONCLUSIONS AND FUTURE WORK

The purpose of this work was to better understand the fluid and heat flows of the LAr region of the ProtoDUNE-SP neutrino detector. This was accomplished by investigating previously unknown detector features in parametric CFD simulations. As is the case with many inverse problems, a single solution was not found, but rather there are several potential explanations for the experimentally observed temperature distributions. This section includes a summary of the major conclusions of this work and lists potential opportunities for future development.

5.1 Conclusions

- Iteration-averaged temperature reporting is necessary to eliminate solution unsteadiness and make accurate comparisons between different simulations.

- Modeling the LAr-ullage interface at a lower-than reported height improved agreement between the simulated and experimental Valencia temperatures.

- Under these modeling methods, there exists an optimum cold electronics heat source to minimize Valencia temperature error. Increasing the cold electronics (CE) heat source from 336W to 504W slightly improved Valencia temperature prediction.

- Adding and increasing volumetric heat source of the porous field cage (FC) regions adds desired nonlinearity to the Valencia temperature profile but does not necessarily improve its agreement with experimental.

- The physical geometries of the cable trays and I-beams have a significant effect on the LAr flow patterns, and thus may be responsible for the Valencia temperature profile “bump.”

- Accurate experimental operating conditions for CFD model boundary conditions is critical for solution accuracy.

- Flow obstructions and/or heat sources in the cryostat may be responsible for the non-linear behavior of the Valencia profile. There is likely not a singular cause, but a combination of effects.

5.2 Future Work

- Other heat sources (electronics) within the cryostat should be investigated to further improve the CFD temperature modeling.

- Other significant flow obstructions, especially those that are large, drastically obstruct/ redirect the flow, and in close proximity to the temperature sensors, should be identified and added to the model as detector photos and models become available.

- With the most accurate I-beams and cable tray representation in place, an additional study of varying CE heat and FC heat simultaneously should be conducted to identify the final, ideal heat input.

- Further investigation of the LAr height measurement "level meter" device and the experimental surface condition should be conducted, in collaboration with the DUNE researchers, to better understand the validity/ relevance of the lowered LAr height CFD results. Other geometric and thermal specifications for the modeled surface should be considered as a result of the investigation.

- The passive scalar/ impurity solutions of these CFD simulations were not considered at the time of this study. As new experimental impurity measurements become available, passive scalar convergence should be verified and the results studied.

- The CFD model should be updated with upcoming cryostat changes (i.e., additional sensors, geometries, etc.) associated with ProtoDUNE-Phase II.

6 BIBLIOGRAPHY

AEL Heating Solutions. (2018). Are Cast Radiators Efficient and Eco Friendly. Company Blog.

Alvarez, C., Conca, C., Lecaros, R., & Ortega, J. H. (2008). On the identification of a rigid body immersed in a fluid: A numerical approach. *Engineering analysis with boundary elements*, 32(11), 919-925. doi:10.1016/j.enganabound.2007.02.007

ANSYS Inc. (2021). Computational Fluid Dynamics (CFD) Simulation. Retrieved from https://www.ansys.com/products/fluids

Argoul, P. (2012). Overview of Inverse Problems. In *Parameter Identification in Civil Engineering* (pp. 13).

Autodesk Inc. (2020). Autodesk Computational fluid dynamics simulation software. Retrieved from https://www.autodesk.com/products/cfd/overview

Bangian-Tabrizi, A., & Jaluria, Y. (2018). An optimization strategy for the inverse solution of a convection heat transfer problem. *International journal of heat and mass transfer, 124*, 1147-1155. doi:10.1016/j.ijheatmasstransfer.2018.04.053

Cervera, A. (2019). *ProtoDUNE Temperature Sensors Overview Presentation (June 13).* PowerPoint. CISC. IFIC Valencia.

Chen, H.-T., Lin, M.-C., & Chang, J.-R. (2018). Numerical and experimental studies of natural convection in a heated cavity with a horizontal fin on a hot sidewall. *International journal of heat and mass transfer, 124*, 1217-1229. doi:10.1016/j.ijheatmasstransfer.2018.04.046

Chen, H.-T., & Chou, J.-C. (2006). Investigation of natural-convection heat transfer coefficient on a vertical square fin of finned-tube heat exchangers. *INT J HEAT MASS TRAN, 49*(17), 3034-3044. doi:10.1016/j.ijheatmasstransfer.2006.02.009

COMSOL Inc. (2020). Simulate Fluid Flow Applications with the CFD Module. Retrieved from https://www.comsol.com/cfd-module

Dassault Systèmes SolidWorks Corporation. (2020). SolidWorks Flow Simulation Website. Retrieved from https://www.solidworks.com/product/solidworks-flow-simulation

Farahani, S. D., Najafi, A. R., Kowsary, F., & Ashjaee, M. (2016). Experimental estimation heat flux and heat transfer coefficient by using inverse methods. *Scientia Iranica. Transaction B, Mechanical engineering, 23*(4), 1777.

Fermi National Accelerator Laboratory. (2020a). All Things Neutrinos Website. Retrieved from https://neutrinos.fnal.gov/mysteries/mass/

Fermi National Accelerator Laboratory. (2020b). Deep Underground Neutrino Experiment. Retrieved from https://www.dunescience.org/

Fermi National Accelerator Laboratory. (2020c). DUNE at LBNF. Retrieved from https://lbnf-dune.fnal.gov/

Hess, J. L., & Smith, A. M. O. (1967). Calculation of potential flow about arbitrary bodies. *Progress in Aerospace Sciences, 8*, 1-138. doi:https://doi.org/10.1016/0376-0421(67)90003-6

Huang, C. H., & Özisik, M. N. (1992). Inverse Problem of Determining Unkown Wall Heat Flux in Laminar Flow through a Parallel Plate Duct. *Numerical Heat Transfer, Part A: Applications, 21*(1), 55-70. doi:10.1080/10407789208944865

Inverse problems in science and engineering. (2004).

Jaluria, Y. (2020). Solution of Inverse Problems in Thermal Systems. *J. Thermal Sci. Eng. Appl, 12*(1). doi:10.1115/1.4042353

Johnson, N. L. (1996). *The Legacy and Future of CFD at Los Alamos*. Paper presented at the Canadian CFD Conference, Ottawa, Canada.

Karageorghis, A., & Lesnic, D. (2020). Identification of obstacles immersed in a stationary Oseen fluid via boundary measurements. *Inverse problems in science and engineering, 28*(7), 950-967. doi:10.1080/17415977.2019.1686498

Kumar, H., & Nagarajan, G. (2018). A Bayesian inference approach: estimation of heat flux from fin for perturbed temperature data. *Sadhana (Bangalore), 43*(4), 1-16. doi:10.1007/s12046-018-0861-7

Li, H. Y., & Yan, W. M. (2000). Inverse Convection Problem for Determining Wall Heat Flux in Annular Duct Flow. *J. Heat Transfer, 122*(3), 460-464. doi:10.1115/1.1287169

Matsuo, T., Shimadera, H., & Kondo, A. (2019). Identification of multiple contamination sources using variational continuous assimilation. *Building and environment, 147*, 422-433. doi:10.1016/j.buildenv.2018.10.041

Munson, B. R., Okiishi, T. H., Huebsche, W. W., & Rothmayer, A. P. (2013). *Fundamentals of Fluid Mechanics*. Hoboken, NJ: John Wiley & Sons.

Nellis, G., & Klein, S. (2009). *Heat Transfer*. New York, NY: Cambridge University Press.

OpenCFD Ltd. (2019). OpenFOAM: the Open Source CFD Toolbox. Retrieved from https://www.openfoam.com/

Orlande, H. R. B. (2012). Inverse Problems in Heat Transfer: New Trends on Solution Methodologies and Applications. *J. Heat Transfer*, *134*(3), 31011. doi:10.1115/1.4005131

Ozisik, M. N., & Orlande, H. R. B. (2000). *Inverse Heat Transfer Fundamentals and Applications*. New York, NY: Taylor & Francis.

Pedersen, D. (2019). *Quantifying the Performance of the Protodune Single Phase Neutrino Detector Using Computational Fluid Dynamics*. South Dakota State University, Electronic Theses and Dissertations. Retrieved from https://openprairie.sdstate.edu/etd/3148

Propst, A. (2017). *CFD Analysis Methods for Systems Driven by Natural Convection*. South Dakota State University, Electronic Theses and Dissertations. Retrieved from https://openprairie.sdstate.edu/etd/2145

Resolved Analytics. (2019). Comparing CFD Software - Part 3: Semi-Comprehensive Software. Retrieved from https://www.resolvedanalytics.com/theflux/comparing-cfd-software-part-3-semi-comprehensive-cfd-software

Resolved Analytics. (2020). Comparing CFD Software - Part 4: Comprehensive CFD Software Packages. Retrieved from

https://www.resolvedanalytics.com/theflux/comparing-cfd-software-part-4-comprehensive-cfd-software-packages

Siemens. (2021). Simcenter STAR-CCM+. Retrieved from https://www.plm.automation.siemens.com/global/en/products/simcenter/STAR-CCM.html

Tamaddon-Jahromi, H. R., Chakshu, N. K., Sazonov, I., Evans, L. M., Thomas, H., & Nithiarasu, P. (2020). Data-driven inverse modelling through neural network (deep learning) and computational heat transfer. *Computer methods in applied mechanics and engineering*, *369*, 113217. doi:10.1016/j.cma.2020.113217

Tarantola, A. (2005). *Inverse Problem Theory and Methods for Model Parameter Estimation*. Paris, France: SIAM.

The DUNE Collaboration. (2017). *The Single-Phase ProtoDUNE Technical Design Report*. Retrieved from DUNE-doc-13921-v1:

The DUNE Collaboration. (2020). Deep Underground Neutrino Experiment (DUNE) Far detector technical design report: Volume I. Introduction to DUNE. *Journal of Instrumentation*, *15*. doi:T08008

Voirin, E. (2015). LBNF Liquid Argon Flow Simulations. *DUNE Docs Database, DUNE-doc-581-v4*.

Voirin, E. (2016). 35 Ton LAr Impurity Distribution Measurements and CFD simulation. *DUNE Docs Database, DUNE-doc-1156-v1*.

Woodbury, K. A. (2003). *Inverse engineering handbook*. Boca Raton, Fla.: Boca Raton, Fla. : CRC Press.

Yaman, F., Yakhno, V. G., & Potthast, R. (2013). A Survey on Inverse Problems for Applied Sciences. *Mathematical Problems in Engineering*, *2013*, 1-19. doi:10.1155/2013/976837

Zhang, D.-D., Zhang, J.-H., Liu, D., Zhao, F.-Y., Wang, H.-Q., & Li, X.-H. (2016). Inverse conjugate heat conduction and natural convection inside an enclosure with multiple unknown wall heating fluxes. *International Journal of Heat and Mass Transfer, 96*, 312-329. doi:10.1016/j.ijheatmasstransfer.2016.01.012

Zueco, J., Zueco, J., Alhama, F., Alhama, F., González Fernández, C. F., & González Fernández, C. F. (2005). Numerical nonlinear inverse problem of determining wall heat flux. *Heat Mass Transfer, 41*(5), 411-418. doi:10.1007/s00231-004-0553-1